ĐẠI HỌC THÁI NGUYÊN
**TRƯỜNG ĐẠI HỌC KHOA HỌC**

**CỘNG HOÀ XÃ HỘI CHỦ NGHĨA VIỆT NAM**
**Độc lập - Tự do - Hạnh phúc**

*Thái Nguyên ngày 30 tháng 10 năm 2025*

# GIẤY XÁC NHẬN

Trường Đại học Khoa học, Đại học Thái Nguyên (Địa chỉ: Phường Phan Đình Phùng, tỉnh Thái Nguyên), xác nhận:

1. Bà Trương Thị Thảo, sinh ngày 31/01/1980, học hàm: Phó giáo sư, học vị: Tiến sĩ, là Giảng viên Khoa Khoa học Tự nhiên và Công nghệ, trường Đại học Khoa học, Đại học Thái Nguyên
2. Hai đề tài khoa học công nghệ:

   *Đề tài 1:* "Chế tạo than sinh học sả bằng phương pháp thủy nhiệt và ứng dụng làm vật liệu hấp phụ xử lý môi trường", mã số CS2023-TN06-17, Chủ nhiệm: ThS. Chu Thị Hồng Huyền.

   *Đề tài 2*: "Ảnh hưởng của môi trường thủy nhiệt tới đặc trưng và khả năng hấp phụ một số chất màu của hydrochar bã chưng cất tinh dầu sả", mã số CS2024-TN06-17. Chủ nhiệm: PGS.TS. Trương Thị Thảo

   Là hai đề tài được thực hiện tại trường Đại học Khoa học, Đại học Thái Nguyên, do trường tài trợ kinh phí, được thực hiện bởi PGS.TS. Trương Thị Thảo - khoa Khoa học Tự nhiên và Công nghệ và ThS. Chu Thị Hồng Huyền – Giảng viên khoa Tài nguyên và Môi trường, đã được nghiệm thu trong năm học 2024-2025.
3. Kết quả thực hiện của hai đề tài trên đều trung thực, đáng tin cậy, có giá trị khoa học và thực tiễn cao. Than sinh học thủy nhiệt từ bã sả lần đầu tiên được nghiên cứu chế tạo một cách hệ thống, xây dựng được quy trình chế tạo tối ưu, có khả năng sản xuất quy mô công nghiệp vừa và nhỏ, là sản phẩm thân thiện môi trường; là một trong số ít các vật liệu được nghiên cứu và có hiệu qủa cao xử lý ô nhiễm đồng thời nhiều kim loại nặng và chất màu, tái sinh và tái sử dụng tốt. Các kết quả thử nghiệm mẫu thực, thử nghiệm hiện trường ban đầu quy mô vừa và nhỏ khá tốt. Công trình đã góp phần nâng cao chuyên môn nghiệp vụ, năng lực nghiên cứu khoa học của cán bộ giảng viên nhà trường, đồng thời nâng cao chất lượng đào tạo người học.
4. Kết qủa nghiên cứu còn có giá trị tham khảo cao về mặt học thuật, đã công bố trên các tạp chí khoa học uy tín quốc tế, được các nhà khoa học quốc tế quan tâm trích

dẫn (Hai công bố từ 3/2025 tới nay 30/10/2025 đã có 9 và 5 lượt trích dẫn quốc tế, https://scholar.google.com/citations?user=sO9ejYkAAAAJ&hl=vi). Đây là hướng nghiên cứu có tính ứng dụng thực tế cao, đáp ứng xu hướng hóa học xanh, sản xuất xanh, kinh tế xanh và kinh tế tuần hoàn.

TRƯỜNG ĐẠI HỌC KHOA HỌC – ĐH THÁI NGUYÊN

TRƯỜNG ĐẠI HỌC KHOA HỌC

TL. HIỆU TRƯỞNG
VIỆN TRƯỞNG VIỆN KHOA HỌC & CÔNG NGHỆ
PGS.TS. Nguyễn Xuân Ca

Journal of Molecular Liquids 425 (2025) 127205

Contents lists available at ScienceDirect

Journal of Molecular Liquids

journal homepage: www.elsevier.com/locate/molliq

# Adsorption characteristics of single and binary mixture of methylen blue and rhodamine B of novel hydrochar derived from lemongrass essential oil distillation residue

Thi Thu Uyen Le [a], Thi Giang Ngo [a], Ngoc Anh Hoang [a], Van Hao Nguyen [b], Van Dang Nguyen [b], Le Phuong Hoang [c], Tien Duc Pham [d], Thi Thao Truong [a,*]

[a] Faculty of Chemistry, TNU-University of Sciences, Thai Nguyen 250000, Viet Nam
[b] Instittute of Science and Technology, TNU-University of Sciences, Thai Nguyen 250000, Viet Nam
[c] Faculty of Civil and Environmental Engineering, Thai Nguyen University of Technology (TNUT), Tich Luong Ward, Thai Nguyen 250000, Viet Nam
[d] Faculty of Chemistry, University of Science, Vietnam National University, Hanoi, 19 Le Thanh Tong, Hoan Kiem, Hanoi 100000, Viet Nam

ARTICLE INFO

*Keywords:*
Lemongrass
Hydrochar
Adsorption
Rhodamine B
Methylene blue

ABSTRACT

The present study evaluates the influence of hydrothermal environment ($H_2O$, 1 M KOH, 1 M $H_2SO_4$ and 5 % $H_3PO_4$) on the properties of hydrochars from lemongrass essential oil distillation residue (LDR), and applied for simultaneously adsorption of methylene blue (MB) and rhodamine B (RhB) dyes in water. The hydrochars were characterized using different physicochemical techniques including XRD, Raman, SEM-EDS, FTIR and BET methods. The results indicated that the PLH (hydrothermal LDR in 5 % $H_3PO_4$ solution) had the highest carbon content, most porous structure, most uniform material size and largest specific surface area at 28.37 $m^2/g$. The PLH performed well in both single and mixed adsorption with MB and RhB. The highest adsorption capacity was achieved at pH 4, and increased with temperature. Adsorption efficiency for MB was better than for RhB, the maximum sorption capacity for MB and RhB were 97 and 78 mg/g, respectively, and insignificantly reduced in mixed adsorption. After regeneration, the sorption capacity slightly increased in individual adsorption but slightly decreased in mixed adsorption. The single adsorption process followed the Sips isotherm model while both single adsorption and mixed adsorption were fitted well with the pseudo – second order kinetic model, spontaneous, and endothermic. The results indicated that the surface of PLH was heterogeneous and the chemisorption played a dominant role. The dominant interaction between RhB and PLH involved π-π interactions between aromatic rings, while are the interactions included π-π interactions from C═N and C═C and hydrogen bonding between the nitrogen atoms and the O–H group on the PLH surfacewere governed MB adsorption. Our results indicate that the hydrochars derived from LDR is an efficient adsorbent with high adsorption capacities for both MB and RhB in single and mixed adsorption system.

## 1. Introduction

The textile and leather industry plays a vital role in the global economy, the global textile market was approximately $920 billion [1] in 2021, and it is projected to continue growing in the coming years. However, these contributions also come with significant environmental cost, including the consumption of tons of dyes each year, for example: the global dye market was valued at approximately $38.14 billion USD (representing around 2–3 million tons of dyes) in 2022, and it is expected to grow at a compound annual growth rate of around 4–5 % in the coming years [2]. Of which, the textile and leather industry consumes about 70 %. As a result, substantial dye residues are released into the environment during production, use and disposal process, making dyes is one of the major contributors to global environmental pollution. Among these, synthetic dyes such as azo dyes, anthraquinone dyes and triphenylmethane dyes are particularly problematic because they s are not biodegradable and exist for a long time in the environment, causing many serious consequences. All dyes alter the color of water, reduce the oxygen content level in water, and disrupt the natural development of aquatic organisms.

* Corresponding author.
*E-mail address:* thao.tt@tnus.edu.vn (T.T. Truong).

https://doi.org/10.1016/j.molliq.2025.127205
Received 4 January 2025; Received in revised form 17 February 2025; Accepted 19 February 2025
Available online 23 February 2025

Methylene blue (MB) is a very popular dye from the phenolthiazines family with a tricyclin phenolthiazine, formula is $C_{16}H_{18}ClN_3S$ (Fig. 5a), soluble in water and some organic solvents. Although MB has numerous promising benefits across various medical applications, but, MB can interfere with bacterial growth in water, disrupting natural purification processes. It is a toxic, carcinogenic, and mutagenic, with potential to cause serotonin toxicity in humans at high doses [3]. MB-induced serotonergic toxicity can lead to neuromuscular hyperactivity; dose-dependent toxicity of MB includes hemolysis, methemoglobinemia, nausea, chest pain, and hypertension [4]. It also includes skin irritation and inflammatory responses. RhB is also a popular azo dye, formula is $C_{28}H_{31}ClN_2O_3$ (Fig. 5b), can exist in two forms: an "open"/fluorescent from (in acidic condition) and a "closed"/nonflurescent spirolactone from in basic condition, soluble in common solvents. RhB is applied in a number of fields, including photochromics, thermochromics, and ionochromics [5]. RhB and its derivative rhodamine 6G have been utilized as colorimetric and fluorescent chemo sensors for detecting metal ions, particularly copper, in environmental and biological samples [6]. However, RhB poses significant health risks in both humans and animals. RhB causes infections of the skin, eyes, respiratory system, digestive system, including the potential to cause liver damage, tumors, and cancer [7]. Prolonged exposure to RhB has been shown to lead liver cell necrosis and tissue disintegration in animal studies [8].

Therefore, the removal of these dye from polluted environment, is crucial. Various methods have been explored, including chemical, biological, and physical techniques. While chemical methods may generate secondary pollutants and biological methods are sensitive to pH, adsorption has emerged as a promising physical technique due to its effectiveness and economic feasibility [3,9]. Various types of adsorbent materials have been studied for the removal of MB, RhB and their mixture. Important criteria when choosing an adsorbent include: high efficiency, low price, available raw materials, easy to regenerate materials, simple and easy to regenerate materials. Therefore, biochar is one of the top choices compared to materials of mineral origin such as oxides, composites, mineral rocks, … Biochar derived from various biomass sources, through pyrolysis or hydrothermal processes, have shown significant potential in removing a variety of pollutants, including MB and RhB removal [9,10]. The pyrolysis was often occurred at 300 °C to 700 °C for 30 min to several hours in nitrogen environment, using dry biomass. In contrast, hydrothermal process operates at 180 °C to 260 °C for several hours, with either dry or wet biomass. This makes the hydrothermal process more environmentally friendly and energy efficient compared to pyrolysis. MB adsorption has been extensively studied globally utilizing various types of adsorbents, especially carbon-based materials [11–13]. Hydrochars derived from different biomass sources, includes pristine hydrochar, such as Mason pine, cedarwood, bamboo, coconut shell, pecan shell, wheat straw, maize straw, rice straw [14], coffee husk [15], shorrea spp. [16], nut shell [17], pomegranate [18], sewage sludge hydrochar [19], modified hydrochar [20], or walnut and silicate hydrochar composite [21]. All exhibited adsorption capacities for MB ranging from 64.43 to 657.76 mg/g, demonstrating their potential as cost-effective for wastewater treatment. However, only a limited number of hydrochars derived from agricultural residues have been studied to adsorb RhB [22–24]. For instance, Kohzadi *et al.* used wheat straw to produced hydrochar and biochar, finding that, hydrochar adsorbed RhB approximately 1.7 times more than the biochar, and twice as effectively as untreated wheat straw. When modified with Fe, the RhB adsorption capacity of wheat straw hydrochar increased significantly, to 80 mg/g while Fe-modified wheat straw biochar showed little improvement [25]. Citric acid modified furfural residue hydrochar demonstrated a maximum theoretical adsorption capacity of 39.46 $mg{\cdot}g^{-1}$ at pH 3, with a retention rate of 92.74 % after five regeneration cycles [26]. Certain adsorbents from agricultural residues have been evaluated for the individual adsorption both MB and RhB. Examples include shea butter leaves [27], cellulose fibers activated biochar [28], $HNO_3$ activated longan peel [29], *Pongamia glabra* seed cover biochar, [30], biochar and EDTA modified biochar of palm kernel shells [31], seeds of *Aleurites Moluccana* [32] and microplastics before and after ultraviolet irradiation [33]. Mixture of MB and RhB was adsorbed by some adsorbents from natural, such as: alkaline-modified Vietnam diatomite [34]; the commercial natural zeolite from deposits in Semnan, Iran [35]; agricultural waste such as *Onecarpus bacaba* Mart fiber residues (collected in Itacoatiara, Amazonas state, Brazil), in natural (OBMi) and NaOH-modifed (OBMm), in which, OBMm was more efficient [36]; a pyrochar of cassava peel (was obtained from a farm in Djakotomey, Benin) was studied for the single and binary adsorption of MB, malachite green (MG), and RhB demonstrating adsorption capacities ranging from 20.48 mg/g to 407.98 mg/g for MB, 5.51 mg/g to 143.70 mg/g, for RhB, and in mixed adsorption MB and RhB, 10.00 mg/g to 145.60 mg/g for MB, and 4.82 mg/g to 67.06 mg/g for RhB [37]. Despite the environmental advantages of hydrothermal processes over pyrolysis, no studies on hydrochars for simultaneous adsorption of MB and RhB have been published. Furthermore, there is little research on biochar production from lemongrass essential oil distillation residue (LDR). Lemongrass (Cymbopogon spec.) is a popular tropical and subtropical plant, a small amount is used directly in food and medicine, mainly used to produce lemongrass essential oil, a widely popular flavor around the world, due to its scent and numerous health benefits, the global lemongrass oil market is projected to grow from $41.98 million to $ 81.43 million between 2021 and 2028, with Compound Annual Growth Rate of 9.3 % [38]. Therefore, LDR, a waste byproduct from lemongrass essential oil production, has a very large annual output. The distillation acts as a pretreatment stage, helping to simplify the LDR carbonization process, shorten time and save energy. Currently, only a few studies have reported the production of pyrochar from lemongrass residue for application in agricultural land improvement [39–42]. There are no publications on hydrochar, used for treat water pollutant.

Base on the above premises, in this study, the first time, we explored the hydrochar synthesis from LDR, examined the characteristics of hydrochars, identified the optimal material to evaluate its capacity for single and mixed adsorption of MB and RhB dyes. To improve the availability of hydrochar, various activation methods have been studied, both of physical and chemical activation. Although chemical activation requires to use of chemicals, it has many advantages: easy to perform, saves energy and cots (because common and cheap chemicals are often used), is very diverse and easy to adjust the desired properties of prepared materials by adjusting the type and dosage of activator. In the early stages of researching the production of LDR hydrochar, we choose some popular activators that have been applied in many previous study to activate hydrochar and have good results [43]: a strong alkaline, a strong and a weak acid. Therefore, the hydrothermal LDR was conducted in different environments: distillation water, 1 M KOH, 1 M $H_2SO_4$ and 5 % $H_3PO_4$.

## 2. Materials and methods

### 2.1. Chemicals

Rhodamine B ($C_{28}H_{31}ClN_2O_3$, Sigma-Aldrich, ≥95 % (HPLC)), Methylene Blue ($C_{16}H_{18}ClN_3S{\cdot}3H_2O$, Sigma-Aldrich, ≥98.5 %), distilled water (DW), hydrochlohydric acid (HCl, Isochem, 36–37 %), sodium hydroxide (NaOH, Isochem, 98.5 %), phosphoric acid ($H_3PO_4$, Sigma-Aldrich, ≥99 %), potassium hydroxide (KOH, Sigma-Aldrich, ACS reagent, ≥85%, pellets), and ethanol ($C_2H_6O$, Sigma-Aldrich, 96 % (v/v)). Lemongrass were collected in Thai Nguyen, Vietnam, LDR was recovered at the Institute of Life Sciences, Thai Nguyen University, Thai Nguyen, Vietnam.

### 2.2. Synthesis of hydrochar

LDR was dried to constant mass at 105 °C. It was finely ground and store in a desiccator. 8 g of DWL was completely dispersed in 50 mL of

solvent (DW, KOH 1 M, $H_2SO_4$ 1 M, $H_3PO_4$ 5 %) in a 100 mL Teflon container. The container was then placed in a stainless steel autoclave, heated to 220 °C for 6 h (heating rate of 200 °C/h), and allowed to cool naturally. The resulting material was washed with DW until the wash was colorless and neutral It was then oven-dried to constant mass at 105 °C, allowed to cool naturally, stored in a zip-top plastic bag in a desiccator, and designated as LH, KLH, SLH and PLH, respectively (Fig. 1).

### 2.3. Characterization of the materials

LDR and hydrochars were characterized using various analytical techniques. X-ray diffraction (XRD) was performed with a PANanalytical X'Pert PRO MPD diffractometer, operating at 40 kV and 30 mA, using Cu-Kα radiation (λ = 0.15406 nm) in the 2θ range from 15° to 70°. Fourier-transform infrared (FTIR) spectroscopy was conducted with a Perkin Elmer-400 spectrometer, analyzing pellets prepared by mixing KBr and sample at a weight ratio of 1:99, over a wavenumber range of 4000 to 400 $cm^{-1}$. Scanning electron microscopy (SEM), integrated with an Energy-Dispersive X-ray System (EDS), was performed using a Hitachi S-4800 instrument at an acceleration voltage of 20 kV, before scanning, samples were sputter coated with Pt for 30 s at 20 mA and vacuum of 10 Pa. Raman spectroscopy was conducted with a LabRAM HR Evolution spectrometer (Horiba) using a 532 nm argon laser as the excitation source, the exposure time is 15 s and laser power of 3.2 mW. The Brunauer–Emmet–Teller (BET) method was applied using a TriStar 3000 V6.07 instrument. Dynamic Light Scattering and Zeta potential measurement were carried out with a Zetasizer Nano ZS instrument (Malvern Panalytical, England). The point of zero charge ($pH_{PZC}$) was identified experimentally using the pH-drift method: preparing 9 solutions of 0.1 M KCl at pH of 2, 3, 4, 5, 6, 7, 8, 9 and 10. Add 25 mg PLH to each 25 ml of that solution, shake well for 24 h then re-measure the final pH of the solution to determine the ΔpH ($\Delta pH = pH_{final} - pH_{initial}$), experiment was repeated 3 times to obtain average values. Build a graph to represent the ΔpH via the initial pH, the pH at which the $\Delta pH = 0$ is the point of zero charge ($pH_{PZC}$).

### 2.4. Adsorption tests and data analysis

The adsorption experiments were carried out in 15 mL Conical Sterile Polypropylene Falcon tubes. For each adsorption experiment, an exact mass of PLH sample was added to 10 mL of the study solution (MB, RhB solution or a mixture of MB and RhB with the designed initial concentrations and pH). The tubes were then placed in a constant temperature shaker at 150 rpm for a specific period of time. After shaking, the treated solutions were centrifuged to separate the solid and liquid fractions. The solid fractions were recovered for analysis and regeneration, while the liquid fractions were used to determine the residual dye concentrations after adsorption using the ultraviolet–visible spectrophotometer method at wavelength of 553,5 nm and 663 nm, corresponding to RhB and MB, respectively. Each experiment was repeated 3 times to obtain average values.

The adsorption capacity (q, mg/g) and the adsorption efficiency (AE, %) are calculated using the following Eqs. (1) and (2), respectively:

$$q = (C_o - C)\frac{V}{m} \quad (1)$$

$$AE = \frac{(C_o - C)}{C_o}.100\% \quad (2)$$

where $C_o$ and C are the initial concentration and residual concentration of the dye in the solution after adsorption for t min (mg/L), V is the volume of the working solution (L), and m is the mass of the adsorbent (g).

To study the adsorption kinetics, the experimental data were fitted to the pseudo-first-order (PFO), pseudo-second-order (PSO), and Elovich kinetic models, based on the following non-linear Eqs. (3)–(5), respectively:

$$q_t = q_e\left(1 - e^{-k_1 t}\right) \quad (3)$$

$$q_t = \frac{k_2 q_e^2 t}{1 + k_2 q_e t} \quad (4)$$

$$\mathrm{qt} = \frac{1}{k_e}\ln(\mathrm{a.ke} + \mathrm{t}) \quad (5)$$

where $k_1$ ($min^{-1}$), $k_2$ ($g.mg^{-1}.min^{-1}$) and $k_e$ ($g.mg^{-1}$) are the rate constants for the PFO, PSO, and Elovich kinetic models, respectively. The term $1/k_e$ represents the number of sites available for adsorption and a is initial adsorption rate (mg. $g^{-1}.min^{-1}$) in the Elovich kinetic model.

The adsorption thermodynamic parameters, including equilibrium stability constant ($K_C$), the Gibbs free energy (ΔG) and enthalpy (ΔH), were calculated using following Eqs. (6)–(8), respectively:

$$K_C = C_s/C_e \quad (6)$$

$$DG = -RTln(K_C) \quad (7)$$

$$ln\frac{K_{T_2}}{K_{T_1}} = \frac{\Delta H}{R}\left(\frac{1}{T_1} - \frac{1}{T_2}\right) \quad (8)$$

where $C_s$ and $C_e$ are the equilibrium concentrations of dye on the adsorbent surface and in the aqueous phase, respectively, ($C_s = C_o - C_e$).

To study the adsorption isotherm, the experimental data were fitted to the non-linear forms of the Langmuir, Freundlich, and Sips isotherm models, according to the following Eqs. (9)–(11):

$$q_e = \frac{q_m.K_L.C_e}{1 + K_L.C_e} \quad (9)$$

$$q_e = K_F.C_e^{1/n_F} \quad (10)$$

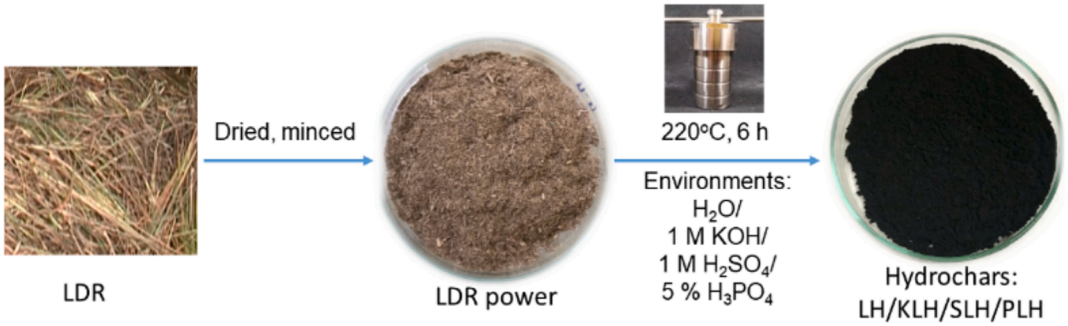


**Fig. 1.** Diagram for synthesis hydrochar from LDR.

$$qe = \frac{K_s C_e^{n_s}}{1 + b_s C_e^{n_s}} \quad (11)$$

where $q_e$ and $q_m$ are the equilibrium sorption capacity and the maximum monolayer sorption capacity (mg/g), respectively; $K_L$ (L/g), $K_F$ ($mg^{1-n_F}.L^{n_F}.\ g^{-1}$) and $K_S$ ($mg^{1-n_S}.L^{n_S}.\ g^{-1}$) are the Langmuir, Freundlich and Sips adsorption constant, respectively; $n_F$ is the Freundlich exponent coefficient related to adsorption intensity, and $n_S$ is the Sips exponent coefficient related to the heterogeneity of the adsorbate-adsorbent system. $b_s$ is a dimensionless parameter that qualitatively characterizes the heterogeneity of the adsorbate-adsorbent system.

### 2.5. Regeneration and reusable adsorbent materials

After MB adsorption, the PLH was collected, soaked for 4–5 h and washed many times with 0.1 M HCl until the HCl solution does not change color. The material was then washed to neutrality, dried, and used to evaluate reusability [44].

After RhB adsorption, the PLH was regenerated as MB post-adsorption material using1 M NaOH solution. Finally, it was calcined at 400 °C for 1 h in nitrogen, allowed to cool naturally, and used to evaluate reusability [45].

After adsorption of a mixture of MB and RhB, the PLH was collected, soaked, and washed several times with 99 % ethanol until the ethanol no longer change color. It was then dried and used to evaluate reusability [46].

## 3. Results and discussion

### 3.1. Characterization of hydrochars

Lemongrass hydrochar, which was hydrolyzed in different solutions, was characterized using several techniques. Fig. 2 shows the XRD, Raman, EDS, and FTIR spectra.

The XRD spectrum (Fig. 2a) of LDR exhibits a broad and intense diffraction peak at approximately 21.9° and a small diffraction peak at around 34.4°, characteristic of the cellulose structure [47]. Additionally, a sharp and narrow peak at around 26.5° is attributed to the (002) reflection planes of graphite [48]. After being hydrolyzed in water at 220 °C, the XRD spectrum of LH sample shown significant changes: the intensity of diffraction peaks decreased sharply, and the peaks at 21.9° in the LDR spectrum shifted to a lower 2θ angle, indicating the transformation of the cellulose structure into an amorphous carbon form. However, the hydrothermal sample treated in 1 M $H_2SO_4$ environment (KLH) had no change in the cellulose structure. Instead, a new peak appears at 15.5°, corresponding to the (101) crystal planes of cellulose [49]. For the hydrothermal samples treated in a 1 M KOH solution (KLH) and a 5 % $H_3PO_4$ solution (PLH), cellulose decomposition was evident. The diffraction peak of cellulose was split into two distinct peaks (both significantly reduced in intensity) representing cellulose and amorphous carbon. Additionally, the characteristic graphite peaks were reduced and broadened, indicating that LDR underwent a stronger transformation in $H_3PO_4$ and KOH solutions.

The Raman spectra of LH sample (Fig. 2b) only consists of D band (1335 $cm^{-1}$, typical for defects and disorder in the graphitic lattice or amorphous carbon structures) and G band (1574 $cm^{-1}$, corresponding to the graphitic structure) [50]. In Raman spectroscopy of the KLH and PLH samples, some other bands are observed. These include bands at 1118 and 1220 $cm^{-1}$, attributed to contributions from amorphous

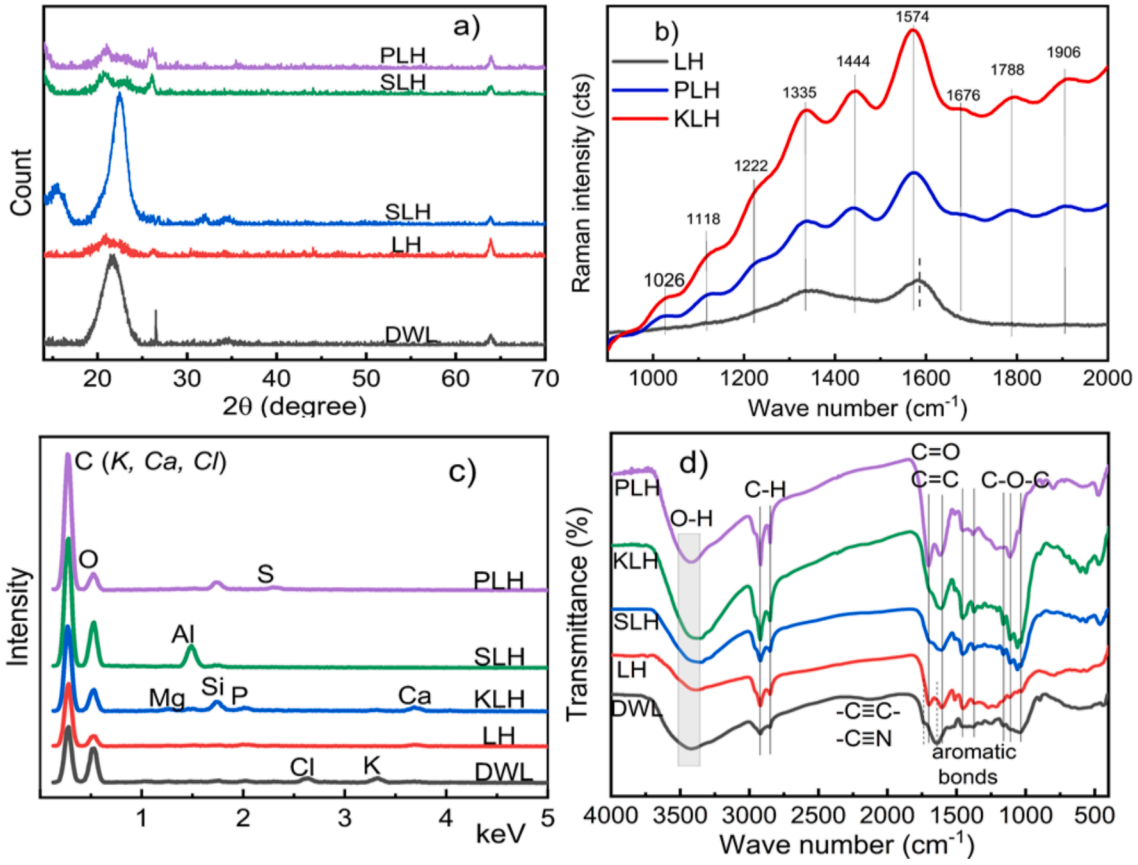


**Fig. 2.** The XRD patterns (a), Raman spectra (b), EDS spectra (c) and FTIR spectra (d) of LDR and prepared lemongrass hydrochars.

structure or impurities; at 1444 $cm^{-1}$ characteristic of $CH_2$ bending vibration in amorphous carbon; and at 1676, commonly found in graphite materials. However, when combined with the G peak, this bands reflects disordered material or amorphous carbon [51]. Additionally, bands at 1788 and 1906 are assigned to the C═O functional group in GO [52]. These results suggest that the hydrothermal process partially converted cellulose into amorphous carbon and GO, with the conversion efficiency increasing as the hydrothermal environment changed from neutral to alkaline and then to acidic conditions.

This transformation is also reflected in the change in carbon content of the samples, as shown in the EDS spectrum (Fig. 2c). The carbon content increases gradually with the increasing intensity of the carbon signal in the spectrum (details in Table 1).

Table 1 shows that the SLH sample has the lowest carbon content while PLH has the highest. This result is consistent with the analysis obtained from the XRD and Raman spectra.

The characteristic bonds in the sample were determined from the FTIR spectrum in Fig. 2d. All samples have several common features, including: (1) a broad peak about 3410 $cm^{-1}$ assigned to the O–H stretching vibration; two peaks at 2918 and 2850 $cm^{-1}$ assigned to the C–H symmetric and asymmetric stretching vibrations. Outside that, the stretching vibration of −C≡C– or −C≡N bonds, typically represented by a broad peak at about 2220 $cm^{-1}$, observed in DWL, disappeared in the hydrochar samples. The peaks at 1740 $cm^{-1}$ and 1649 $cm^{-1}$ representing the C═O and C═C stretching vibrations in LDR, shifted to lower wave numbers (1700 $cm^{-1}$ and 1640 $cm^{-1}$, respectively) in hydrochar samples, with a change in the intensity ratio between the two peaks. The spectral region 1500 to 1200 $cm^{-1}$, attributed to C–C, C═C, and aromatic bonds, decreased in intensity from the hydrothermal solutions of water, KOH, and $H_3PO_4$, indicating that the ability to decompose these bonds is the weakest in water and strongest in $H_3PO_4$. The spectral region 1200–1000 $cm^{-1}$, representing the C-O-C bonds, remained fairly stable across the samples, with only a slight shift in position, suggesting that this bond is less affected by the hydrothermal process in different environments.

SEM micrographs of LDR and hydrochars are shown in Fig. 3. The surface of LDR (Fig. 3a) is not flat; it has various convex and concave areas and round scales with a diameter of about 0.5 μm. After hydrothermal treatment, the surface of SLH (Fig. 3d) appears minimally damaged, with fragmented scales lying on fairly large flat fragments. This shows that the 1M $H_2SO_4$ environment does not cause significant fragmentation of the source material, despite changes in its initial physical structure. The extent of physical decomposition of LDR increases as the hydrothermal environment changes from $H_2SO_4$ to water, 1 M KOH, and 5 % $H_3PO_4$. In the aqueous environment, the LDR block was destroyed into many layers of large and small fragments, appearing messy and quite porous, with fragment sizes varying over a large range (Fig. 3b). In the 1M KOH environment, the LDR block seems to have been destroyed only on the outer layers, forming very small, uniform particles on the surface, while the inner layer remains flaky but intact (Fig. 3c). Meanwhile, the PLH sample (Fig. 3e) consists of relatively small and uniform particles, about 0.2 × 0.4 mm in size, which appear to have been internally destroyed into a porous structure. This degree of destruction is consistent with the change in carbon atom content in the sample, as observed in the EDS spectrum analysis.

The change in material morphology allows for the prediction of the changes in specific surface area of materials. The results are verified by BET analysis in Fig. 4a. The $S_{BET}$ of the SLH sample is very low, at 2.37 $m^2/g$, of KLH is 8.63 $m^2/g$, and of PLH is the highest, 28.73 $m^2/g$, which is 12 times higher than SLH and 3.5 times higher than KLH. The surface area contributed by the cumulative surface area of pores (calculated by BJH method) for SLH, KLH, and PLH is 1.06, 8.67 and 25.82 $m^2/g$, respectively. It means that, the $S_{BET}$ of KLH and PLH samples are mainly due to the contribution of pores while that of SLH sample accounts for less than 50 %. This result is quite consistent with the surface characteristics observed from SEM images. The pore size of PLH sample, calculated from the BJH adsorption and desorption curves, is quite similar, at 36.6 and 30.2 nm, reflecting the mesoporous structure of the material. Table 2 shows that the PLH sample has a relatively high $S_{BET}$ compared to many of the other hydrochars studied. The isoelectric point of PLH was also determined experimentally, as shown in Fig. 4b, with a $pH_{pzc}$ value of 3.5.

**Table 1**
Element composition of LDR and hydrochars were determined by EDS method.

| Atom/Sample | LDR | LH | KLH | SLH | PLH |
|---|---|---|---|---|---|
| C (atomic %) | 62.12 | 72.35 | 75.39 | 64.67 | 77.66 |
| O (atomic %) | 36.79 | 27.05 | 23.64 | 34.08 | 21.71 |

### 3.2. Single adsorption

#### 3.2.1. Some factors affecting to the adsorption of MB and RhB on PLH and the adsorption mechanism

pH is an important factor affecting the chemical forms of MB and RhB, as well as the surface characteristics of PLH, affecting the adsorption capacity of PLH. Adsorption studies were conducted in solutions with pH values of 2, 3, 4, 6, 8, and 10 over a duration of 4 h, with an initial concentration of MB or RhB was 20 mg/L and a PLH dose of 2 g/L. The results are shown in Fig. 5a. For MB adsorption, pH has a strong affection on adsorption capacity: as pH increases from 2 to 4, the adsorption efficiency increases rapidly, but when pH continues to rise, the adsorption efficiency decreases sharply. A similar trend was observed for RhB adsorption; however, the difference in adsorption efficiency between the pH values was not significant, with adsorption efficiencies at pH 3 and 4 being approximately the same. Based on the $pH_{pzc}$ of PLH, at pH values below 3.5, the PLH surface carried a negative charge, and at pH values above 3.5, the surface becomes positively charged. The $pK_a$ values of MB and RhB are 3.8 and 3.7 respectively, meaning that at pH values lower than 3.7, both MB and RhB are not charged and are not attracted to the charged PLH surface. At pH values higher than 3.8, both MB and RhB become positively charged, leading to repulsive interactions with the positively charged PLH surface [55,56]. Furthermore, as $pH > pK_a$, RhB dimer formation increases, which also reduces the adsorption capacity of RhB [57]. Therefore, pH 4 was found to be the optimum pH for single adsorption as well as the mixed adsorption of MB and RhB using PLH.

The effect of PLH dose on the single adsorption of 20 mg/L MB or RhB at pH 4 and 298 K for 4 h was performed at PLH doses of 0.5, 1.0, 2.0, 5.0, and 10.0 g/L, as shown in Fig. 5b. In general, as the PLH dose increased, the adsorption efficiency also increased. However, the increase was more pronounced as the PLH dose increased from 0.1 to 2 g/L. After that, further increases in PLH dose resulted in only a marginal increase in adsorption efficiency, proving that at a concentration of 2 g/L, PLH provided sufficient surface area to achieve near-maximum adsorption of MB or RhB. A PLH dose 2 g/L was then used to evaluate the adsorption capacity of 30 mg/L MB or RhB over time at 298 K and 313 K for 5 to 240 min. The results are shown in Fig. 5c. The adsorption capacity increased gradually over time and reached equilibrium after approximately 120 min. In particular, the adsorption capacity increased with temperature. The results from the study on the effects of time and temperature were used to investigate the kinetic (Fig. 8) and thermodynamic of adsorption process (Table 4). At 25 °C, the adsorption capacity of MB was better than RhB, however at high temperature, the adsorption efficiency of RhB increased significantly, reaching the same level as MB. Both MB and RhB contain functional groups and aromatic rings, but 3D molecular structure of MB is relatively flat, whereas the RhB structure is non-planar (Fig. 6a & b), which reduced the interaction of RhB molecule with the adsorbent surface. As a result, the adsorption efficiency of RhB is typically lower than that of MB. Many other studies have been similar results [27–37]. Temperature may affect the movement of atomic groups, which could lead to changes in the spatial

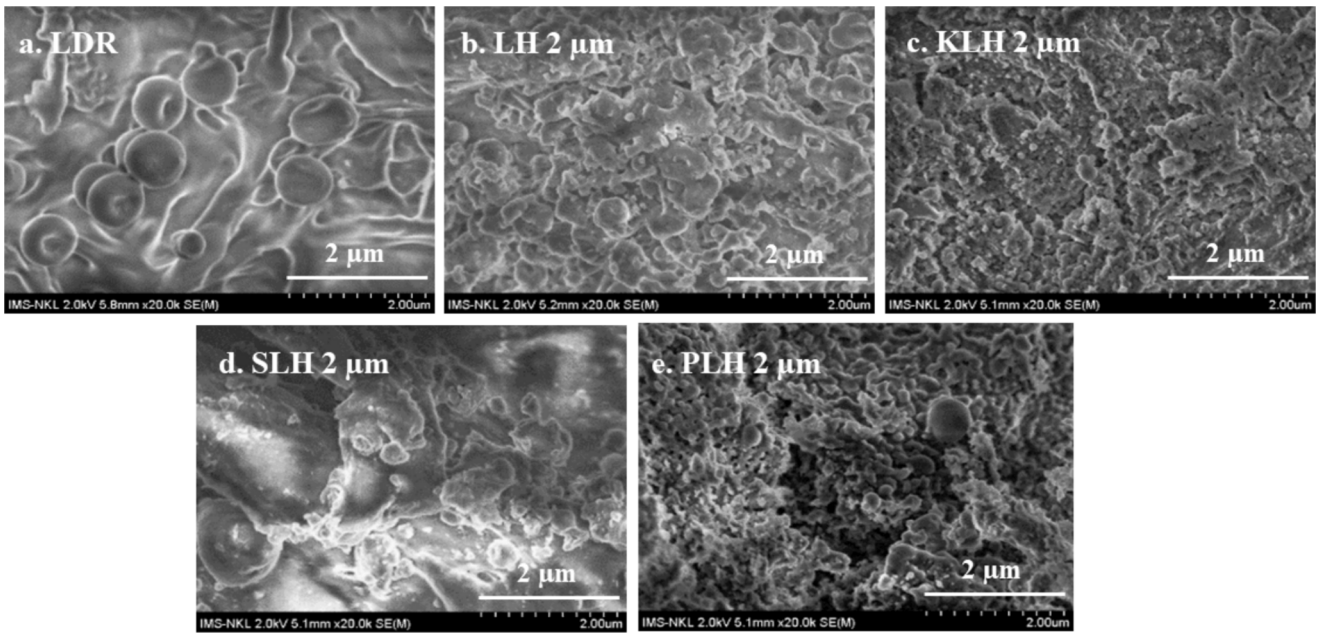


**Fig. 3.** SEM images of a. LDR; b. LH; c. KLS; d. SLH and e. PLH.

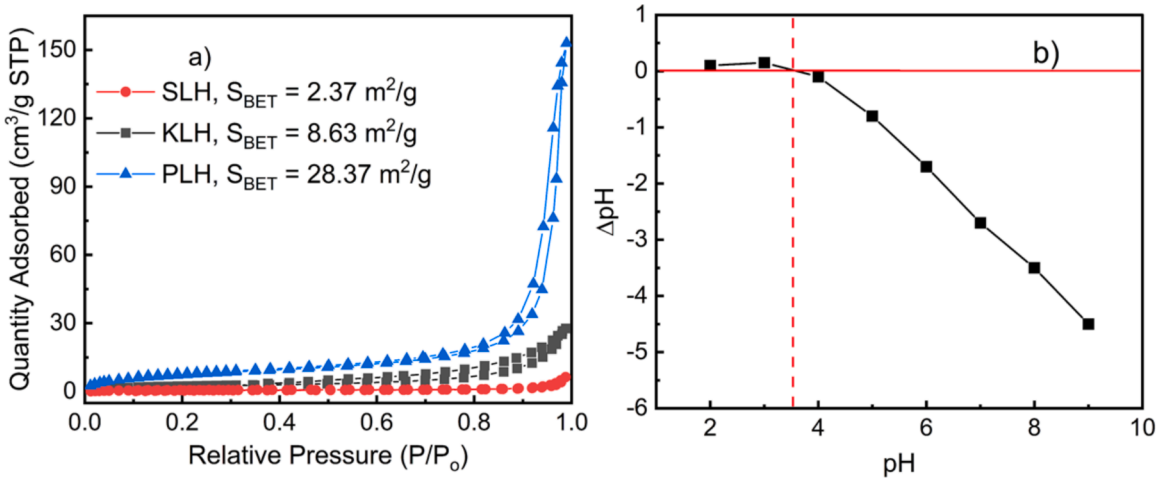


**Fig. 4.** The nitrogen adsorption–desorption isotherm (BET method) of hydrochar materials (a) and $pH_{pzc}$ determination graph of PLH (b).

structure of RhB molecules, thereby increasing their accessibility to the PLH surface and improving the adsorption capacity. The increase in adsorption capacity with temperature is typically due to enhanced chemical interaction between the adsorbent and adsorbate.

The effects of initial adsorbate concentration on adsorption were evaluated at initial dye concentrations of 10, 20, 50, 100, 150, 200, 250, and 300 mg/L, using 2 g/L of PLH at pH 4 and 25 °C for 4 h. The results are shown in Fig. 5d and were used to analyze the adsorption isotherm (Fig. 7 and Table 3). At all initial concentrations, the adsorption capacity of MB was higher than that of RhB. The $q_{m,\,exp}$ for MB was approximately 97 mg/g, while for RhB, it was about 78 mg/g. These values were higher compared to some materials reported in the literature, such as $q_m$ of shea butter leaves for adsorption MB and RhB were 49.27 and 36.06 mg/g, respectively [27]; by cellulose fibers activated biochar was about 84 and 47 mg/g [28]; by $HNO_3$ activated longan peel material were 59.97 mg/g and 32.40 mg/g [29]; by *Pongamia glabra* seed cover biochar were only 1.31 and 0.57 mg/g [30]; by biochar and EDTA modified biochar of palm kernel shells were 7.4 and 7.11 mg/g [31]; by microplastics (polylactic acid and Polyamide 66) before and after UV Irradiation adsorbed RhB and MB, with $q_m$ values of 7.13 mg/g and 14.95 mg/g, respectively [33].

The adsorption mechanism was analyzed using the FTIR spectra of PLH before and after adsorption (Fig. 6). The stretching vibration of O–H group in PLH shifted slightly from 3416 $cm^{-1}$ to 3407 $cm^{-1}$ after adsorption RhB or a mixture of MB and RHB, but it shifted strongly to 3340 $cm^{-1}$ after adsorption MB The spectral broadening was minor after mixed adsorption but became broaden significantly after MB adsorption. It means that a strong hydrogen-bond was formed between the nitrogen in MB and the OH group in PLH [58].

However, this bond was weakened during mixed adsorption, indicating that MB competed significantly with RhB. The C = C stretching vibrations in PLH (at 1640 $cm^{-1}$) shifted to 1620 $cm^{-1}$, 1599 $cm^{-1}$ and 1613 $cm^{-1}$ after adsorption RhB, MB and the mixture of MB and RhB, respectively. The intensity of these peaks increased compared to the original PLH spectrum, due to the C═N stretching in MB and RhB molecules. The changes in the position and intensity of peaks in the 1000 to 1400 $cm^{-1}$ region, such as: peak at 1306 $cm^{-1}$ was enhanced after adsorption, peak at 1221 $cm^{-1}$ decreased after adsorption of RhB but

**Table 2**
Some information of some hydrochars for MB and RhB adsorption.

| No. | Hydrochar | $S_{BET}$ ($m^2/g$) | Dye adsorbed | pH | Adsorption isotherm model | $Q_m$ (mg/g) | References |
|---|---|---|---|---|---|---|---|
| 1 | Mason pine Cedarwood Bamboo Coconut shell Pecan shell Wheat straw | 3.13 | MB | 7 | Langmuir | 156.73 | [14] |
| | Maize straw Rice straw | 3.88 | | | | 94.30 | |
| | | 2.61 | | | | 63.42 | |
| | | 9.62 | | | | 94.53 | |
| | | 5.04 | | | | 106.61 | |
| | | 8.32 | | | | 73.81 | |
| | | 5.81 | | | | 80.66 | |
| | | 6.17 | | | | 6208 | |
| 2 | Coffee husk | 31.30 | MB | | Langmuir | 34.85 | [15] |
| 3 | *Shorea* spp. | 28.69 | MB | – | Sips | 37.80 | [16] |
| 4 | Nut shell | 7.93 | MB | | | 17.92 | [17] |
| 5 | Pomegranate peels | 22.60–25.80 | MB | | Langmuir Freundlich | 37.30–41.19 | [18] |
| 6 | Sewage sludge | 11.91 | MB | | Langmuir | 400.00 | [19] |
| 7 | N-doped corn straw, | 10.59–33.83 | MB | 11 | – | 57.52 | [53] |
| | | | CR | 3 | | 62.19 | |
| 8 | *Sargassum muticum* | 13.18–60.86 | RhB | | – | 17.29–20.77 | [24] |
| 9 | wheat straw | 9.40 | | 6 | | ~40.00 | [25] |
| 10 | Fe- modified wheat straw | 52.74 | | 6 | | 80.00 | |
| 11 | Furfural residue | – | | | – | 39.46 | [26] |
| 12 | Kapok pod | – | | natural | – | 33.34 | [54] |
| 13 | LDR | 28.37 | MB | 4 | Sips | 97 | This study |
| | | | RhB | | | 78 | |

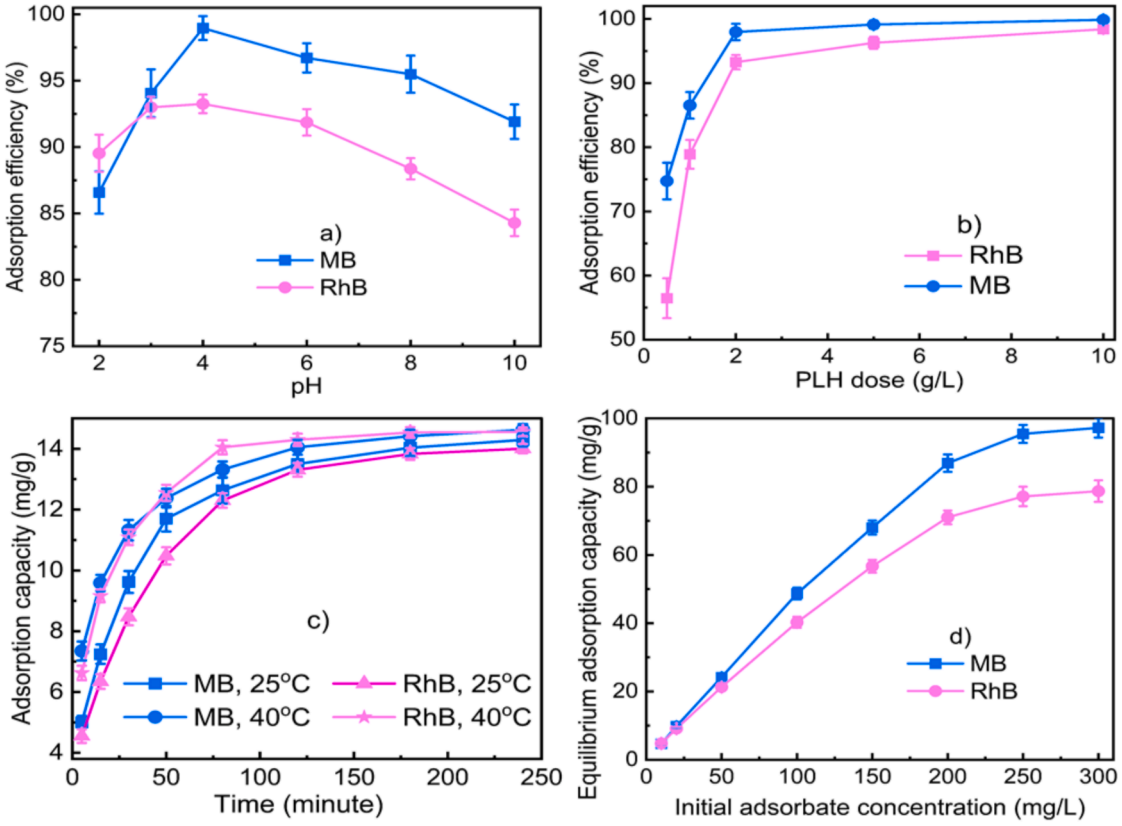


**Fig. 5.** Effect of various factors on the single adsorption capacity of MB and RhB on PLH: a) pH of the solution, b) PLH dose, c) contact time and temperature, d) initial MB/RhB concentration.

slightly shifted after adsorption of MB or mixture, peak at 1162 $cm^{-1}$ increased intensity after adsorption of single MB or RhB but disappeared after mixed adsorption, peak at 1102 $cm^{-1}$ decreased after adsorption of MB and mixture, shoulder peak at 1043 $cm^{-1}$ increased strongly after RhB adsorption but slightly increased after MB adsorption and was no longer observed after MB and RhB mixture adsorption. They confirmed the aromatic ring vibration bands of MB or RhB on PLH. These demonstrated the presence of π-π interactions in the adsorption process [58,59]. Notably, the spectral changes of PLH after mixed adsorption were often intermediate compared to those observed after single adsorption of MB and RhB. This demonstrates that the adsorption preferences of the two dyes differ. The dominant interaction between RhB and PLH involved π-π interactions from aromatic ring, whereas for MB, the primary interactions were π-π interactions from C═N and C═C

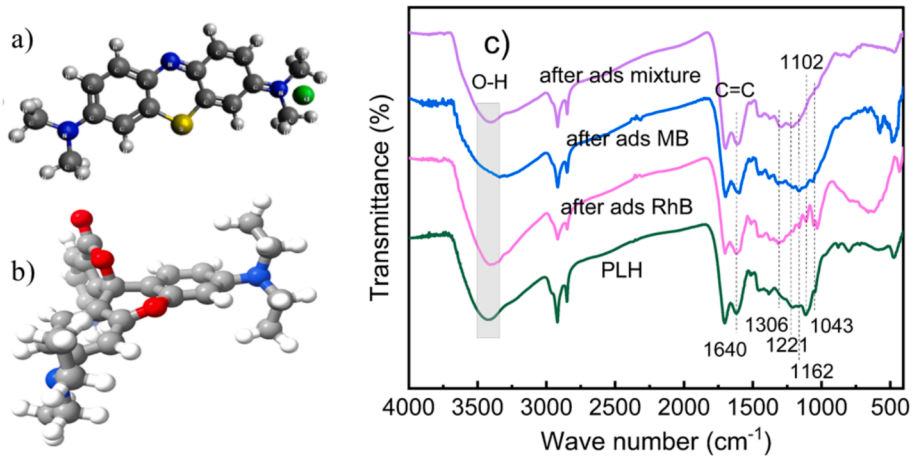


**Fig. 6.** The 3D molecular structures of MB (a) and RhB (b), and the FTIR spectra of PLH before and after adsorption.

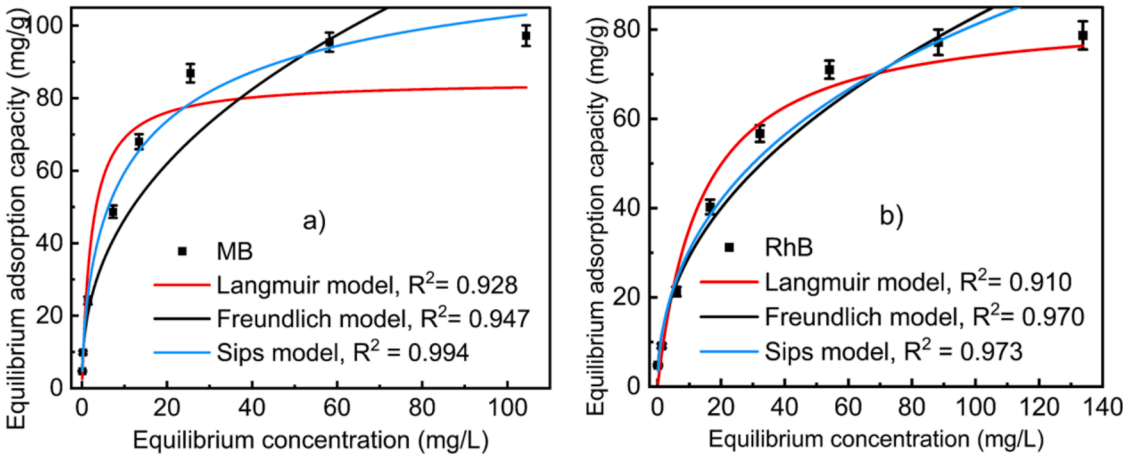


**Fig. 7.** Fitting the single adsorption experimental data of MB (a) and RhB (b) (on 2 g/L PLH at pH 4, 25 °C) to adsorption isotherm models.

**Table 3**
Parameters of adsorption isotherm models for single adsorption of MB and RhB on PLH.

| Model/adsorbate | $q_{e,\,exp}$ (mg/g) | Langmuir | | Freundlich | | Sips | | |
|---|---|---|---|---|---|---|---|---|
| | | $K_L$ | $q_m$ | $K_F$ | $n_F$ | $b_s$ | $K_s$ | $n_s$ |
| MB | ~97 | 0.436 | 84.81 | 17.99 | 0.413 | 0.195 | 25.816 | 0.622 |
| $R^2$ | | 0.928 | | 0.947 | | 0.994 | | |
| RhB | ~78 | 0.072 | 84.23 | 10.280 | 0.453 | 0.035 | 10.417 | 0.515 |
| $R^2$ | | 0.910 | | 0.970 | | 0.973 | | |

in MB to PLH, as well as hydrogen bonding between the nitrogen in MB and the O–H group in PLH.

### 3.2.2. *Research on adsorption isotherm and adsorption kinetic*

Experimental data for single adsorption of MB and RhB at various concentrations (using 2 g/L PLH at 298 K and pH 4) were fitted with the Langmuir, Freundlich, and Sips isotherm models. The results are presented in Fig. 7 and Table 3.

Fig. 7 and Table 3 reveal that, the correlation coefficient $R^2$ for the Langmuir model is the lowest, while that for the Sips is the highest. The Sips isotherm model was developed as combination of the Langmuir and Freundlich isotherm models, relating to the distribution of adsorption on a heterogeneous surface of the adsorbent [60]. These results demonstrate that the first adsorption layer is essentially chemical adsorption, followed by physical adsorption layers. The adsorption mechanism includes chemisorption and physisorption. Furthermore, the surface of PLH is heterogeneous.

The kinetic of the experimental single adsorption process were studied using the PFO, PSO, and Elovich kinetic models, the results are shown in Fig. 8 and Table 4.

Table 4 shows that, all the adsorption rate constants, according to all models, increased with temperature, and those for MB were higher than for RhB. The equilibrium adsorption capacities calculated using the PFO and PSO kinetic equations ($q_{e1,cal}$ and $q_{e2,cal}$) had relatively small errors compared to the experimental equilibrium adsorption capacity ($q_{e,exp}$). However, the $q_{e1,cal}$ always exhibited negative errors, while the $q_{e2,cal}$ always showed positive errors. About the $R^2$ for PFO, PSO, and Elovich kinetic models ($R_1^2$, $R_2^2$ and $R_E^2$, respectively) for both MB and RhB: $R_1^2$ was always much smaller than $R_2^2$. For MB adsorption the $R_E^2$ is the highest. For RhB adsorption, $R_{E,\,25}^2$ was insignificantly higher than $R_{2,25}^2$, but $R_{2,40}^2$ was noticeably higher than $R_{E,40}^2$. However, the highest $R^2$ value for MB adsorption was 0.988, and for RhB it was 0.973, indicating

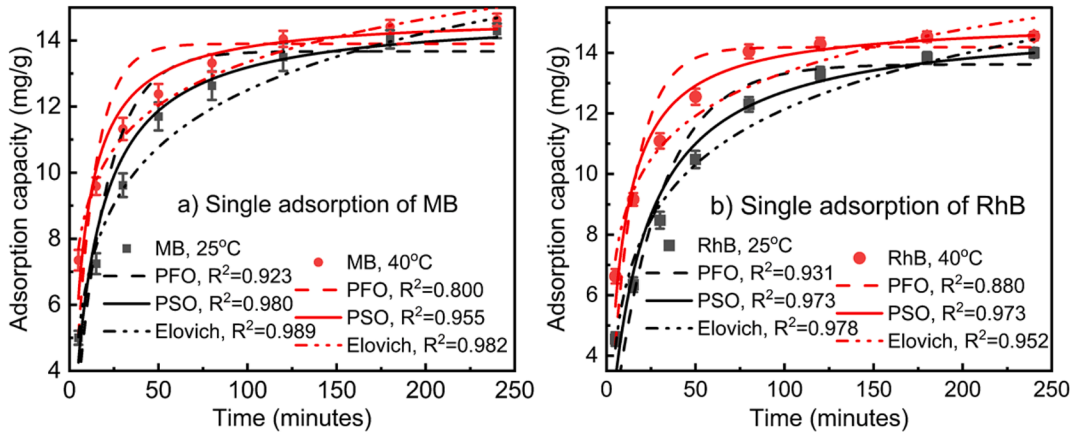


**Fig. 8.** Fitting the single adsorption experimental data of 30 mg/L MB (a) and 30 mg/L RhB (b) (onto 2 g/L PLH at pH 4, 25 °C and 40 °C) to adsorption kinetic models.

**Table 4**
Kinetic and thermodynamic parameters for single adsorption of MB and RhB on PLH.

| Adsorbate | Kinetic parameters | Single adsorption | | | | Mixed adsorption | | | |
|---|---|---|---|---|---|---|---|---|---|
| | | MB ($C_o$ = 30 mg/L) | | RhB ($C_o$ = 30 mg/L) | | MB ($C_o$ = 10 mg/L) | | RhB ($C_o$ = 10 mg/L) | |
| | | 298 K | 313 K | 298 K | 313 K | 298 K | 313 K | 298 K | 313 K |
| | $q_{e,exp}$ (mg/g) | 14.29 | 14.62 | 14.00 | 14.56 | 4.61 | 4.74 | 4.43 | 4.65 |
| PFO | $q_e$ (mg/g) | 13.67 | 13.90 | 13.62 | 14.19 | 4.58 | 4.70 | 4.41 | 4.60 |
| | Error (%) ($q_{e,e}$&$q_{e,c}$) | −4.35 | −4.94 | −2.72 | −2.52 | −0.57 | −0.95 | −0.41 | −0.93 |
| | $k_1$ ($min^{-1}$) | 0.058 | 0.090 | 0.038 | 0.074 | 0.075 | 0.071 | 0.114 | 0.075 |
| | $R_1^2$ | 0.923 | 0.800 | 0.931 | 0.880 | 0.942 | 0.895 | 0.847 | 0.831 |
| PSO | $q_e$ (mg/g) | 14.82 | 14.76 | 15.09 | 15.09 | 4.80 | 4.92 | 4.54 | 4.80 |
| | Error (%) ($q_{e,e}$&$q_{e,c}$) | 3.72 | 0.94 | 7.72 | 3.66 | 4.17 | 3.68 | 2.39 | 3.21 |
| | $k_2$ ($g.mg^{-1}.min^{-1}$) | 0.005 | 0.010 | 0.004 | 0.008 | 0.024 | 0.024 | 0.043 | 0.028 |
| | $R_2^2$ | 0.980 | 0.955 | 0.973 | 0.973 | 0.985 | 0.972 | 0.972 | 0.949 |
| Elovich | $k_e$ (g/mg) | 0.401 | 0.529 | 0.380 | 0.485 | 1.487 | 1.565 | 2.257 | 1.741 |
| | a ($mg.g^{-1}.min^{-1}$) | 3.74 | 22.08 | 2.64 | 13.36 | 3.16 | 5.10 | 47.96 | 8.93 |
| | $R_E^2$ | 0.989 | 0.982 | 0.978 | 0.952 | 0.932 | 0.940 | 0972 | 0.916 |
| Thermodynamic | $K_C$ | 20.21 | 38.84 | 11.57 | 32.31 | 15.71 | 30.46 | 12.39 | 33.06 |
| | ΔG (KJ/mol) | −7.448 | −9.523 | −6.067 | −9.044 | −6.824 | −8.890 | −6.236 | −9.103 |
| | ΔH (KJ/mol) | 33.765 | | 53.076 | | 34.227 | | | |
| | | | | | | | | 50.723 | |

that MB or RhB adsorption on PLH was a complex process rather than a straight forward first or second-order reaction. The experimental data partially fitted the PFO, PSO or Elovich models, with better fits observed for the Elovich kinetic model for MB and the PSO kinetic model for RhB. All these results suggest that the PLH surface is energetically heterogeneous [61].

### 3.3. Mixed adsorption

RhB:MB mixtures at molar ratios of 2:1, 4:3, 2:3, and 1:3 (corresponding to initial mass ratios of approximately 15/5; 20/10; 10/10 and 10/20 mg/L/dye) were evaluated for mixed adsorption capacity after 4 h at 25 °C and pH 4. These results were compared with the single adsorption at the same initial concentrations and conditions. The results are presented in Fig. 9. The $q_{e,m}/q_{e,s}$ ratio (the ratio of the equilibrium adsorption capacity of each adsorbate in mixed adsorption $q_{e,m}$ to that in single adsorption $q_{e,s}$) is listed in Table 5.

Fig. 9 and Table 5 show that, the equilibrium adsorption capacity in mixed adsorption was lower compared with single adsorption at different initial mole ratios. For MB, the $q_{e,m}/q_{e,s}$ ratio at initial concentrations was lower or higher than for RhB (mole ratio of RhB/MB = 2:1 or 1:3, corresponding to the initial mass concentration of MB was of 5 mg/L or 20 mg/L, and the reduction was stronger than when the initial concentrations were approximately (mole ratio of RhB/MB = 4:3 or 2:3, with the initial MB concentration of 10 mg/L). It means that when the initial concentration is low, MB is more strongly overwhelmed, but when the initial concentration is higher, MB is not only competed by RHB molecules but can also competes with other MB molecules, as both are relatively bulky organic molecules. For RhB, the $q_{e,m}/q_{e,s}$ ratio was highest when the mole ratio of RhB/MB was 4:3, as the initial concentration of RhB was highest (20 mg/L). As initial mass concentration and mole ratios of RhB in the mixture decreased, the $q_{e,m}/q_{e,s}$ ration also decreased, indicating stronger competitively adsorption. The $q_{e,m}/q_{e,s}$ ration for RhB was smaller than for MB, proving that RhB competes more strongly than MB. This can be easily explained by the bulkier spatial structure of RhB compared to MB. However, this reduction is insignificant compared to many studies on the adsorption of MB and RhB mixtures on other materials. For example, $q_m$ of alkaline-modified Vietnam diatomite in individual adsorption of of MB and RhB was $7.14.10^{-4}$ mol/g and $3.10^{-4}$ mol/g (equal 228.48 mg/g and 143.7 mg/g) respectively, $q_m$ strongly decreased in mixed adsorption, down to $4.55.10^{-4}$ and $1.4.10^{-4}$ mol/g (equal 145.60 and 67.06 mg/g), reduced about 35 % and 53 % [33]; or commercial natural zeolite from deposits in Semnan, Iran, the $q_m$ in single adsorption at 298 K was $6.4.10^{-5}$ and $1.15.10^{-5}$ mol/g (equal 20.48 and 5.51 mg/g) for MB and RhB, respectively, reduced by 50 % and 60 % in binary adsorption [34]; or a pyrochar of cassava peel in single and binary adsorption of MB, malachite green, and RhB, the $q_m$ in single adsorption for MB and RhB were 286.41 mg/g and 265.36 mg/g, respectively, strongly decreased in binary adsorption, for MB and RhB were 51.07 mg/g (17.8 %) and 4.82 mg/g (1.8 %), respectively [37].

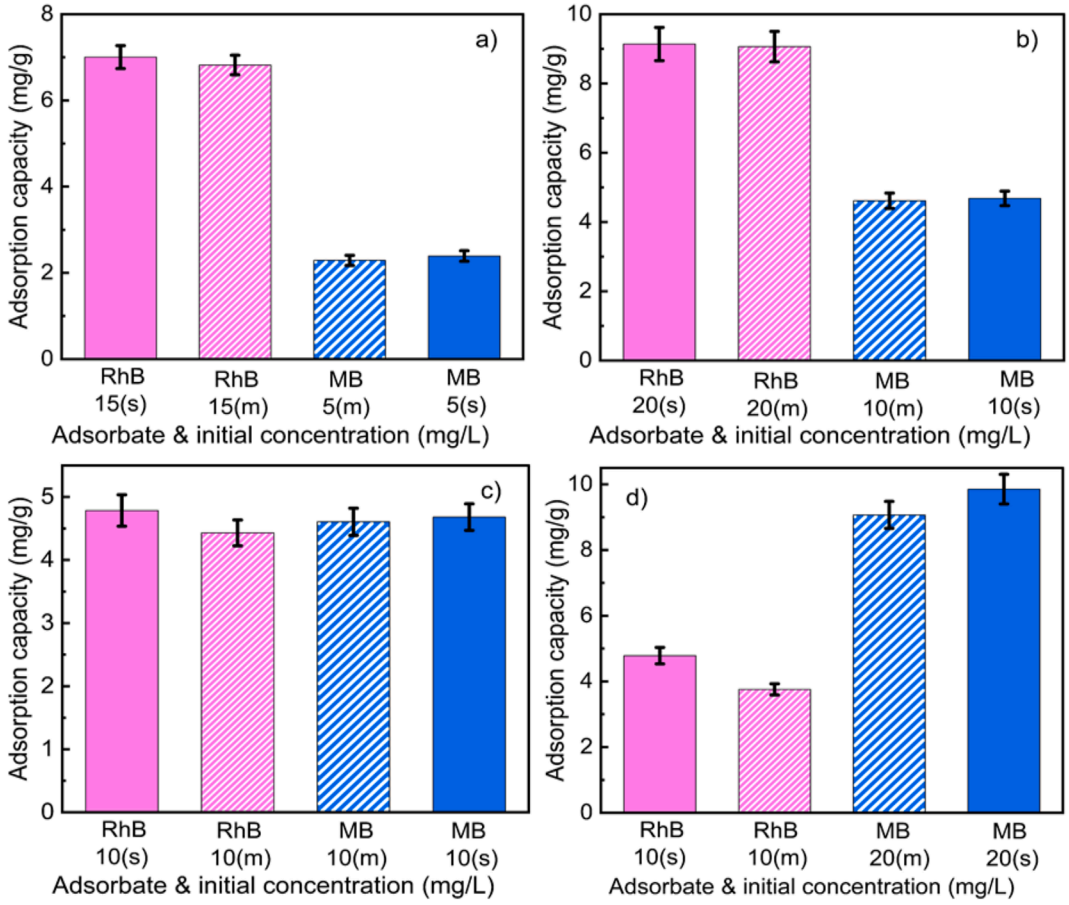


**Fig. 9.** The equilibrium adsorption capacity for single adsorption (s) and mixed adsorption (m) of each adsorbate when the mixture has different initial mole ratios of RhB/MB of 2:1 (a), 4:3 (b), 2:3 (c) and 1:3 (d).

**Table 5**
The The $q_{e,m}/q_{e,s}$ ratio of MB and RhB adsorption on 2 g/L PLH at different initial mole concentration ratios (pH 4, 240 min, 298 K).

| Adsorbate | $q_{e,m}/q_{e,s}$ at different initial mole ratios of RhB/MB | | | |
|---|---|---|---|---|
| | 2:1 | 4:3 | 2:3 | 1:3 |
| MB | 0.958 | 0.986 | 0.984 | 0.921 |
| RhB | 0.974 | 0.992 | 0.926 | 0.785 |

The effect of time and temperature on the adsorption capacity of MB and RhB mixture by 2 g/L PLH was studied using a mixture of 10 mg/L/dye at pH 4, 25 °C, and 40 °C, over a time from 0 to 240 min. These experimental data were used to study the adsorption kinetic according to the PFO, PSO and Elovich kinetic models. The results are shown in Fig. 10 and Table 4.

Table 4 and Fig. 10 show that, although the $q_{e1,cal}$ was approximately to $q_{e,exp}$, there was always a negative error the value of $k_{1,T2}$ was smaller than $k_{1,T1}$, while $q_{e1,T2}$ was higher than $q_{e1,T1}$. Additionally, the $R_1^2$ was the lowest compared to $R_2^2$ and $R_E^2$, indicating that the adsorption

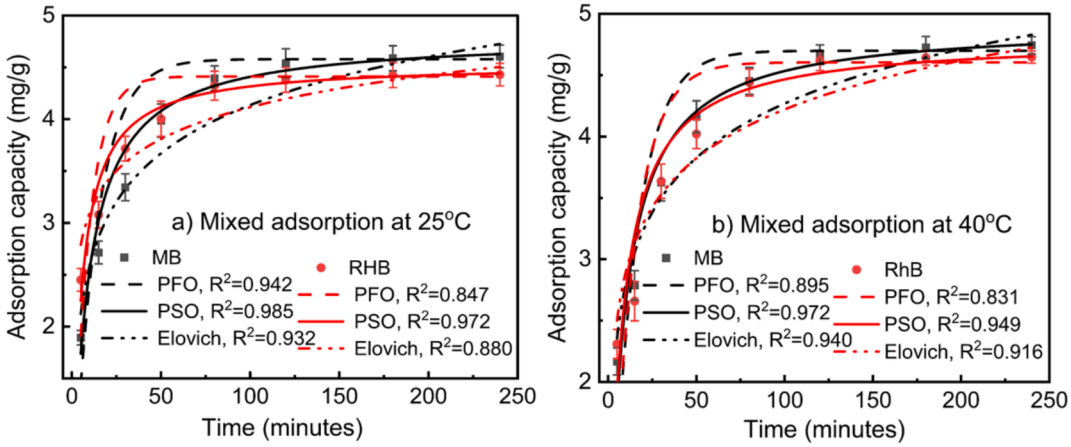


**Fig. 10.** Fitting of mixed adsorption experimental data (10 mg/L/dye on 2 g/L PLH at pH 4) at 25 °C (a) and 40 °C (b) to adsorption kinetic models.

kinetics of MB and RHB in the mixed adsorption do not follow the first-order kinetic model. For the adsorption of RhB in mixture, similar to single adsorption, the values of $R^2_{2,T1}$ and the $R^2_{E,T1}$ was the same, and $R^2_{2,T2}$ was higher than $R^2_{E,T2}$, but the value of $R^2_2$ was only 0.949 and 0.972. This means that the experimental mixed adsorption of RhB on PLH best fits the PSO kinetic model, although the adsorption process is a complex process than a straightforward second-order reaction. For the the adsorption of MB in the mixture, unlike single adsorption, $R^2_2$ was noticeably higher than $R^2_E$ at both temperatures. The errors of $q_{e2,cal}$ were small compared to the $q_{e,exp}$ and were positive. Additionally the $k_{2,T2}$ was higher than $k_{2,T1}$, all of these factors proved that the experimental mixed adsorption of MB on PLH best fits the PSO kinetic model. An increase in MB and RhB adsorption capacity with temperature has also been observed in several studies, such as by of alkaline-modified Vietnam diatomite [34] or commercial natural zeolite from deposits in Semnan, Iran [35].

### 3.4. The adsorption thermodynamic

Table 4 shows that, the Gibbs free-energy (ΔG) values of the single or mixed adsorption processes of MB and RhB by PLH material all have negative, meaning that these processes are spontaneous and thermodynamically favorable. The enthalpy (ΔH) of RhB and MB adsorption both in single and in mixture were all positive, means that adsorption process were endothermic. Theoretically, $\Delta H > 0$, adsorption increases as temperature increases, and the experimental results obtained were also correct. The ΔH values of MB adsorption were about 33–34 kJ/mol, means that, the nature of adsorption interactions is intermediate between physics and chemistry, of adsorption mechanism of MB on PLH includes chemisorption and physisorption. But the ΔH values of RhB adsorption were about 50–53 kJ/mol, means that the interaction between RhB and PLH was mainly chemical interaction. The efficiency of RhB was smaller than MB due to the influence of spatial effects.

### 3.5. The reusability

The reuse of PLH was conducted with four adsorption – desorption cycles, including both single adsorption of 20 mg/L MB, 20 mg/L RhB and mixed adsorption of MB and RhB (10 mg/L/adsorbate) at 25 °C, pH 4 for 4 h. The results are exhibited on the Fig. 11.

For single adsorption of both MB and RhB, the adsorption capacity slightly increased after each cycle, while the mixed adsorption capacity slightly decreased after each cycle. Typically, studies show a slightly decrease in adsorption capacity after each reuse cycle [62] or quickly decreased [63,64] or insignificant decrease for MB but rapid decrease for RhB [37], an increase is rare [36].

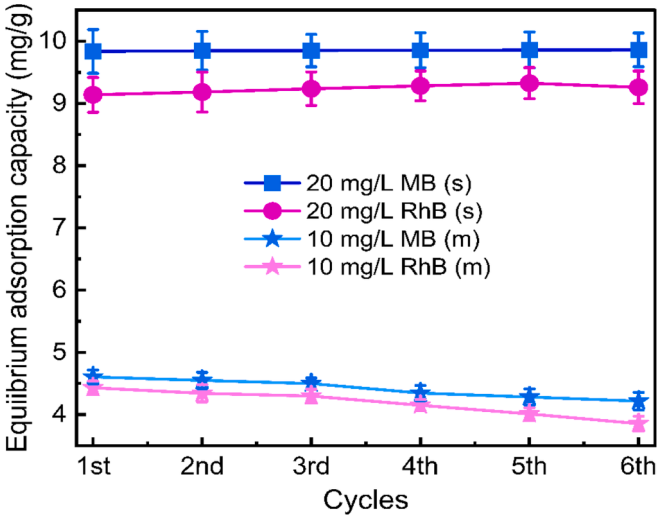


**Fig. 11.** Adsorption capacity of PLH during adsorption/desorption cycles.

The increase in adsorption capacity after regeneration and reuse is an unexpected result that has not been reported in previous studies. Many previously studies have evaluated the regeneration of hydrochar after adsorption of various dyes, using common solvents as HCl, NaOH, ethanol, acetic acid, NaCl, and NaCl in Methanol, … In which, organic solvents were often used when the physical adsorption occurred, while inorganic solvents were selected for chemisorption. In some cases, using 0.1 M HCL showed very high reusability in MB adsorption, such as hydrochar of *Lavandin* straws showed nearly 100 % efficiency after the first reuse and still 96 % after the sixth reuse [65]. Similarly, the hydrochar of persimmonpeel@montmorillonite for MB adsorption retained 94.95 % efficiency after the fifth reuse [66]. These results indicated that, 0.1 M HCl was not only an effective hydrochar regenerator but also an activator, enhancing the MB adsorption capacity of PLH.

To regenerate RhB adsorbent, many solvents have been tested, NaOH solution has shown high regeneration and reuse ability. Magnetic hollow carbon microspheres remained the RhB removal efficiency of over 90 % after six reuse cycles [45], However, pyrochar from *Calophyllum inophyllum* seeds was only regenerated with NaOH solution. After four reuse cycles, the RhB adsorption efficiency decreased from 95.5 % to 56.4 % [67]. It is clear that the recycling process and the nature of the adsorbent have an important influence on the reuse efficiency. For PLH, the recycling process with NaOH solution was repeated many times to ensure effective recycling, along with the calcination process similar to pyrolysis in pyrochar production, which contributes to the activation of the material, thus increasing the reuse efficiency.

However, for material after mixed adsorption, using ethanol as the regeneration solvent may not have achieved the same recycling efficiency as NaOH or HCl solutions, so the adsorption capacity decreased slightly after each regeneration. Furthermore, the competitive adsorption between MB and RhB also contributed to the reduction of the mixed adsorption efficiency. Nevertheless, the equilibrium adsorption capacity only decreased from about 4.55 to 4.22 mg/g for MB adsorption and from about 4.43 to 3.85 mg/g for RhB adsorption after six cycles, which was still a small decrease, indicating the very good reusability of the PLH material.

## 4. Conclusion

Hydrothermal environment had important influence on the properties of hydrochar prepared from LDR. The carbonization degree, carbon content in the sample, physical destruction level of the original sample, specific surface area increased gradually according to changes in hydrothermal solution: DW, 1 M $H_2SO_4$, 1 M KOH, to 5 % $H_3PO_4$. The PLH sample consists of relatively small and most uniform particles, about 0.2x0.4 mm in size, with the most porous structure and largest specific surface area, 28.37 $m^2/g$. PLH samples was choose to evaluate the single and mixed adsorption MB and RhB. The optimal adsorption was at pH 4, 120 to 180 min, adsorbent dose increased and initial concentration of MB and RhB decreased. The maximum sorption capacity for MB and RhB were about 97 and 78 mg/g, respectively, insignificantly reduced in mixed adsorption at different mole ratios. The sorption capacity after regeneration increased slightly in individual adsorption and decreased slightly in mixed adsorption after six cycles. The single adsorption followed the Sips isotherm model, the surface of PLH is heterogeneous. Both single adsorption and mixed adsorption were well fitted with the pseudo-second-order kinetic model, spontaneous, and endothermic, the dominant interaction between RhB and PLH involved π-π interactions from aromatic ring, while for MB were π-π interactions from C═N and C═C in MB to PLH, and the hydrogen bonding between the nitrogen in MB and the O–H group in PLH. All the results indicate that the hydrochar of lemongrass essential oil distillation residue is an efficient adsorbent

with high adsorption capacity for MB and RhB both in single and mixed adsorption. In the near future, we continues to study about the conditions for manufacturing biochar from LDR, expand the assessment to adsorb other pollutants and the possibility of practical application, study in detail the material regeneration, evaluate the economic value of adsorbents and application processed.

## CRediT authorship contribution statement

**Thi Thu Uyen Le:** Writing – original draft, Investigation, Data curation. **Thi Giang Ngo:** Investigation. **Ngoc Anh Hoang:** Investigation. **Van Hao Nguyen:** Validation, Methodology. **Van Dang Nguyen:** Validation, Methodology. **Le Phuong Hoang:** Writing – review & editing, Data curation. **Tien Duc Pham:** Writing – review & editing, Validation, Conceptualization. **Thi Thao Truong:** Writing – review & editing, Writing – original draft, Visualization, Supervision, Project administration, Data curation, Conceptualization.

## Funding

This research was partially supported by the TNU-University of Sciences under the project code: CS2024-TN06-17.

## Declaration of competing interest

The authors declare that they have no known competing financial interests or personal relationships that could have appeared to influence the work reported in this paper.

## Data availability

No data was used for the research described in the article.

## References

[1] K. Awasthi, K, Padwekar, S. C. Misra, Chapter 7: Industry 4.0 in the Textile Sector: Applications, Influencing Factors, and Opportunities, In: S. Singh, S. Gupta, S. Jagtap, Futuristic Technology for Sustainable Manufacturing, IGI Global Scientific Publishing, New York, 2024, pp.110-125. doi: 10.4018/979-8-3693-1862-1.ch007.
[2] M. Phagare, Chapter 1: Global Market Analysis, in book: Global Dyes and Pigments Market Report 2024 (Global Edition), Cognitive Market Research Company Profile, update 12/29/2024. https://www.cognitivemarketresearch.com/dyes-and-pigments-market-report?.
[3] P.O. Oladoye, T.O. Ajiboye, E.O. Omotola, O.J. Oyewola, Methylene blue dye: Toxicity and potential elimination technology from wastewater, Results Eng. 16 (2022) 100678, https://doi.org/10.1016/j.rineng.2022.100678.
[4] M. Bużga, E. Machytka, E. Dvořáčková, Z. Švagera, D. Stejskal, J. Máca, J. Král, Methylene blue: a controversial diagnostic acid and medication? Toxicol. Res. 11 (5) (2022) 711–717, https://doi.org/10.1093/toxres/tfac050.
[5] N. Bar, P. Chowdhury, A Brief Review on Advances in Rhodamine B Based Chromic Materials and Their Prospects, ACS Appl. Electron. Mater. 4 (8) (2022) 3749–3771, https://doi.org/10.1021/acsaelm.2c00107.
[6] S. Dumbare, A. Doshi, S. Ravindran, Rhodamine B and Rhodamine 6G Based Sensing of Copper Ions in Environmental and Biological Samples: Recent Progress, Pol. J. Environ. Stud. 30 (4) (2021) 3445–3455, https://doi.org/10.15244/pjoes/130572.
[7] S. Sulastri, Review Artikel: Analisis Kandungan Rhodamin B Dalam Makanan Dan Minuman, COMSERVA: Jurnal Penelitian dan Pengabdian Masyarakat. 2(10) (2023) 2429-2435. doi: 10.59141/comserva.v2i10.701.
[8] F.A. Saputri, B.P. Irinda, R. Pratiwi, Review] analisis Rhodamin B Dalam makanan, Indonesia J. Pharmaceut. Sci. Technol. 7 (1) (2018) 50–58, https://doi.org/10.58327/jstfi.v7i1.74.
[9] M.A. Mohammed, A. Shitu, A. Ibrahim, Removal of Methylene Blue Using Low Cost Adsorbent: A Review, Res. J. Chem. Sci. 4 (1) (2014) 91–102. https://www.researchgate.net/publication/267737463.
[10] A.M. Bożęcka, M.M. Orlof-Naturalna, M. Kopeć, Methods of Dyes Removal from Aqueous Environment, J. Ecol. Eng. 22 (9) (2021) 111–118, https://doi.org/10.12911/22998993/141368.
[11] M. Rafatullah, O. Sulaiman, R. Hashim, A. Ahmad, Adsorption of methylene blue on low-cost adsorbents: a review, J. Hazard. Mater. 177 (1–3) (2010) 70–80, https://doi.org/10.1016/j.jhazmat.2009.12.047.
[12] E. Santoso, R. Ediati, Y. Kusumawati, H. Bahruji, D.O. Sulistiono, D. Prasetyoko, Review on recent advances of carbon based adsorbent for methylene blue removal from waste water, Mater. Today Chem. 16 (2020) 100233, https://doi.org/10.1016/j.mtchem.2019.100233.
[13] H.S. Kusuma, J.D.E. Christa, N. Illiyanasafa, K.L. Ikawati, E. Kurniasari, H. Darmokoesoemo, A.N. Amenaghawon, A critical review and bibliometric analysis of methylene blue adsorption using leaves, Chemosphere 356 (2024) 141867, https://doi.org/10.1016/j.chemosphere.2024.141867.
[14] X. Zhang, F. Chen, S. Liu, Synthesis, characterization, and methylene blue adsorption isotherms of hydrochars derived from forestry waste and agro-residues, Biomass Conv. Bioref. 14 (2024) 1809–1824, https://doi.org/10.1007/s13399-021-02241-y.
[15] A. Ronix, O. Pezoti, L.S. Souza, I.P.A.F. Souza, K.C. Bedin, P.S.C. Souza, Hydrothermal carbonization of coffee husk: Optimization of experimental parameters and adsorption of methylene blue dye, J. Environ. Chem. Eng. 5 (2017) 4841–4849, https://doi.org/10.1016/j.jece.2017.08.035.
[16] M. Elhassan, M.R.R. Kooh, C.Y.E. Chou, R. Abdullah, Hydrochar from Shorea spp.: a dual-purpose approach for sustainable biofuel and efficient methylene blue adsorbent, Biomass– Convers Biorefnery (2024), https://doi.org/10.1007/s13399-024-05376-w.
[17] I. Teğin, M.F. Demirel, I. Alacabey, E. Yabalak, Investigation of the effectiveness of waste nut shell–based hydrochars in water treatment: a model study for the adsorption of methylene blue, Biomass Conv. Bioref. 14 (2024) 10399–10412, https://doi.org/10.1007/s13399-022-02996-y.
[18] M. Hessien, Methylene Blue Dye Adsorption on Iron Oxide-Hydrochar Composite Synthesized via a Facile Microwave-Assisted Hydrothermal Carbonization of Pomegranate Peels' Waste, Molecules 28 (11) (2023) 4526, https://doi.org/10.3390/molecules28114526.
[19] L. Chen, D. Li, W. Zhu, C. Xu, Y. Ding, Y. Huang, Adsorption properties of sludge-hydrochar for methylene blue, Environ. Sci. 41 (4) (2020) 1761–1769, https://doi.org/10.13227/j.hjkx.201908198.
[20] W.C. Qian, X.P. Luo, X. Wang, M. Guo, B. Li, Removal of methylene blue from aqueous solution by modified bamboo hydrochar, Ecotoxicol. Environ. Saf. 157 (2018) 300–306, https://doi.org/10.1016/j.ecoenv.2018.03.088.
[21] X. Duan, W. Hong, C. Srinivasakannan, X. Wang, Hydrochar silicate composite sorbent via simple hydrothermal carbonization and its application to methylene blue removal, Mater. Res. Express 6 (2019) 035601 doi: 1088/2053-1591/aaf44f.
[22] A.A. Al-Gheethi, Q.M. Azhar, K.P. Senthil, A.A. Yusuf, A.K. Al-Buriahi, R.M.S. R. Mohamed, M.M. Al-Shaibani, Sustainable approaches for removing Rhodamine B dye using agricultural waste adsorbents: A review, Chemosphere 287 (P2) (2022) 132080, https://doi.org/10.1016/j.chemosphere.2021.132080.
[23] S.S. Imam and H.F. Babamale; A Short Review on the Removal of Rhodamine B Dye Using Agricultural Waste-Based Adsorbents, AJOCS. 7(1) (2020) 25-37, No. *AJOCS.54033,* doi: 10.9734/AJOCS/2020/v7i119013.
[24] D. Spagnuolo, D. Lannazzo, T. Len, A.M. Balu, M. Morabito, G. Genovese, C. Espro, V. Bressi, Hydrochar from Sargassum muticum: a sustainable approach for high-capacity removal of Rhodamine B dye, RSC Sustain. 1 (2023) 1404–1415, https://doi.org/10.1039/d3su00134b.
[25] S. Kohzadi, N. Marzban, J.A. Libra, M. Bundschuh, A. Maleki, Removal of RhB from water by Fe-modified hydrochar and biochar – An experimental evaluation supported by genetic programming, J. Mol. Liq. 369 (2023) 120971, https://doi.org/10.1016/j.molliq.2022.120971.
[26] X. Li, Q. Zhu, K. Pang, Z. Lang, Effective removal of Rhodamine B using the hydrothermal carbonization and citric acid modification of furfural industrial processing waste, Environ. Technol. 45 (17) (2023) 3303–3314, https://doi.org/10.1080/09593330.2023.2215451.
[27] A. Shehu, M.B. Ibrahim, Equilibrium adsorption isotherm of methylene blue and rhodamine B using shea butter leaves as a low-cost adsorbent, Appl. J. Envir. Eng. Sci. 9 (1) (2023) 1–15, https://doi.org/10.5281/zenodo.8052800.
[28] R. Wolski, A. Bazan-Wozniak, A. Nosal-Wiercińska, R. Pietrzak, Methylene Blue and Rhodamine B Dyes' Effcient Removal Using Biocarbons Developed from Waste, Molecules. 29 (17) (2024) 4022, https://doi.org/10.3390/molecules29174022.
[29] D. Kurniawati, E.D. Ramadhani, R.K. Ali, M. Khair, U.K. Nizar, E. Nasra, T.K. Sari, Effect of Particle Size and Mass of Longan Peel (Euphoria Longan L.) as Adsorbent on The Adsorption of Rhodamine B and Methylene Blue Dyes Using the Column Method, J. Phys. Conf. Ser. 2582 (2023) 012034, https://doi.org/10.1088/1742-6596/2582/1/012034.
[30] N. Bordoloi, M.D. Dey, R. Mukhopadhyay, R. Kataki, Adsorption of Methylene blue and Rhodamine B by using biochar derived from Pongamia glabra seed cover, Water Sci. Technol. 77 (3) (2018) 638–646, https://doi.org/10.2166/wst.2017.579.
[31] N.L.B. Kouassi, A. Abollé, A.R. Kouakou, V. Gogbe, A. Trokourey, Using Modified Activated Carbon to Remove Methylene Blue and Rhodamine B from Wastewater, Am. J. Phys. Chem. 12 (3) (2023) 30–40, https://doi.org/10.11648/j.ajpc.20231203.11.
[32] D.L. Postai, C.A. Demarchi, F. Zanatta, D.C.C. Melo, C.A. Rodrigues, Adsorption of rhodamine B and methylene blue dyes using waste of seeds of Aleurites Moluccana, a low cost adsorbent, Alex. Eng. J. 55 (2) (2016) 1713–1723, https://doi.org/10.1016/j.aej.2016.03.017.
[33] J. Li, K. Wang, K. Wang, S. Liang, C. Guo, A. Hassan, J. Wang, Adsorption behavior of Methylene Blue and Rhodamine B on microplastics before and after ultraviolet irradiation, Colloids Surf. A Physicochem. Eng. Asp 699 (2024) 134671, https://doi.org/10.1016/j.colsurfa.2024.134671.
[34] P.D. Du, H.T. Danh, Single and Binary Adsorption Systems of Rhodamine B and Methylene Blue onto Alkali-Activated Vietnamese Diatomite, Adsorpt. Sci. Technol. 2021 (2021) 1014354, https://doi.org/10.1155/2021/1014354.
[35] F. Jafari-zare, A. Habibi-yangjeh, Competitive Adsorption of Methylene Blue and Rhodamine B on Natural Zeolite, Chin. J. Chem . 28 (2010) 349–356.
[36] E.M. Rolim, A.M.B. Silva, B.J. Santos, Removal of rhodamine B and methylene blue using residual *Onecarpus bacaba* Mart fibers as biosorbent: kinetic and

thermodynamic parameters, Discov Water. 4 (2024) 13, https://doi.org/10.1007/s43832-024-00058-0.
[37] A. Belcaid, B.H. Beakou, S. Buscotin, A. Anouar, Insight into adsorptive removal of methylene blue, malachite green, and rhodamine B dyes by cassava peel biochar (Manihot esculenta Crantz) in single, binary, and ternary systems: competitive adsorption study and theoretical calculations, Biomass Convers. Biorefin. 14 (2024) 7783–7806, https://doi.org/10.1007/s13399-022-02928-w.
[38] H. Channayya, Da Nagegowda, K. Baskaran, R.S Verma, V. Sundaresan, P. Gupta, K.V Ashwini, S. Singh, G.M. R Swamy, A.C Jnanesha, P.K Trivedi, Registration of high oil-yielding lemongrass (Cymbopogon flexuosus Steud.) Wats Variety CIM-Krishnapriya, J. Med. Aromatic Plant Sci., 45(1-2) (2023) 70-78. doi: 10.62029/jmaps.v45i2.channayya.
[39] G. Agegnehu, K. Jemal, A. Abebe, B. Lulie, Plant Growth and Oil Yield Response of Lemon Grass (Cymbopogon citratuc L.) to Biochar Application, Ethiop. J. Agric. Sci. 29 (3) (2019) 1–12.
[40] S. Jain, V. Yadav, D. Mishra, B. Kumar, Y. Deshmukh, N. Nigam, P. Khare, Utilizing Three Different Biochars for Attenuation of Toxic Acidic Mine Spoils Reflected by Lixiviate Quality Vis-a-Vis Phyto-Toxicity on Ocimum sanctum and Cassia angustifolia, Global J. Agricult. Innov., Res. Develop. 8 (2022) 49–65, https://doi.org/10.15377/2409-9813.2021.08.4.
[41] K.L. Sefatlhi, V.U. Ultra, S. Majoni, Chemical and Structural Characteristics of Biochars from Phytoremediation Biomass of *Cymbopogon Citratus*, *Cymbopogon Nardus*, and *Chrysopogon Zizanioides*, Waste Biomass Valor. 15 (2024) 283–300, https://doi.org/10.1007/s12649-023-02164-x.
[42] A. Saha, B.B. Basak, N.A. Gajbhiye, K.A. Kalariya, P. Manivel, Sustainable fertilization through co-application of biochar and chemical fertilizers improves yield, quality of Andrographis paniculata and soil health, Ind. Crop Prod. 140 (2019) 111607, https://doi.org/10.1016/j.indcrop.2019.111607.
[43] Z. Liu, Z. Wang, H. Chen, T. Cai, Z. Liu, Hydrochar and pyrochar for sorption of pollutants in wastewater and exhaust gas: A critical review, Environ. Pollut. 268 (2021) 115910, https://doi.org/10.1016/j.envpol.2020.115910.
[44] F.O. Omwoyo, G. Otieno, Optimization of Methylene Blue Dye Adsorption onto Coconut Husk Cellulose Using Response Surface Methodology: Adsorption Kinetics, Isotherms and Reusability Studies, J. Mater. Sci. Chem. Eng. 12 (2) (2024) 1–18, https://doi.org/10.4236/msce.2024.122001.
[45] F. Lu, C. Huang, L. You, J. Wanga, Q. Zhang, Magnetic hollow carbon microspheres as a reusable adsorbent for rhodamine B removal, RSC Adv. 7 (2017) 23255–23264, https://doi.org/10.1039/C7RA03045B.
[46] E.M. Rolim, E.M. Rolim, A.M.B. Silva, J.S. Batista, N.O. Serrão, L.O. Laier, F. Freitas, G.F. Perotti, D. Carmo, G.G. Celestino, Removal of rhodamine B and methylene blue using residual Onecarpus bacaba Mart fibers as biosorbent: kinetic and thermodynamic parameters, Discover Water. 4 (1) (2024) 13, https://doi.org/10.1007/s43832-024-00058-0.
[47] F. Dhaouadi, L. Sellaoui, L.E. Hernández-Hernández, A. Bonilla-Petriciolet, D. I. Mendoza-Castillo, H.E. Reynel-Avila, H.A. Gonzalez-Ponce, S. Taamalli, F. Louis, A.B. Lamine, Preparation of an avocado seed hydrochar and its application as heavy metal adsorbent: Properties and advanced statistical physics modeling, Chem. Eng. J. 419 (2021) 129472, https://doi.org/10.1016/j.cej.2021.129472.
[48] Z. Ding, L. Zhang, H. Mo, Y. Chen, X. Hu, Microwave-assisted catalytic hydrothermal carbonization of *Laminaria japonic*a for hydrochars catalyzed and activated by potassium compounds, Bioresour. Technol. 341 (2021) 125835, https://doi.org/10.1016/j.biortech.2021.125835.
[49] Z. Li, J. Liu, H. Han, Mechanical Properties and VOC Emission of Hemp Fibre Reinforced Polypropylene Composites: Natural Freezing-mechanical Treatment and Interface Modification, Fibers Polym. 22 (4) (2021) 1–13, https://doi.org/10.1007/s12221-021-00052-8.
[50] Y. Holade, C. Morais, K. Servat, T.W. Napporn, K.B. Kokoh, Enhancing the available specific surface area of carbon supports to boost the electroactivity of nanostructured Pt catalysts, Phys. Chem. Chem. Phys. 16 (2014) 25609–25620, https://doi.org/10.1039/c4cp03851g.
[51] Z.E. Brubaker, J.J. Langford, R.J. Kapsimalis, Quantitative analysis of Raman spectral parameters for carbon fibers: practical considerations and connection to mechanical properties, J. Mater. Sci. 56 (2021) 15087–15121, https://doi.org/10.1007/s10853-021-06225-1.
[52] A. Primo, M. Puche, O.D. Pavel, B. Cojocaru, A. Tirsoaga, V. Parvulescu, H. García, Graphene oxide as a metal-free catalyst for oxidation of primary amines to nitriles by hypochlorite, Chem. Commun. 52 (9) (2016) 1839–1842, https://doi.org/10.1039/c5cc09463a.
[53] Z. Lin, R. Wang, S. Tan, K. Zhang, Q. Yin, Z. Zhao, P. Gao, Nitrogen-doped hydrochar prepared by biomass and nitrogen-containing wastewater for dye adsorption: Effect of nitrogen source in wastewater on the adsorption performance of hydrochar, J. Environ. Manage. 334 (2023) 117503, https://doi.org/10.1016/j.jenvman.2023.117503.
[54] C.V. Kaline, G.A. Sabryna, B.F. Alice, F.A.M.O. Laís, J.S.F. Eduardo, B. B. Vanderson, L.P.S.Z. Carmem, L.S.D. José, M.T.M.O. Leonardo, Novel kapok pods (*Ceiba pentandra* (l.) Gaerth) adsorbent and its reusability by transformation on hydrochar with an outstanding adsorptive capacity for Rhodamine B removal, Sep. Purif. Technol. 326 (2023) 124787, https://doi.org/10.1016/j.seppur.2023.124787.
[55] G. Purwiandono, P. Lestari, Comparison of Two Biosorbent Beads for Methylene Blue Discoloration in Water, J. Ecol. Eng. 24 (8) (2023) 137–145, https://doi.org/10.12911/22998993/166319.
[56] F. Hashemzadeh, R. Rahimi, A. Ghaffarinejad, V. Jalalat, S. Safapour, Photocatalytic treatment of wastewater containing Rhodamine B dye via $Nb_2O_5$ nanoparticles: effect of operational key parameters, Desalin. Water Treat. 56 (1) (2014) 181–193, https://doi.org/10.1080/19443994.2014.936516.
[57] K. Kuśmierek, J. Fronczyk, A. Świątkowski, Adsorptive Removal of Rhodamine B Dye from Aqueous Solutions Using Mineral Materials as Low-Cost Adsorbents, Water Air Soil Pollut. 234 (2023) 531, https://doi.org/10.1007/s11270-023-06511-5.
[58] B. Wang, Y. Zhai, T. Wang, S. Li, C. Peng, Z. Wang, Fabrication of bean dreg-derived carbon with high adsorption for methylene blue: Effect of hydrothermal pretreatment and pyrolysis process, Bioresour. Technol. 274 (2019) 525–532, https://doi.org/10.1016/j.biortech.2018.12.022.
[59] P.C. Vithalani, N.S. Bhatt, Degradation of Rhodamine B, A Xanthene Dye by Aspergillus niger MSA2, Environ. Ecol. 40 (4A) (2022) 2258–2265.
[60] K.A. Babatunde, B.M. Negash, S.R. Jufar, T.Y. Ahmed, M.R. Mojid, 2022, Adsorption of gases on heterogeneous shale surfaces: A review. J. Petrol. Sci. Eng. 208, Part B, 109466. doi: 10.1016/j.petrol.2021.109466.
[61] A. Agoe, S.G. Poulopoulos, Y. Sarbassov, D. Shah, Investigation of Sewage Sludge–Derived Biochar for Enhanced Pollutant Adsorption: Effect of Particle Size and Alkali Treatment, Energies 17 (18) (2024) 4554, https://doi.org/10.3390/en17184554.
[62] M.S. Tehrani, R. Zare-Dorabei, Highly efficient simultaneous ultrasonic-assisted adsorption of methylene blue and rhodamine B onto metal organic framework MIL-68(Al): central composite design optimization, RSC Adv. 6 (2016) 27416–27425, https://doi.org/10.1039/C5RA28052D.
[63] Y. Tang, T. He, Y. Liu, B. Zhou, R. Yang, L. Zhu, Sorption behavior of methylene blue and rhodamine B mixed dyes onto chitosan graft poly (acrylic acid-co-2-acrylamide-2-methyl propane sulfonic acid) hydrogel, Adv. Polym. Tech. (2017) 1–11, https://doi.org/10.1002/adv.21932.
[64] M.T. Nakhjiri, G.B. Marandi, M. Kurdtabar, Adsorption of Methylene Blue, Brilliant Green and Rhodamine B from Aqueous Solution Using Collagen-g-p(AA-co-NVP)/$Fe_3O_4$@$SiO_2$ Nanocomposite Hydrogel, J. Polym. Environ. 27 (2019) 581–599, https://doi.org/10.1007/s10924-019-01372-8.
[65] X. Li, E. Bonjour, P. Jame, P. Kuzhir, C. Hurel, Production of hydrochar from biomass waste as economical adsorbents for methylene blue—insight of occurring adsorption phenomena, Biomass– Convers Biorefnery. 14 (2023) 19723–19737, https://doi.org/10.1007/s13399-023-04122-y.
[66] N. Chai, L. Gao, S. Li, Z. Ma, L. Li, M. Hu, Simple Alkali-Modifed Persimmon Peel–Montmorillonite Composite Hydrochar for Rapid and Effcient Removal of Methylene Blue, Sustainability. 15 (15) (2023) 11867, https://doi.org/10.3390/su151511867.
[67] A.K. Behera, K.P. Shadangi, P.K. Sarangi, Efficient removal of Rhodamine B dye using biochar as an adsorbent: Study the performance, kinetics, thermodynamics, adsorption isotherms and its reusability, Chemosphere 354 (2024) 141702, https://doi.org/10.1016/j.chemosphere.2024.141702.

Journal of Water Process Engineering 71 (2025) 107402

Contents lists available at ScienceDirect

Journal of Water Process Engineering

journal homepage: www.elsevier.com/locate/jwpe

# Synthesis of novel hydrochar from lemongrass distillation waste and its application in individual and simultaneous adsorption of a mixture of heavy metal ions

Thi Thao Truong [a], Truong Xuan Vuong [a], Thi Hong Huyen Chu [b], Thi Hong Tham Diep [a], Hoang Chinh Ta [a], Le Phuong Hoang [c], Tien Duc Pham [d,*]

[a] Faculty of Chemistry, TNU-University of Sciences, Thai Nguyen 250000, Viet Nam
[b] Faculty of Natural Resources and Environment, TNU-University of Sciences, Thai Nguyen 250000, Viet Nam
[c] Faculty of Civil and Environmental Engineering, Thai Nguyen University of Technology (TNUT), Tich Luong Ward, Thai Nguyen 250000, Viet Nam
[d] Faculty of Chemistry, University of Science, Vietnam National University Hanoi, 19 Le Thanh Tong, Hoan Kiem, Hanoi 100000, Viet Nam

ARTICLE INFO

Editor: Ludovic F. Dumée

*Keywords:*
Hydrochar
Lemongrass
Metal ions
Simultaneous adsorption

ABSTRACT

This study presents a new procedure to fabricate the lemongrass hydrochar (LH) and its applications for adsorptive removal of Cr(III), Ni(II), Zn(II), and Mn(II). Factors affecting the hydrothermal process including temperature, time and solid-liquid ratio were studied by XRD, EDS, FTIR, Raman, SEM, XPS and BET methods. The best hydrochar material demonstrated a high carbon content of 84.5 % by atomic (79.7 % by weight) and exhibited a porous morphology characterized by an average pore size, with a specific surface area of 32.66 $m^2/g$, the particle size of 1.5 × 5 μm and a point of zero charge ($pH_{pzc}$) of 5.4. The LH was a composite structure comprising amorphous carbon, cellulose, and graphene oxide, with the active functional groups such as C═O, O—H, C-O-C, and aromatic rings. The LH was effectively adsorbed Cr(III), Ni(II), Zn(II), and Mn(II) ions at pH 6, both independently and simultaneously, and was not significantly affected by the presence of other soluble cations. The adsorption efficiencies were in the order Zn < Mn < Ni < Cr at both 25 °C and 40 °C, which was mainly influenced by covalent indices and ionic charges. The individual adsorption of heavy metal ions on LH were well fitted with the Freundlich isotherm model and the multicomponent adsorption fitted well with the modified extended Sips isotherm model while both of them followed the Elovich kinetic model. Adsorption mechanism involved both chemical and physical interactions. Real samples were also tested with high removal efficiencies, indicating substantial applicability for heavy metal ions removal.

## 1. Introduction

Charcoal has long been recognized for its widespread historical use and its crucial role throughout human civilization. It has served as a biofuel, an amendment for soil improvement, and an environmentally sustainable remediation agent. Its high effectiveness and compatibility with the principles of green chemistry and sustainable development highlight its significance. Consequently, the exploration of charcoal-like materials derived from various biomass sources has garnered substantial attention, leading to the emergence of the term "hydrochar" around 2009–2011 [1]. Hydrochar is produced via hydrothermal processes, which offer the advantage of significantly reduced energy consumption compared to conventional pyrolysis, yielding biochar with distinct and unique properties. Recent years have witnessed a rapid increase in scientific researches focusing on hydrochar [2]. According to Huang et al., from January 1, 2011, to December 31, 2021, the Web of Science database cataloged 2403 publications on hydrochar, with a marked increase in output observed from 2017 to 2021 [1]. Notably, the two most frequently cited applications in this domain were "soil quality improvement" and "adsorption" within environmental science.

The raw materials utilized for hydrochar production could be classified into three primary categories as livestock wastes, municipal solid wastes, and agricultural feedstocks. Generally, livestock wastes possess low carbon content, which results in hydrochar characterized by low

* Corresponding author at: Faculty of Chemistry, University of Science, Vietnam National University Hanoi, 19 Le Thanh Tong, Hoan Kiem, Hanoi 100000, Viet Nam
*E-mail addresses:* tienducpham@hus.edu.vn, tienduchphn@gmail.com, ducpt@vnu.edu.vn (T.D. Pham).

https://doi.org/10.1016/j.jwpe.2025.107402
Received 28 October 2024; Received in revised form 24 February 2025; Accepted 2 March 2025
Available online 6 March 2025

porosity. Conversely, municipal solid wastes tend to exhibit complex compositions, leading to heterogeneous mechanisms of char formation and properties that are significantly influenced by both the composition of the raw materials and the production temperature. In contrast, agricultural feedstock, especially those derived from plants, represent the most accessible and cost-effective resources. These materials are typically porous, rich in carbon, and exhibit a high degree of compositional uniformity, thereby rendering them particularly advantageous for the production process and the subject of considerable research attention. The agricultural feedstock sources commonly studied include corn stalks, corn stover, corn cobs, rice husk, rice straw, wheat straw, bagasse, coconut husk, bamboo stems, etc., as well as various by-products from the leaves, seeds, peels, stems, roots, and flowers of different plant species [3,4]. Lemongrass is a common crop with substantial yield, originating from South and Southeast Asia, is widely cultivated in tropical regions. Lemongrass and its essential oil have numerous applications in herbal medicine, pharmaceuticals, cosmetics, food, and perfumery, and are particularly favored for their pleasant aroma and beneficial properties [5]. The global demand for lemongrass essential oil is significant, and the residual biomass from distillation represents a large by-product, commonly used as bedding material in livestock farming, a soil amendment, or for mushroom cultivation, and sometimes even discarded or landfilled. After distillation, lemongrass leaves primarily consist of fibrous, porous cellulose, which is highly advantageous for biochar production. Nonetheless, research on biochar production from lemongrass remains limited. Few published studies [6–9] have primarily focusing on pyrochar synthesis and its application in soil improvement. To the best of our knowledge, the investigation into the production of hydrochar from the distillation waste of lemongrass essential oil has not been reported.

In the field of environmental technology, hydrochar is primarily studied as an effective adsorbent for the removal of both inorganic and organic pollutants out of water and soil [10–12]. Hydrochar is highly values for its porous structure and the abundance of organic functional groups, which offer advantages over biochar. For heavy metal removal from water, initial studies predominantly focused on the adsorption of single metals such as Pb, As, Cr, Cd, and Cu. For instance, Cu(II) ions were removed by hydrochar derived from pinewood with higher efficiency than pyrochar from the same feedstock, despite pyrochar having a larger surface area, due to its increased oxygen-containing functional groups that facilitate ion-exchange adsorption [13]. Pb(II) was efficiently adsorbed by polyaminophosphonated-functionalized hydrochar derived from bamboo [14]. Hydrochar produced from *Eupatorium adenophorum* demonstrated the ability to adsorb Cd(II) through different interactions including electrostatic interaction, ion exchange, π – π interaction and complexation with organic functional groups [15]. Cr (III) has been studied for adsorption by pyrochar rather than hydrochar [16]. Research has also extended to simultaneous adsorption of two, three or four metal ions to solve actual wastewater treatment needs. For example, a mixture of Cd(II) and Pb(II) was successfully removed from solution using sulfide-modified hydrochar with magnetic pinecone primarily through electrostatic interactions, ion exchange, and complexation, achieving capacities of 62.49 mg/g for Cd(II) and 149.33 mg/g for Pb(II) [17]. Similar results were observed with hydrochars derived from rice husk and *Zizania latifolia* straw, which showed superior competitive adsorption of Pb compared to biochar [18]. The mixtures of Pb(II), Cd (II) and Cu(II) have also been simultaneously adsorbed using potassium permanganate-modified hydrochar from hickory wood, bamboo, and wheat straw [19], with the modified hydrochar from wheat straw achieving the highest adsorption efficiencies (189.24 mg/g for Pb(II), 29.06 mg/g for Cd(II), and 32.68 mg/g for Cu(II)), which is 12–17 times greater than raw hydrochar. Additionally, the simultaneous adsorption of cations Cu(II), Pb(II), Cd(II), and Zn(II) have been investigated using $H_2O_2$-modified hydrochar derived from peanut hulls in both batch and column tests, consistently showing higher adsorption of Pb(II) compared to other ions [20]. The simultaneous adsorption of Pb(II), Cr(VI), Cu(II), Cd(II), Zn(II), and Ni(II) has also been examined using hydrochars derived from the invasive plant *Alternanthera philoxeroides* (AP), with the MIL-53(Fe)-$NH_2$-magnetic hydrochar composite exhibiting the best adsorption capacity, following the order Pb(II) > Cr(VI) > Cu(II) > Cd (II) > Zn(II) > Ni(II) [21].

However, research on hydrochar remains limited compared to other materials such as pyrochar, activated carbon, zeolites, metal oxides and hydroxides. Current studies predominantly focus on a few ions, including Cu(II), Pb(II), Zn(II), Cd(II), and Cr(VI), while investigations on Ni(II), Mn(II), and Cr(III) are relatively scarce. These elements are frequently encountered in industrial wastewater, including chemical manufacturing, paper production, textiles, woodworking, and electroplating [22]. Such industries contribute significantly to global production and are widely distributed. When these metals release into aquatic media and accumulate in soil, they can be absorbed by plants through their roots. This infiltrating into the ecosystem disrupts food chains and may result in adverse effects on human health, as well as on the development of both flora and fauna.

This study aims to investigate the production process of hydrochar derived from lemongrass distillation residues, evaluate its efficacy as an adsorbent for both independent and simultaneous removal of Cr(III), Ni (II), Zn(II) and Mn(II) ions from aqueous solution. The adsorption mechanisms of Cr(III), Ni(II), Zn(II), and Mn(II) on hydrochar surface are also proposed based on interactions and the changes in surface charge and functional active surface groups after adsorption.

## 2. Materials and methods

### 2.1. Chemicals

The atomic spectroscopic standard solutions of 1000 mg/L Cr(III), Zn (II), Ni(II), and Mn(II) were delivered from Sigma-Aldrich. Double distilled water (DW), Hydrochlohydric (HCl, Isochem, 36–37 %), and sodium hydroxide (NaOH, Isochem, 98.5 %) were used. All chemicals are directly used without further purification. Distillation waste of lemongrass (DWL) was collected at the Institute of Life Sciences, Thai Nguyen University, Vietnam.

### 2.2. Synthesis of hydrochar

DWL was dried at 105 °C for 24 h, subsequently chopped, finely ground, and stored in a zip-lock bag. A specific mass (m) of DWL (m = 2, 4, 6, 8, 10 g) was completely dispersed in 50 mL of DW within a 100 mL Teflon container, which was then placed in a stainless steel autoclave. The autoclave was then heated to a specified temperature (T (Kelvin), where $T = 473$, 493 and 513 K) for varying durations (t hours, where $t =$ 3, 5, 10, 15 h) at a heating rate of 200 °C per hour. Following the heating process, the reactor was allowed to cool naturally to room temperature. The resulting material was filtered and washed with DW until the supernatant was colorless and washing water was neutral, then oven-dried at 378 K for 24 h, and designated as LHthmgT.

To activate the hydrochar, the synthesized material was immersed in 5 M KOH solution for 24 h at room temperature. Subsequently, the activated hydrochar was thoroughly washed with DW to achieve neutral pH and oven-dried at 378 K for 24 h, and was correspondingly designated as KLHthmgT. Based on the aforementioned conditions, optimal parameters for sample preparation were selected, and the material was utilized to investigate the individual and simultaneous adsorption of Cr (III), Zn(II), Ni(II), and Mn(II) cations.

Hydrochar production efficiency is calculated according to the eq. (1):

$$E_p = \frac{m_H}{m_{LDW}} x100\ (\%) \quad (1)$$

where $m_H$ and $m_{LDW}$ are the mass of hydrochar and initial DWL (g).

### 2.3. Characterization of the materials

X-ray diffraction patterns (XRD) were conducted utilizing a PAN-analytical X'Pert PRO MPD diffractometer, operating at 40 kV and 30 mA, with Cu-Kα radiation (λ = 0.15406 nm) over a 2θ range of 5° to 85°. Fourier-transform infrared (FTIR) spectra were obtained using a Perkin Elmer-400 spectrometer, analyzing pellets formed from a mixture of the sample and KBr (1:99 *w*/w) across the wavenumber range of 4000–400 $cm^{-1}$. The morphological features and elemental composition of the samples were assessed via scanning electron microscopy (SEM) integrated with an Energy-Dispersive X-ray System (EDS) at an acceleration voltage of 20 kV. Raman spectroscopy was performed at ambient temperature (25 °C) using a 532 nm argon laser as the excitation source (LabRAM HR Evolution, Horiba). The specific surface area ($S_{BET}$) and pore were determined using the Brunauer–Emmet–Teller (BET) method (TriStar 3000 V6.07), with the total pore volume (Vp) calculated at the maximum point of P/Po, and the average pore diameter estimated as $4Vp/S_{BET}$. The zeta potential (ζ) was measured using a Zetasizer Nano ZS (Malvern, England). Electrical properties were assessed through the point of zero charge ($pH_{PZC}$) [23]. Surface elemental composition and binding form of metal ions on hydrochar after adsorption were analyzed by X-ray photoelectron spectroscopy (XPS, Nexsa G2) using Al Kαradiation (1486.6 eV), calibrate with C 1 s assuming the binding energy of 284.8 eV.

### 2.4. Adsorption tests

Batch adsorption experiments of Cr(III), Zn(II), Ni(II), and Mn(II) were performed to evaluate the adsorption capacity of the prepared hydrochar for individual and simultaneous adsorption: 20 mg hydrochar was added to 10 mL of 20 mg/L of each ion solutions of single ion (Cr (III), Zn(II), Ni(II) and Mn(II)) at different initial pH (3,4,5,6) in a 15 mL Falcon. They were shaken for 4 h at 25 °C and 150 rpm. Heavy metal concentrations were determined using the ICP-OES technique. The solution pH values were measured after adsorption. The pH at which the best adsorption efficiency was observed ($pH_{optimal}$) was used in subsequent adsorption studies. Tn these studies, varying amount of hydrochar (adsorbent dosage = 0.5–1–2–5–10 g/L) was added to 10 mL of C mg/L/ ion solutions of single ions (Cr(III), Zn(II), Ni(II), and Mn(II)) (C = 5–10–20 –30 - 50 - 100–200-400–500-600 mg/L) or mixture of ions (C = 5–10–20-30-50–80 - 100–120-150 mg/L/ion) at $pH_{optimal}$ in a 15 mL Falcon was shaken for different contact time ($t$ = 10–30–60–90–129–180–240 min) at temperature of $T$ = 298 and 313 K, with a shaking speed of 150 rpm. After each test, the worked solutions were centrifuged and filtered to collect the transparent liquid The final heavy metal ion concentrations were quantified using ICP-OES (Hach DR 5000) at the wavelengths λ of 206.201 nm, 226.502 nm, 231.604 nm and 279.482 nm for Zn(II), Cr(III), Ni(II) and Mn(II), respectively.

The adsorption capacity, $q_t$ (mg/g or mmol/g) and adsorption efficiency $AE_t$ (%) at the time t (min) are calculated by eqs. (2) and (3):

$$q_t = (C_o - C_t)\frac{V}{m} \tag{2}$$

$$AE_t = \frac{(C_o - C_t)}{C_o}.100\% \tag{3}$$

where $C_o$ and $C_e$ are the initial and the concentration at time $t$ of each heavy metal ion (mg/L when prepared, converted to mmol/L (mM) when calculating), respectively, $V$ is the volume (L) and $m$ is the adsorbent mass (g).

For the single adsorption isotherms, the experimental data were fitted using Langmuir, Freundlich, Sips and Temkin models, based on the respective equations from (4) to (7) [24,25]:

$$q_e = q_m\frac{K_L C_e}{1 + K_L C_e} \tag{4}$$

$$q_e = K_F C_e^{n_F} \tag{5}$$

$$q_e = \frac{K_s C_e^{n_s}}{1 + b_s C_e^{n_s}} \qquad K_s = b_s.q_m \tag{6}$$

$$q_e = q_m.e^{\left(-K_{DR}\left(R^*T^*ln\left(1+{}^1/_{C_e}\right)\right)^2\right)} \tag{7}$$

where, $C_e$ is the equilibrium concentration of adsorbate (mM), $q_e$ and $q_m$ are the adsorption capacities at equilibrium and maximum adsorption, respectively; $K_L$ ($mM^{-1}$), $K_F$ ($mmol^{1-n_F}.L^{n_F}.g^{-1}$), $K_S$ ($mmol^{1-n_S}.L^{n_S}.g^{-1}$) and $K_T$ ($mM^{-1}$) are adsorption constants of Langmuir, Freundlich, Sips and Temkin isotherm models, respectively; $n_F$ and $n_S$ are Freundlich and Sips coefficient, respectively; and $b_S$ and B are Sips and Temkin parameter; $R$ is the universal gas constant (8.314 J/mol. K), T is the temperature in Kelvin (K).

The multi-component adsorption data were fitted using the extended Langmuir (EL), extended Freundlich (EF) and extended Sips (ES) isotherm models according to eqs. (8), (9) and (10) [26]:

$$q_{e,i}^M = \frac{q_{m,i}K_{L,i}C_{e,i}}{1 + \sum_{j=1}^{N} K_{L,i}C_{e,i}} \tag{8}$$

$$q_{e,i}^M = K_{F,i}C_{e,i}\left(\sum_{j=1}^{n} a_{ij}.C_{e,j}\right)^{n_i - 1} \tag{9}$$

$$q_{e,i}^M = \frac{K_{s,i}C_{e,i}^{n_{s,i}}}{1 + \sum_{j=1}^{N} b_{sj}C_{ej}^{n_{s,j}}} \tag{10}$$

where $q_{e,i}^M$ is the maximum adsorption capacity (mmol/g) obtained from multicomponent isotherm; $q_{m,i}$, $K_{L,i}$, $K_{F,i}$, $K_{S,i}$, $n_{F,i}$, $n_{S,i}$ and $b_{S,i}$ represent the maximum adsorption capacity (mmol/g), adsorption constants of Langmuir, Freundlich and Sips isotherm models, Freundlich and Sips coefficients, with Sips parameter of $i$ adsorbate obtained from the single component adsorption isotherm, respectively; N is number of adsorbates and $a_{ij}$ is the competitive coefficient between $i$ and $j$ adsorbates. For an approximate calculation, can be initially set to 1 and adjust later as necessary. Then for a set of $C_e$, values, the corresponding values of $q_{e,i}$ can be evaluated.

The experimental data were fitted to four kinetic models: the pseudo-first-order (PFO), pseudo-second-order (PSO), intra-particle diffusion (IPD) and Elovich kinetic models, performed according to the eqs. (11) to (14) [23]:

$$q_t = q_e\left(1 - e^{-k_1 t}\right) \tag{11}$$

$$q_t = \frac{k_2 q_e^2 t}{1 + k_2 q_e t} \tag{12}$$

$$q_t = k_{ID}t^{0.5} + c \tag{13}$$

$$q_t = \frac{1}{\beta}ln(v_o\beta t + 1) \tag{14}$$

where $k_1$ ($min^{-1}$), $k_2$ ($g.mM^{-1}.min^{-1}$) and $k_{ID}$ ($mM.g^{-1}.min^{-0.5}$) are the rate constants for the PFO, PSO and ID adsorption kinetic models, respectively; $c$ (mg/g) is the intercept of the ID model; $v_o$ is initial adsorption rate ($mM.g^{-1}.min^{-1}$) and $\beta$ is desorption constant during each experiment in Elovich equation.

The adsorption thermodynamic parameters, including apparent equilibrium constant $K_C$ (distribution coefficient), the Gibbs free energy variation (ΔG, kJ/mol) and the enthalpy variation (ΔH, kJ/mol), were calculated according to the eqs. (15), (16) and (17) [27]:

$$K_c = \frac{C_{e,A}}{C_e} \quad (15)$$

$$\Delta G = -RT\ln K_C \quad (16)$$

$$\ln\frac{K_{C,T_2}}{K_{C,T_1}} = \frac{\Delta H}{R}\left(\frac{1}{T_1} - \frac{1}{T_2}\right) \quad (17)$$

where R is the universal gas constant (8.314 J/mol K), $C_{eA}$ (mg/L) is the concentration of adsorbate on the adsorbent at equilibrium, and $C_e$ (mg/L) is the equilibrium concentration of adsorbate in the studied solution.

## 3. Results and discussion

### 3.1. Characterization of hydrochar from distillation waste of lemongrass

The hydrochar production yields are summarized in Table S1, with recovery efficiencies ranging from 32 % to 37 %. A negative correlation between temperature and yield was observed, likely attributable to enhanced carbonization at elevated temperatures that is similar to some other studies [28]. At lower temperatures, a smaller fraction of the feedstock underwent conversion to hydrochar, resulting in a greater proportion of untransformed material remaining in the final product. These yields were consistent following a 3 h hydrothermal treatment. Activated materials exhibited marginally lower yields compared to non-activated ones, potentially due to the KOH activation process further facilitating cellulose conversion, as well as cleaning and increasing the porosity. Furthermore, material loss during the post-activation washing process may have contributed to the reduction in yield. Notably, variations in hydrothermal treatment duration (ranging from 5 to 15 h) and feedstock solid-to-liquid ratios (4–10 g/50 mL) did not induce significant differences in hydrochar yield.

The XRD patterns of the materials are illustrated in Fig. 2(a). The XRD peaks of the DWL exhibit a diffraction peak at 2θ ≈ 10.1°, corresponding to the (001) plane of graphene oxide (GO), and a peak at 2θ ≈ 26.5° attributed to the (002) reflection planes of graphite [29]. Additionally, two diffraction peaks at 2θ ≈ 21.9° and 34.4° correspond to cellulose [30]. These results indicate that the distillation process results in incomplete removal of organic matter in lemongrass, with cellulose partially converted into GO and graphite forms.

When DWL is subjected to hydrothermal treatment at 473 K for 5 h (LH5g6h473), the characteristic peak at 2θ = 26.5° for graphite exhibits a significant decrease in intensity, while the peak at 2θ ≈ 21.9° for cellulose shifts to a higher 2θ value. This result suggests that hydrothermal treatment at 473 K does not significantly alter the structure of DWL. As the hydrothermal temperature increases to 493 K and 513 K (LH5g6h493 and LH5g6h513), there is a marked decrease in intensity and broadening of the characteristic peaks at 2θ = 21.9°, indicating that cellulose is transformed into an amorphous structure within the hydrochar, with optimal conversion occurring at 513 K. It is noteworthy that subsequent studies were conducted with hydrothermal temperature at 513 K. For simplicity, the hydrothermal temperature will not be included in the sample names (LHthmg).

Lemongrass hydrochar samples subjected to soaking in concentrated alkali for 24 h at room temperature (KLH) displayed significant changes in the XRD pattern. The peak at 2θ ≈ 10° in LH was split into two distinct peaks, shifting to 10.8° and 12.3° in KLH, while the peak at 2θ ≈ 20° was also split into two peaks at 20.2° and 21.5°, shifting to lower 2θ values as

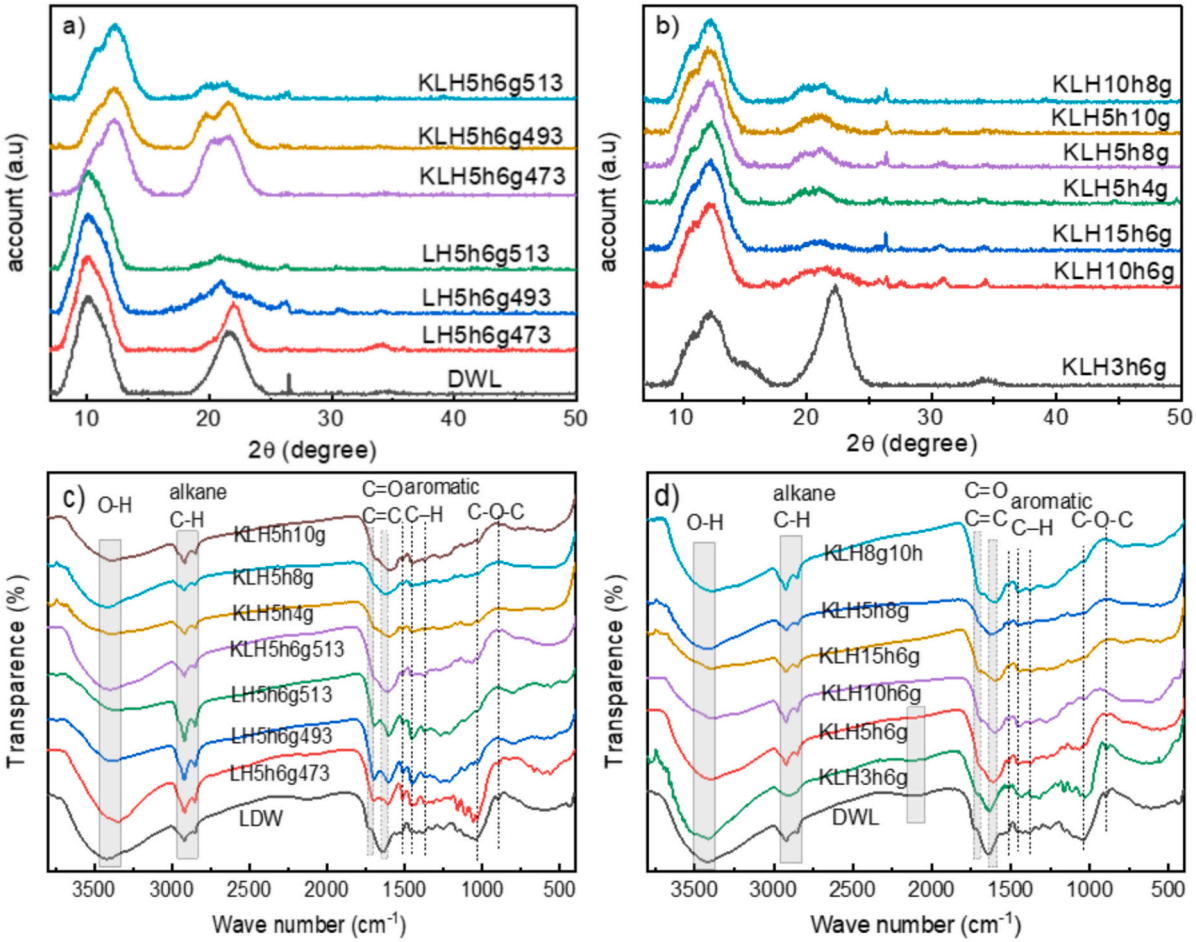


**Fig. 1.** The XRD patterns (a, b) and FTIR spectra (c, d) of DWL and prepared lemongrass hydrochars.

the temperature increased. The peak at 10.8° is attributed to the (001) plane of GO, while the peaks at 12.3°, 20°, and 21° correspond to the crystallographic plane reflections (1−10), (110), and (020), representing typical peaks of cellulose II polymorph [30,31].

During hydrothermal treatment across varying durations, Fig. 1b demonstrates that for the sample subjected to 3 h at 513 K, the peak observed in the XRD pattern at approximately 20° closely resembled that of both the DWL and the LH5h6g473 sample. This similarity suggests that, despite the high temperature, the short treatment duration was insufficient for the effective conversion of the initial lemongrass residue into char. As the duration of hydrothermal treatment is extended to 10 and 15 h at 513 K, a significant reduction in peak intensity and broadening in the 20° region was observed, indicating an enhanced degree of carbonization. However, when varying amounts of lemongrass residue (4 g, 6 g, 8 g, and 10 g in 50 mL of water) were treated for 5 h at 513 K, or when 8 g of residue was treated for 10 h at the same temperature, the XRD spectra did not display notable alterations. Therefore, it can be concluded that optimal hydrothermal conditions should be sustained for a minimum of 5 h at 513 K to achieve effective transformation.

The functional groups present in the DWL and hydrochar samples were analyzed using FTIR spectra, as shown in Fig. 1c and d. All samples exhibit certain similarities with a broad peak around 3350 $cm^{-1}$ assigned for the stretching vibration of hydroxyl (-OH) or carboxyl groups, while two peaks at 2909 and 2843 $cm^{-1}$ are attributed to the symmetric and asymmetric stretching vibrations of C—H bonds in aliphatic compounds [32], indicating that these bonds in the lemongrass residue remain intact after hydrothermal treatment. However, notable differences are observed between the FTIR spectra of DWL and the hydrochar samples: (1) A broad peak around 2220 $cm^{-1}$, attributed to the stretching vibration of -C ≡ C- or -C ≡ N bonds [33], is only observed in the FTIR spectra of LH473 and KLH3h samples. These specific groups suggest that when hydrothermal treatment occurs at a lower temperature (473 K) or for a shorter duration (3 h, even at 513 K), the -C ≡ C- or -C ≡ N bond is preserved. In contrast, this bond is completely decomposed when hydrothermal treatment exceeds 5 h or temperatures exceed 493 K. (2) The two peaks at 1735 $cm^{-1}$ and 1631 $cm^{-1}$ in DWL shift to 1698 $cm^{-1}$ and 1594 $cm^{-1}$ after hydrothermal treatment, with the extent of the shift increasing as the hydrothermal temperature and duration increase. When the mass of DWL is 6 g or 8 g, the shift remains consistent; however, as the mass decreases to 4 g or increases to 10 g, the shift of wavenumber continues to increase. These peaks correspond to the C═O stretching vibrations found in aldehydes, carboxylic acids, or esters derived from cellulose, and they also corresponded to the C═C stretching vibrations of lignin aromatic rings [34]. The observed peak shifts indicate that the breakdown of organic compounds in the feedstock results in greater exposure of aromatic compounds in the hydrochar samples. Notably, these peaks are sharp in un-activated hydrochar but appear as broad peaks in alkaline-activated hydrochar, suggesting that alkaline activation enhances the decomposition of lignin and cellulose [35]. (3) The peak in the wavenumber range of 1510–1363 $cm^{-1}$, associated with the stretching vibrations of C—C bonds in aromatic rings or in-plane bending vibrations of aromatic C—H groups [36], becomes more pronounced in the hydrochar samples. These changes indicate that aromatic rings are formed and/or recombined as a result of hydrothermal carbonization (HTC) treatment [37]. (4) The intensity of the peaks at 1025 $cm^{-1}$ and 898 $cm^{-1}$, could assign for the stretching vibrations of C—O groups in esters, phenols, and aliphatic alcohols, markedly decreases following HTC treatment, with a reduction observed as hydrothermal temperature and duration increase. This result suggests that the -C-O- bonds in DWL are decomposed during HTC treatment. Therefore, the bonding patterns and functional groups in DWL undergo significant changes following hydrothermal treatment, with these alterations being distinctly influenced by temperature, duration, and the quantity of DWL used in the process.

The microstructure and graphitic characteristics of carbon in the hydrochar were analyzed using Raman spectroscopy. A Gaussian function was employed to fit the peaks, to determine the position and intensity of the Raman peaks (Fig. 2). All samples exhibited the D band (approximately 1335 $cm^{-1}$), D″ band (approximately 1448 $cm^{-1}$), and G band (approximately 1572 $cm^{-1}$) with varying intensities and only minor differences in position. The D and G bands are typically associated with non-graphitic carbonaceous materials. Specifically, the D band corresponds to the vibrations of $sp^2$ carbon atoms at the edges of the graphene layers, indicating the degree of defects and the disordered nature of the graphitic lattice, which highlighting the presence of amorphous carbon structures. In contrast, the G band corresponds to the $E_2g$ mode of stretching vibrations of carbon atoms in an ideal graphitic lattice [37,38]. Both peaks signify the presence of carbon atoms ($sp^2$) within aromatic rings or condensed aromatic structures, indicating that the amorphous carbon is partially hydrogenated [39]. The broad peak of the D″ band at around 1448 $cm^{-1}$ corresponds to $CH_2$ bending, indicating that amorphous cellulose predominates over crystalline cellulose [40].

Table 1 shows that when increasing temperature from 473 K to 513 K, the hydrothermal time increased from 5 to 10 h, the solid/liquid ratio increased from 6 g/50 mL to 8 g/50 mL, the intensity of the D″ band decreased, the $I_D/I_G$ intensity ratio increased. These results suggest that the cellulose form decreased and the degree of disorder in the carbon material's microstructure increased. Thus, the KLH10h8g provided the most amorphous structure.

The surface morphology of hydrothermally treated lemongrass residue samples was analyzed by SEM images, as depicted in Fig. 3 and Fig. S1. With a consistent quantity of 6 g of DWL powder, hydrothermal treatment for 5 h at 473 K resulted in a heterogeneous surface texture (Fig. 3a). Certain regions exhibited blister-like formations, producing small pores, while the surface did not fully delaminate; instead, it developed nodular structures. In other areas, these nodules were completely disintegrated, leading to uniformly distributed holes resembling a honeycomb architecture. Increasing the hydrothermal temperature to 493 K (Fig. 3b) facilitated more uniform decomposition of the initial lemongrass powder, yielding a rough surface characterized by small scales. As it continued to increased to 513 K, the lemongrass powder were fragmented into porous layers and reduced in size (Fig. 3c). The hydrochar sample produced at 513 K for 5 h, followed by activation with an alkaline solution, exhibited a rough and coarse surface, with the porous layered structure transformed into smaller, granular particles composed of multiple thin layers (Fig. 3d). The increase in structural destruction and porosity of the starting materialobserved with higher hydrothermal temperatures and alkali activation are similar to some other research results [12,41]. For the lemongrass powder subjected to treatment at 513 K, if the hdrothermal duration was limited to 3 h (Fig. 3e), the initial surface experienced only minimal degradation, with low roughness and porosity. Extending the hydrothermal duration to 10 h (Fig. 3f)) led to further breakdown of the surface of the small porous granules formed after 5 h of hydrothermal treatment and subsequent activation. However, when the duration was extended to 15 h (Fig. 3g), despite the granules becoming even smaller, fine particles tended to block the porous openings, resulting in the agglomeration of the granules, which is similar to the results Gao et al. [42].

Upon subjecting varying amounts of lemongrass powder to hydrothermal treatment at 240 °C for 5 h, notable differences in the structural integrity of the powder were observed. Specifically, with 4 g of DWL powder (Fig. 3h), the initial structure fragmented into smaller, rougher aggregates, although the degree of decomposition was less pronounced than that observed in the 6 g sample. In contrast, the application of 8 g of DWL powder (Fig. 3i) resulted in a significant increase in fragmentation and porosity. However, when the DWL quantity was increased to 10 g (Fig. 3k), the level of decomposition decreased. This reduction in degradation may be attributed to the substantial volume of raw material at a 10 g/50 mL DW ratio, where the steam pressure generated was insufficient to effectively interact with the substrate. Conversely, at a 4 g/50 mL DW ratio, the powder exhibited dispersion more widely,

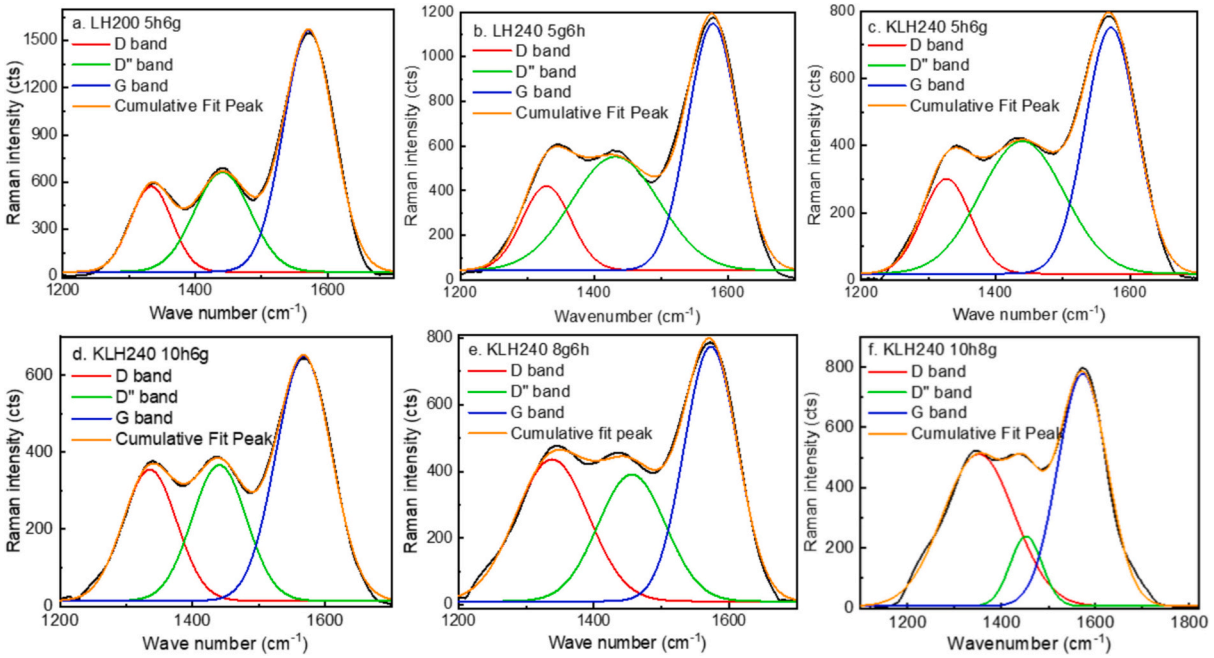


**Fig. 2.** Curve-fitting of Raman spectra of some lemongrass hydrochars.

**Table 1**
The intensity of Raman bands and the relative intensity ratio ($i_D/i_G$) of lemongrass hydrochars.

| | LH5h6g473 | LH5h6g513 | KLH5h6g | KLH10h6g | KLH5h8g | KLH10h8g |
|---|---|---|---|---|---|---|
| D band | 567.5 | 420.9 | 300.8 | 354.6 | 436.5 | 511.0 |
| D″ band | 666.5 | 552.5 | 413.4 | 366.6 | 392.4 | 241.2 |
| G band | 1560.2 | 1147.2 | 751.4 | 643.3 | 771.0 | 776.5 |
| $I_D/i_G$ | 0.36 | 0.37 | 0.40 | 0.55 | 0.57 | 0.66 |

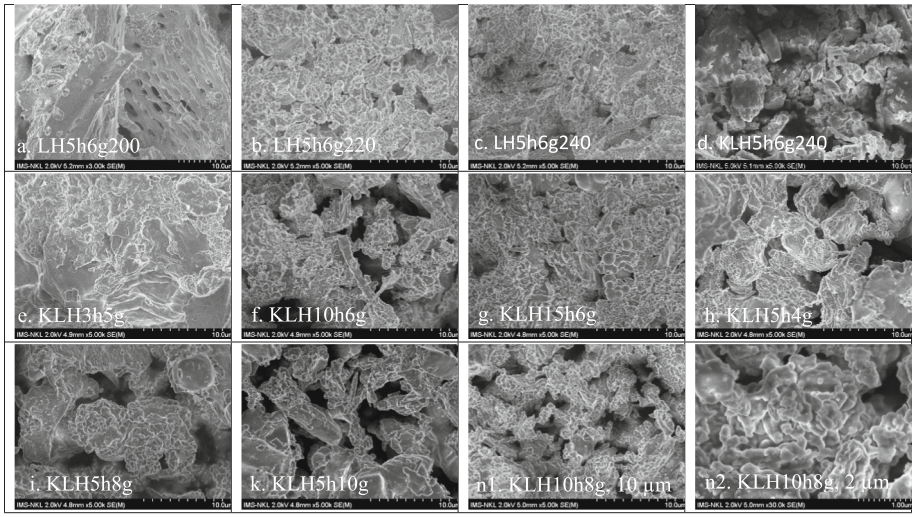


**Fig. 3.** SEM images of lemongrass hydrochar samples.

resulting in a diminished effective pressure applied to the material. For the 8 g DWL treated in 50 mL of DW at 240 °C for 10 h (Fig. 3n1 and 3n2), the powder underwent relatively uniform decomposition, resulting in a material with small size, approximately 1.5 × 5 µm, and highly porous dimensions.

The elemental compositions determined from the EDS spectra presented in Fig. 4a and Table S2 reveal a significant change in carbon content across the samples. In the DWL sample, the carbon content is approximately 62 %, accompanied by trace amounts of Na, Mg, Si, K, and Ca. With an increase in temperature from 473 K to 513 K, the carbon content rose from 70.80 % to 74.43 % and 76.93 %, respectively, and further increased to 78.01 % after activation. Thus, hydrothermal treatment and activation enhanced the carbon content compared to the raw materials. As hydrothermal time increased from 3 h to 6 h, and 10 h followed by activation, the carbon content increased from 65.59 % to 78,01 and 81.85 %, but slightly decreased to 75.12 % when the duration

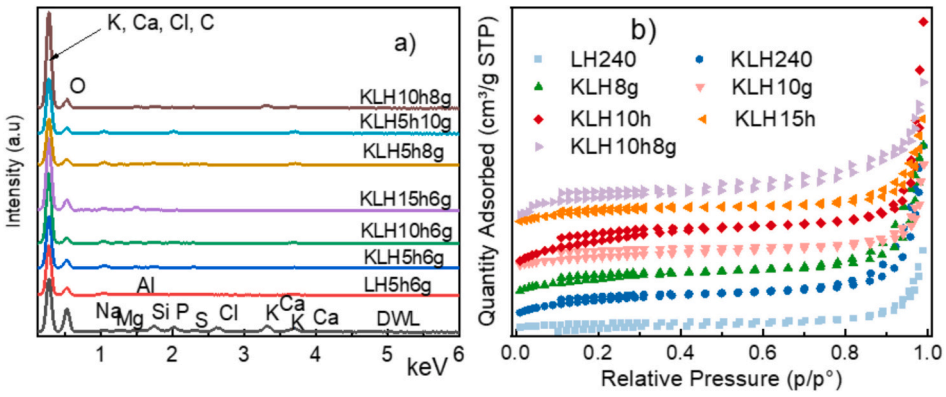


**Fig. 4.** EDS spectra (a) and nitrogen adsorption-desorption isotherm (BET method) of hydrochar materials.

was extended to 15 h. Similarly, when the DWL/DW ratio in the sample increased from 4 g/50 mL to 6 g/50 mL and 8 g/50 mL, the carbon content increased from 76.57 % to 78.01 % and 79.14 %, while a further increase to 10 g/50 mL resulted in a decline to 77.82 %. Considering both the hydrothermal duration and the DWL/DW ratio, hydrothermal treatment with 8 g of DWL in 50 mL of DW at 240 °C for 10 h, followed by alkaline activation, resulting in a carbon content of 84.45 %. This indicates that the degree of carbonization is dependent on temperature, hydrothermal duration, and the solid-to-liquid ratio of the feedstock, as well as whether activation is applied. Lower hydrothermal temperatures and shorter durations corresponded with lower carbonization levels; indeed, the resultant products still retained the brownish color of the initial material. In contrast, the hydrochar obtained after hydrothermal treatment at 513 K for 5 h or longer exhibited a fine black appearance. The carbon content of the prepared hydrochar in our study is significantly higher than that of previous ones [28,43].

The specific surface area ($S_{BET}$), porosity, and pore size of the synthesized hydrochar were quantified using the BET method, with results depicted in Fig. 4b. The $S_{BET}$ was in range of 5.81 to 32.66 $m^2/g$, increasing with rising of hydrothermal temperature, duration, and DWL/DW ratio reflecting similar trends observed in the carbon content of the sample under hydrothermal conditions. Integrating these findings, the material obtained from hydrothermal treatment of 8 g of lemongrass powder in 50 mL of DW at 513 K for 10 h, followed by activation, exhibited a substantial increase in specific surface area to 32.66 $m^2/g$. These results align with those from XRD, Raman spectroscopy and SEM analyses, indicating that increasing temperature, extending hydrothermal duration to specific thresholds, and adjusting the DWL/DW ratio collectively enhanced carbonization, increased porosity, and reduced material size. Nevertheless, prolonged hydrothermal duration or an excessive DWL/DW ratio may diminish the porosity of the final product. In comparison to several other studies (Table 2), hydrochar typically exhibited relatively small specific surface areas [44–47]. However, when activated at high temperatures [45] or $FeCl_3$ [48], they could have significantly larger specific surface areas. Notably, when activated using similar methods, the products obtained in this study demonstrated significantly higher specific surface areas.

Consequently, the optimal conditions for producing hydrochar from DWL via hydrothermal methods were established as a mixture of 8 g of powder in 50 mL of DW, treated in a 100 mL reactor at 240 °C for 10 h.

### 3.2. Adsorption study

#### 3.2.1. Influence of solution pH and absorbent dosage

Based on the *E*-pH diagrams of various elements in water under standard conditions, the solutions with pH values of 3, 4, 5, and 6 was selected to investigate the adsorption of 20 mg/L Cr(III), Zn(II), Ni(II), and Mn(II) ions using 2 g/L of KLH10h8g material under the duration of 3 h. The results are presented in Fig. 5a.

Fig. 5a demonstrates that at pH 3, the adsorption capacity of

**Table 2**
Comparison of porous structure properties of hydrochar with other studies.

| No. | Hydrochar (resources) | Synthesis | $S_{BET}$ ($m^2/g$) | Average Pore Size (nm) | Pore volume $cm^3/g$ | Adsorption application | Reference |
|---|---|---|---|---|---|---|---|
| 1 | Corncob | 4.0 g corncob (+4.0 g $NH_4Cl$) / 60 mL solution, | 14.45 | | 0.17 | Cu(II) and Cr(VI) | [44] |
| 2 | N-doped hydrochar | stirred for 1 h, hydrothermal at 220 °C 24 h | 42.45 | | 0.41 | | |
| 3 | Avermectin residue | Hydrothermal at 180 °C 2 h with an electromagnetic stirring speed of 400 r/min, | 7.22 | 15.3 | 0.05 | Cd(II) and Cu(II) | [45] |
| | | activate by $KHCO_3$ at 600–800 K | 110–310 | 1.91–3.91 | 0.09–0.36 | | |
| 4 | Alga-based hydrochars | 2.00 g powders / 40 mL DW (contains 2 mmol of KCl, $KH_2PO_4$, $K_2CO_3$, and KOH), stirred overnight, then hydrothermal by microwave at 200 °C for 1.5 h | 1.67 to 15.7 | 12.1 to 16.1 | | Pb(II) | [46] |
| 5 | Avocado seed hydrochar | 1.5 g biomass./ 1 mL water, hydrothermal at 523 K for 12 h | 40.54 | 1.163 | 0.013 | Ni(II), Pb(II), Cu (II) | [47] |
| 6 | Rice straw | biomass (was mixed with 1.2 % $FeCl_3$ solution or not), hydrothermal at 200 °C for 3 h | 39.9–44.3 | | | Pb(II), Cu(II) | [48] |
| 7 | Distillation waste of lemongrass essential oil | LH5h6g240 | 5.81 | 26.3 | | | **This study** |
| | | KLH5h6g240 | 14.91 | 22.2 | | Cr(III), Ni(II), Zn (II), Mn(II) | |
| | | KLH10h6g | 24.63 | 20.3 | | | |
| | | KLH15h6g | 11.77 | 18.9 | | | |
| | | KLH5h8g | 18.30 | 17.6 | | | |
| | | KLH5h10g | 9.46 | 19.6 | | | |
| | | KLH10h8g | 32.66 | 8.6 | | | |

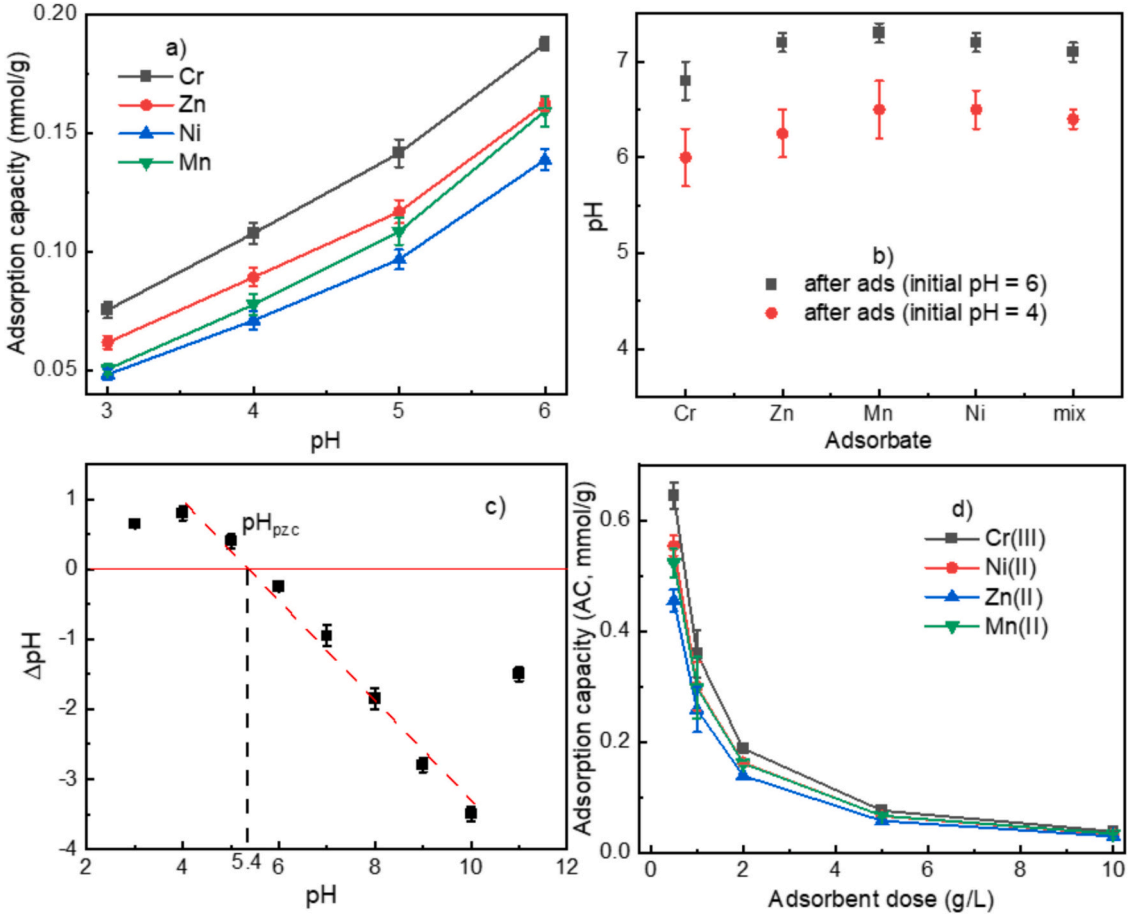


**Fig. 5.** Adsorption capacity at different pH values (a), pH before and after adsorption (b), the $pH_{pzc}$ of KLH10h8g (c) and individual adsorption capacity (Cr(III), Zn (II), Ni(II) or Mn(II) at $C_o$ = 20 mg/L/ion) at different KLH10h8g adsorbent dosage (d) at room temperature.

KLH10h8g material for the heavy metal ions was markedly low. As the pH increased, the adsorption capacity progressively rose, with a more pronounced increase occurring between pH 5 and 6. This phenomenon can be attributed to the high concentration of $H^+$ ions in low pH. This results in strong competitive adsorption with metal ions, as the high mobility of $H^+$ tends to dominate the adsorption process. In addition, at low pH, less negative charge of hydrochar surface prevent the attraction to the heavy metal cations. This assertion is corroborated by the pH measurements of the solution post-adsorption. When the initial pH was 4, the solution pH after adsorption was approximately 6.5, while for an initial pH of 6, the pH increased to 6.8 to 7.3, indicating a significant reduction in the proton concentration in the solution after adsorption, suggesting that protons were adsorbed onto the material. Notably, the pH of the solution after the adsorption of Cr(III) was the lowest, and Cr (III) adsorption consistently exhibited the highest efficiency across all initial pH levels, indicating that Cr(III) competes most effectively with $H^+$. Conversely, the pH of the solution after the adsorption of Mn(II) and Zn(II) was the highest, indicating that this solution has absorbed the greatest amount of $H^+$, which corresponds to the consistently low adsorption efficiency of Mn(II) and Zn(II) at various pH levels [27].

Furthermore, based on the experimentally determined $pH_{pzc}$ (Fig. 5b), which was 5.4, it implies that at pH values below 5.4, the material surface carried a positive charge, aligning with the studied ions, thus resulting in repulsive interactions that diminish the adsorption capacity of metal cations onto the carbon surface. At pH 6, the surface became negatively charged, and the $H^+$ concentrations in the solution was negligible, facilitating the adsorption of metal cations, thereby increasing both the efficiency and capacity of adsorption. At higher pH levels, the adsorption of cations such as Zn(II), Ni(II), and Mn(II) may continue to increase but Cr(III) undergoes hydroxylation; therefore, experiments were not conducted at elevated pH levels. pH 6 was also selected for subsequent studies on both single-ion and mixed-ion adsorption.

The influence of adsorbent dosage on the independent adsorption capacities of each ion was investigated under conditions of 20 mg/L for each cation at pH 6 over 4 h with varying concentrations of KLH10h8g. Fig. 5d shows that, as adsorbent dosage increased, the adsorption capacity progressively enhanced, as the increase in the amount of adsorbent enlarged the surface area, thereby increasing the number of available adsorption sites. At a dosage of 2.0 g/L, the adsorption efficiency was high, approaching saturation; further increases in carbon concentration yield diminishing returns in efficiency. This concentration will be utilized in the study of adsorption kinetics and relevant adsorption theories.

### 3.2.2. *Adsorption isotherms of Cr(III), Zn(II), Ni(II), and Mn(II) on lemongrass hydrochar*

The individual adsorption experimental data (with different initial sorbate concentrations) were fitted with the nonlinear form of the Langmuir, Freundlich, Sips and Temkin isotherm models. The results are presented in Fig. 6 and Table 3.

Fig. 6 and Table 3 show that the adsorption capacity increased with an increase of the initial concentration of the four ions. The alignment of the experimental data for single-ion adsorption with various isotherm models, as indicated by the $R^2$ values, differed in the following order: Temkin < Langmuir < Freundlich ≅ Sips. Although the $R^2$ in the Langmuir model reached from 0.918 to 0.954, significantly lower than 0.99 in the Freundlich and Sips models, but the values of $q_{m,cal}$ error

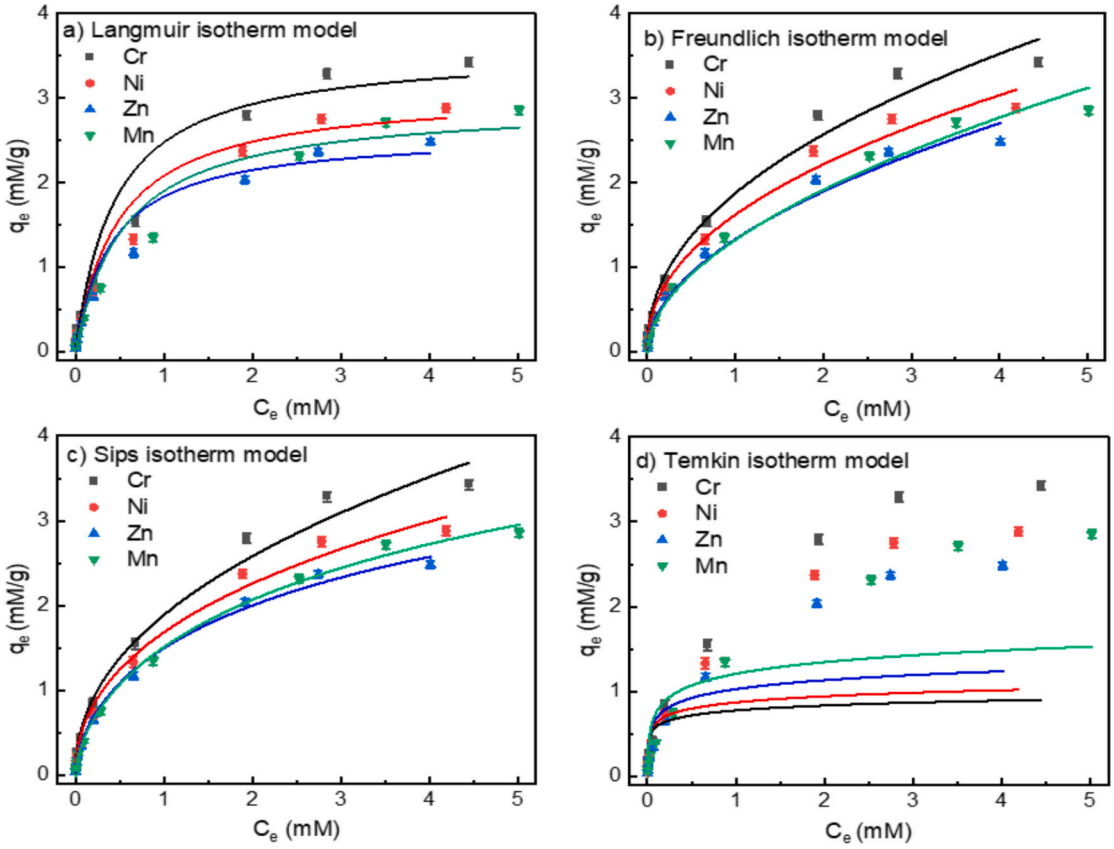


**Fig. 6.** Effect of the initial concentration of adsorbates and adsorption isotherm of individual adsorption of Cr(III), Zn(II) Ni(II) and Mn(II) on KLH10h8g fitted by different isotherm models.

**Table 3**
Parameters of different adsorption isotherm models of individual adsorption of Cr(III), Zn(II) Ni(II) and Mn(II) on KLH10h8g.

| Model | Parameter | Cr(III) | Ni(II) | Zn(II) | Mn(II) |
|---|---|---|---|---|---|
| | $q_{m,\ exp}$ (mmol/g) | 3.43 | 2.88 | 2.48 | 2.86 |
| Langmuir | $K_L$ ($mM^{-1}$) | 2.24 | 2.08 | 2.42 | 1.83 |
| | $q_{m,cal}$ (mmol/g) | 3.59 | 3.08 | 2.59 | 2.94 |
| | Error of $q_m$ (%) | 4.67 | 6.77 | 4.60 | 2.83 |
| | $R^2$ | 0.922 | 0.918 | 0.954 | 0.946 |
| Freundlich | $n_F$ | 0.456 | 0.453 | 0.512 | 0.533 |
| | $K_F$ ($mmol^{1-n_F}.L^{n_F}.g^{-1}$) | 1.87 | 1.62 | 1.33 | 1.32 |
| | $R^2$ | 0.987 | 0.993 | 0.992 | 0.992 |
| Sips | $q_{m,cal}$ (mmol/g) | 87.77 | 16.87 | 5.82 | 6.76 |
| | Magnitude of $q_{m,cal}$ compared to $q_{m,exp}$ | 25.63 | 5.85 | 2.35 | 2.36 |
| | $K_s$ ($mmol^{1-n_s}.L^{n_s}.g^{-1}$) | 1.93 | 1.87 | 2.01 | 1.94 |
| | $b_s$ $(mmol/L)^{-n_s}$ | 0.02 | 0.11 | 0.35 | 0.29 |
| | $n_s$ | 0.462 | 0.479 | 0.598 | 0.616 |
| | $R^2$ | 0.988 | 0.994 | 0.998 | 0.998 |
| Temkin | B (mmol/g) | 0.08 | 0.10 | 0.15 | 0.20 |
| | $K_T$ ($mM^{-1}$) | 10,341.14 | 4447.43 | 901.25 | 439.76 |
| | $R^2$ | 0.369 | 0.456 | 0.629 | 0.678 |

were quite small compared to $q_{m,exp}$, was 2.83 to 6.77 %. The Sips model exhibited the highest regression coefficient ($R^2$), but is not significantly higher than $R^2$ in the Freundich model. Furthermore, all the values of $q_{m,\ cal}$ were calculated by the Sips equation much higher than $q_{e,\ exp}$, 2.35 to 25.63 times larger. It suggests that the Sips model is inappropriate point. Thus, the Freundlich model shows the best fit to the experimental data, as well as having a certain fit according to the Langmuir model. This finding suggests that the KLH10h8g surface was heterogeneous with different positions having varying adsorption abilities and chemical interaction with the adsorbate ions, after that, the adsorbate ions continue to be physically adsorbed upward, forming multilayers during adsorption. The *n* values, ranging from 0.453 to 0.616, indicated that the adsorption process was favorable. [24,25].

The adsorption capacities of the ions followed the order Zn(II) < Mn (II) < Ni(II) < Cr(III), consistent with increasing $K_F$, which represented the adsorption capacity of each ion. In contrast, the Freundlich and Sips exponent ($n_F$ and $n_S$) relativity decreased along this sequence, underscoring both the surface heterogeneity of the adsorbent and the energetic variability of adsorption sites [49]. The adsorption capacity being influenced by several additional factors, including ionic hydration radius, electronegativity, affinity, ion charge, as well as indices such as the covalent index ($\chi_m^2 r$), ionic index ($Z^2/r$), and cationic polarizing power. S.S. Zamil et al. [50] determined that the covalent index accounted for 69 % of the variability in $q_{max}$ values. Similarly, a study by F. Batoo et al. [51] highlighted that the adsorption capacity of 13 metal ions by the *Aerva javanica* absorbent was predominantly influenced by the covalent index and polarizability being the secondary factor. Consequently, higher covalent index values correlated with greater adsorption capacity for heavy metal ions. In the present study, for divalent cations, the maximum adsorption capacities were found to increase in the order Zn(II) < Mn(II) < Ni(II), reflecting a corresponding rise in the covalent index (from 2.015, 1.994 and 2.517, respectively) and ionic index (5.40, 5.97 and 5.79, respectively) [52]. The covalent index of Cr(III) (2.2) is smaller than Ni(II), the cationic polarizing power values of Cr(III) showing a markedly higher value (7.9) shown a markedly higher value compared with those of Mn(II), Zn(II), Ni(II) (2.91, 3.7 and 4.2, respectively), due to its significantly greater ionic charge. At

pH = 6, Cr(III) exists as soluble $Cr(OH)^{2+}$ cation, so the charge is reduced but the OH group can form the hydrogen bonds with hydrochar surface, increasing adsorption capacity. Thus, when considering the combined effects of the sorbate's characteristics, the adsorption capacity decreased in the order: Cr(III) > Ni(II) > Mn(II) > Zn(II). These results agreed well with the previously published studies [53–56]. The adsorption capacities in our case are higher than some other materials for multicomponent system of heavy metal cations, such as Jordanian bentonite, which adsorbed Zn(II), Pb(II), Cr(III) and Mn(II) from water [53]; a composite of dendrimer/titania adsorbed Cu(II), Ni(II) and Cr (III) [54], the super porous polyethyleneimine cryogels, which adsorbed Cd(II), Co(II), Cr(III), Ni(II), Pb(II), and Zn(II) from contaminated waters [55]; or the Polyamide Resin adsorbed Ni (II), Cd (II), and Zn (II) Ions [56].

The simultaneous adsorption experimental data at different initial adsorbate concentrations were fitted to the EL, EF and ES isotherm models. The results of plotting the $q_{e,cal}$ against $q_{e,exp}$ are shown in Fig. 7.

It is observed that, the significant differences between $q_{e,exp}$ and $q_{e,cal}$ values were calculated by multicomponent isotherm models. This is because the approximate calculation used the parameter values ($K$, $n$, $q_m$) of the single ion adsorption model in the context of the simultaneous adsorption, where the presence of other ions leads to competitive adsorption and interactions between them, and approximate $a_{ij}$ in the Freundlich model, causing these parameters to change. To correct this difference, some authors have proposed the coefficient $P_i$, a correction factor for adsorbate i, in EL isotherm model [26,57], which is given by the modified extended Langmuir (MEL) isotherm equation as follows:

$$q_{e,i}^{MEL} = \frac{1}{P_{L,i}} \frac{q_{m,i} K_{L,i} C_{e,i}}{1 + \sum_{j=1}^{N} K_{L,i} C_{e,i}} = \frac{1}{P_{L,i}} q_{e,i}^{EL} \tag{18}$$

We also use the coefficient $P_i$ as a correction factor for adsorbent i in the modeling of the modified EF (MEF) and modified ES (MES) models:

$$q_{e,i}^{MEF} = \frac{1}{P_{F,i}} K_{F,i} C_{e,i} \left( \sum_{j=1}^{n} C_{e,j} \right)^{n_i - 1} = \frac{1}{P_{F,i}} q_{e,i}^{EF} \tag{19}$$

$$q_{e,i}^{MES} = \frac{1}{P_{S,i}} \frac{K_{s,i} C_{e,i}^{n_{s,i}}}{1 + \sum_{j=1}^{N} b_{sj} C_{ej}^{n_{sj}}} = \frac{1}{P_{S,i}} q_{e,i}^{ES} \tag{20}$$

$P_i$ was is determined by fitting the relationship between $q_{e,cal}$ and $q_{e,exp}$ according to the linear relationship $q_{e,cal} = a^* q_{e,exp}$ using origin software to minimum the error. Then, the degree of suitable between experimental results and calculated results from modified isotherm models was evaluated based on the following criteria such as: the root mean square error (RSME, measures the mean difference between the $q_{e,cal}$ and $q_{e,exp}$ or the standard deviation of the model error) [26]) and the chi-square ($\chi^2$) [24]:

$$\mathrm{RMSE} = \sqrt{\sum_{i=1}^{N} \frac{\left( q_{e,i,exp} - q_{e,i,cal} \right)^2}{N}} \tag{21}$$

$$\chi^2 = \sum_{i=1}^{N} \frac{\left| q_{e,i,exp} - q_{e,i,cal} \right|^2}{q_{e,i,exp}} \tag{22}$$

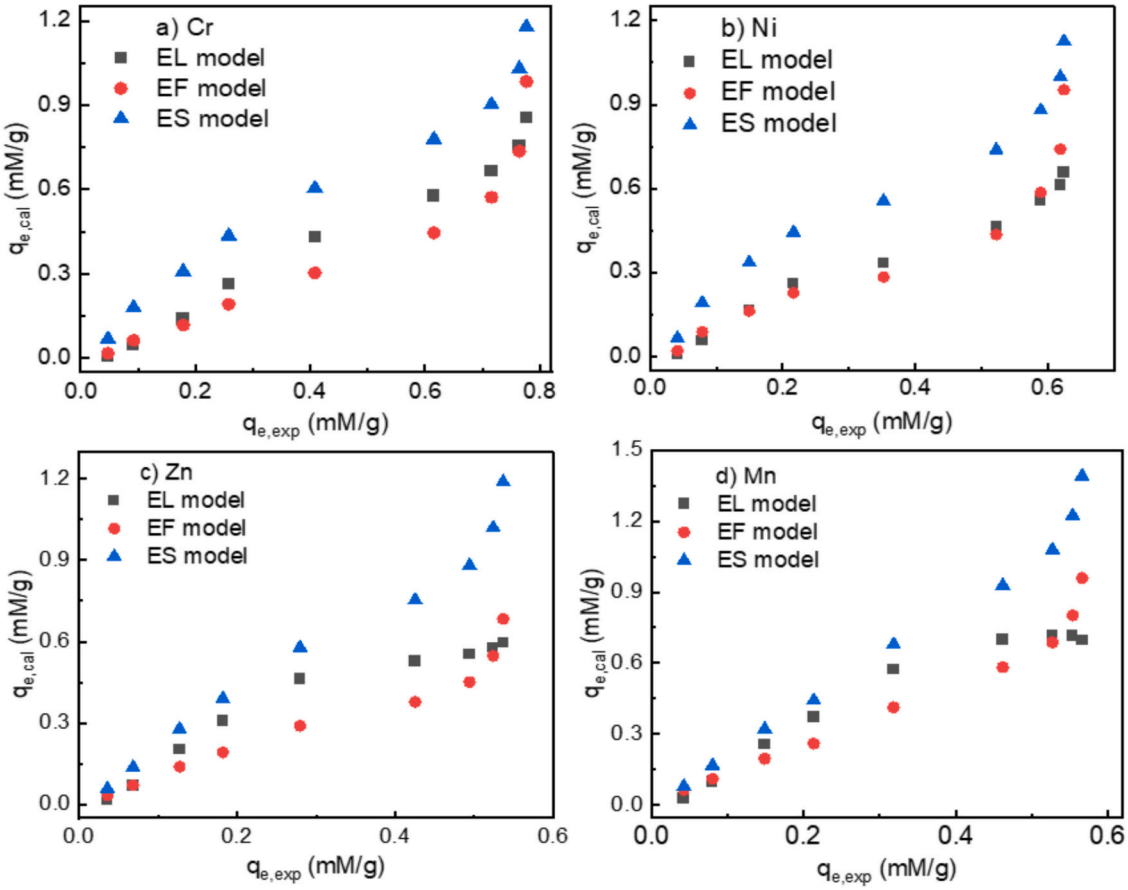


**Fig. 7.** The graph representing $q_{e,cal}$ according to multicomponent isotherm models versus $q_{e,exp}$ simultaneous adsorption of a) Cr(III); b) Ni(II); c) Zn(II) and d) Mn (II) on KLH10h8g at differential initial concentrations.

Where $N$ is the number of measurement points. The smaller the values of RMSE and $\chi^2$, the better the fit of the tested model is ensured. These results are presenting on the Table 4.

The findings from the simultaneous adsorption study of four heavy metal ions in a solution with equivalent mass concentrations differ from those observed in the individual adsorption of each ion. For the adsorption of Cr(II) and Ni(II) ions, the values of RMSE follow the order MEL<MES < MEF but the values of $\chi^2$ follow the order MES < MEL<MEF, in which, the RMSE for MES model was not much higher than by MEL (0.047 compared with 0.042 and 0.047 compared with 0.033, compared to 0.115 and 0.096 to the MEF model. It indicates that, the experimental data fit poorly to the MEF model, better to the MEL model, and best to the MES model. For Zn(II), the smallest $\chi^2$ value for MES model (0.032 compared to 0.049 and 0.052) and the smallest RMSE value for the MEF model (0.66 compared to 0.789 for the MES model and 2.149 for the MEL model). For Mn(II), both the RMSE and $\chi^2$ values are smallest for the MES model. Thus, in general, the MES isotherm model demonstrated the best fit, with the lowest RMSE and $\chi^2$ values for all four ions. These results indicate that the MES model best described the simultaneous adsorption process The $q_{e,\ exp}$ values for each ion followed the same trend observed in individual adsorption, increasing in the order Zn(II) < Mn(II) < Ni(II) < Cr(III), with slight variations in magnitude. It means that, the adsorption capacity of these ions which are in the same solution is also affected by the covalent index, the ionic index and the cationic polarizing power as in individual adsorption. Furthermore, in a multi-ion adsorption system, the presence of different ions will lead to posible inter-ionic interactions, leading to adsorption capacity being influenced. These capabilities are evaluated based on the ratio of the adsorption capacity of each ion in the multi-component adsorption scenario ($q_{max,\ m}$) to that of single ion adsorption ($q_{max,\ s}$) at the same of initial concentration [58]. If $q_{max,\ m}/\ q_{max,\ s} > 1$, it means the adsorption process enhanced by the presence of other metal ions; if $q_{max,\ m}/\ q_{max,\ s} = 1$, the adsorbed metal ions are not affected by other ions; and if $q_{max,\ m}/\ q_{max,\ s} < 1$, the adsorption process is suppressed by the presence of other metal ions. The $q_{max,\ m}/q_{max,\ s}$ ratios were calculated and listed in Table 5.

Table 5 demonstrates that the ratio of $q_{max,\ m}/q_{max,\ s}$, for Cr(III), Zn (II), Ni(II), and Mn (II) onto 2 g/L KLH10h8g at varying initial concentrations (pH 6, 240 min, 298 K) was <1, with the exception of Cr (III) at an initial concentration of 5 mg/L. This finding indicates that the presence of competing ions results in competitive adsorption, thereby diminishing the $q_{max,\ m}$ values in comparison to $q_{max,\ s}$. The ratio exhibited a decreasing trend as the total ion concentration in the solution increased, with the reduction following the order: Cr(III) < Ni(II) < Zn(II) < Mn(II). This suggests that Cr(III) encountered the least competition, with a reduction of 1.5 % to 6.5 %, while Mn(II) experienced the most pronounced competition, with a reduction ranging from 2.6 % to 15.1 %. Although these reductions were relatively minor, the overall adsorption capacity for ions in the mixed solution remained within the limits of single ion adsorption capacities at equivalent initial concentrations.

The competitive adsorption among ions is predominantly influenced by the intrinsic properties of each ion. Factors such as hydrodynamic radius, electronegativity, charge, covalent index, ionic index, and cationic polarizing power play a critical role, as previously discussed.

**Table 5**
The $q_{max,\ m}/q_{max,\ s}$ ratios of Cr(III), Zn(II), Ni(II) and Mn(II) onto 2 g/L KLH10h8g at different initial concentrations (pH 6, 240 min, 298 K).

| $C_o$ (mg/L) | $q_{max,\ m}/\ q_{max,\ s}$ | | | |
|---|---|---|---|---|
| | Cr | Ni | Zn | Mn |
| 5 | 1.0037 | 0.9975 | 0.9752 | 0.9735 |
| 10 | 0.9847 | 0.9576 | 0.9368 | 0.9256 |
| 20 | 0.9645 | 0.9227 | 0.8878 | 0.8758 |
| 30 | 0.9346 | 0.8995 | 0.8568 | 0.8492 |
| 50 | 0.9219 | 0.8852 | 0.7966 | 0.7730 |
| 100 | 0.7854 | 0.7497 | 0.7095 | 0.6347 |

Moreover, the competitive ability may also be modulated by the standard reduction potential of the respective ions, with a higher reduction potential correlating with a greater affinity for the adsorbent. The ionization reduction potentials for Ni(II), Zn(II), and Mn (II) were − 0.26 *V*, −0.76 V, and − 1.17 V, respectively. Consequently, the competitive capacity increases in the order of Ni(II) to Zn(II) to Mn(II). For Cr (III) ion, due to the partial hydrolyzed, the competition can be influenced by a combination of all factors mentioned above and the form of Cr $(OH)^{2+}$. A similar trend has been documented in the literature [53,56,59].

### 3.2.3. Adsorption kinetic and thermodynamic study

Individual adsorption with different initial concentrations of adsorbates over a designated time period were conducted, analyzed and fitted by some kinetic models, as depicted in Figs. 8, Fig. S2 and detailed in Table 6.

Fig. 8 shows that the adsorption of Ni(II) and Cr(III) occurred rapidly, with approximately 75 % of the initial concentration reaching within just 10 min, and then reached to about 99 % after 240 min. In contrast, the adsorption of Zn(II) and Mn(II) ions was considerably slower, attaining merely 13–28 % of the initial concentration after 10 min, though it later accelerated, achieving around 95–96 % after 240 min. Consequently, the unique characteristics of each ion significantly impacted both the rate and capacity of adsorption.

Kinetic analyses of the adsorption process, evaluated through various theoretical models, indicated that the fit to diffusion kinetic models was the weakest. This finding suggests that the adsorption of metal ions on the adsorbent surface was primarily constrained by the interaction between the adsorbent and the adsorbate. This interaction was more accurately represented by a range of kinetic models: at an initial concentration of 20 mg/L/ion, the adsorption of Mn(II) aligned well with all three models: the PFO model ($R^2 = 0.996$), the PSO model ($R^2 = 0.994$), and the Elovich model ($R^2 = 0.985$). The adsorption of Zi(II) indicated a good fit with both the PSO and Elovich models ($R^2 = 0.982$), while the adsorption of Cr(III) and Ni(II) showed the best fit with the Elovich model. The predominance of fit with the PSO and Elovich models indicated that the interactions involved were predominantly chemical in nature, with a heterogeneous adsorbent surface [23].

Moreover, increasing the initial concentration of metal ions to 100 mg/L for each ion (Fig. S2) significantly enhanced the fit of the experimental data to the theoretical models. Although the ID kinetic model still showed the poorest fit, $R^2$ values ranged from 0.867 to 0.955. Both the PFO and PSO kinetic models achieved values exceeding 0.99 (0.992–0.997 for the PSO model and 0.994–0.999 for the PFO model),

**Table 4**
The correction factors for adsorbent *i* and error analysis in modified simultaneous adsorption isotherm models (MEL, MEF and MES).

| Model | MEL | | | MEF | | | MES | | |
|---|---|---|---|---|---|---|---|---|---|
| Parameter | $P_i$ | RMSE | $\chi^2$ | $P_i$ | RMSE | $\chi^2$ | $P_i$ | RMSE | $\chi^2$ |
| Cr(III) | 0.997 | 0.042 | 1.893 | 0.939 | 0.115 | 2.356 | 1.384 | 0.047 | 1.276 |
| Ni(II) | 0.980 | 0.033 | 1.730 | 1.134 | 0.096 | 1.793 | 1.623 | 0.047 | 1.524 |
| Zn(II) | 1.193 | 0.052 | 2.149 | 1.050 | 0.049 | 0.660 | 1.970 | 0.032 | 0.789 |
| Mn(II) | 1.389 | 0.049 | 1.680 | 1.425 | 0.045 | 0.810 | 2.190 | 0.029 | 0.570 |

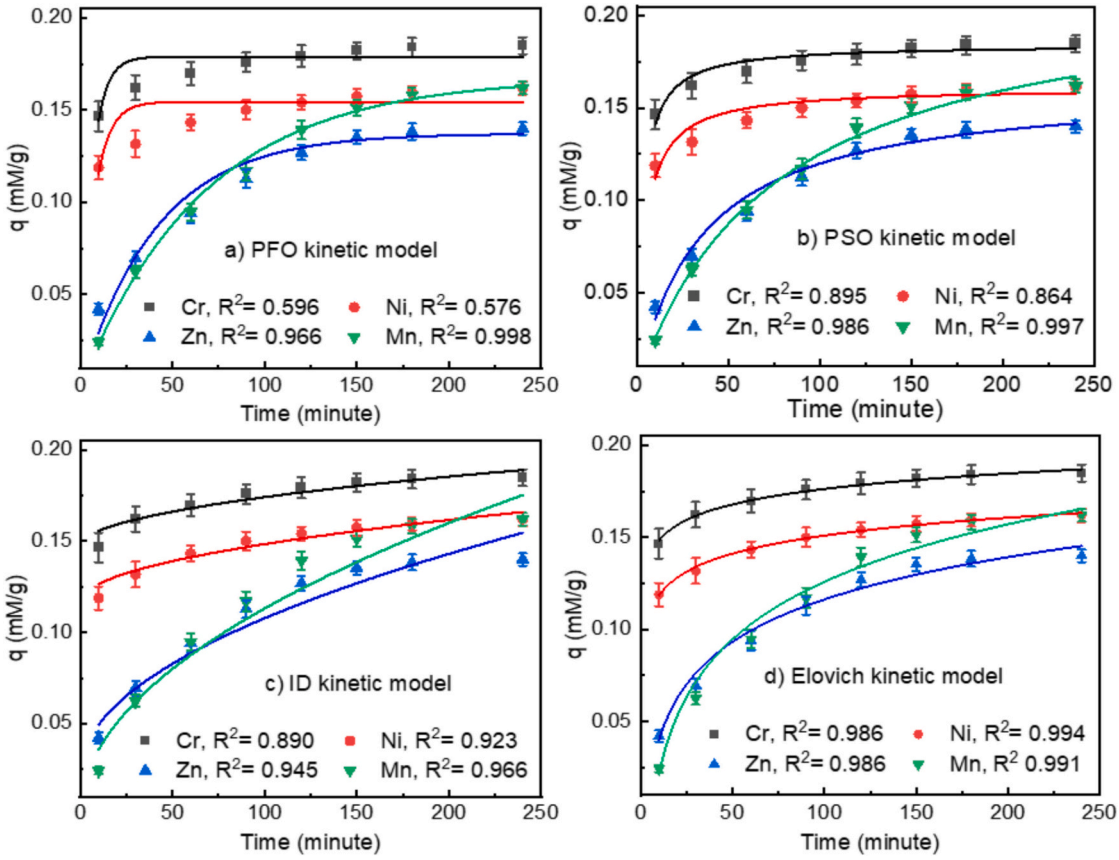


**Fig. 8.** Effect of initial concentration of adsorbates and adsorption kinetic models of individual adsorption of 20 mg/L/ion Cr(III), Zn(II) Ni(II) and Mn(II) on 2 g/L KLH10h8g.

surpassing the Elovich model, which achieved $R^2$ values between 0.985 and 0.991. This suggests that the initial concentrations significantly influenced the kinetics of the process; as initial concentration increases, the likelihood of physical interactions also rises. This can be attributed to the increased density of ions and a substantial reduction in inter-ionic distance, thus enhancing the effects of physical interactions. As a result, the fit for the PFO model shows a marked increase, while the inherent chemical interactions maintain the fit for the PSO and Elovich kinetic models.

Simultaneous adsorption experiments were performed and analyzed using the nonlinear forms of some kinetic models, as detailed in Figs. 9, S3, S4 and Table 6.

The simultaneous presence of four cations in the solution, each at a concentration of 5 mg/L (equal to 0.075 to 0.095 mM/L, which is reduced 4 times to a single ion solution of 20 mg/L/ion), led to alterations in the adsorption dynamics of each ion over time, as compared to individual ion adsorption. After 10 min shaking, the adsorption efficiencies for Cr(III), Ni(II), Zn(II) and Mn(II) reached 72.71 %, 66.60 %, 64.16 %, and 58.87 %, respectively. These values slightly decreased for Cr(III) and Ni(II) but strongly increased for Zn(II) and Mn(II) compared to single adsorption. After 240 min, the adsorption efficiencies for Cr (III), Ni(II), and Zn(II) reached 99.20 %, 98.68 %, and 96.33 %, respectively, showing only marginal enhancements compared to single ion adsorption. Nevertheless, the adsorption efficiency for Mn(II) decreased to 93.73 %. While the order of adsorption capacities among the metal ions remains consistent with that observed during single ion adsorption, the adsorption capacities for each ion shifted in the context of simultaneous adsorption, demonstrating an increase in short-term adsorption efficiency.

As the initial concentration of each ion increased to 10 mg/L/ion and subsequently to 25 mg/L/ion (Fig. S3 and S4), the correlation between the experimental data and the theoretical models improved, paralleling observations from individual ion adsorption studies. At an initial concentration of 10 mg/L/ion within the mixed solution, the $R^2$ values for the Elovich model remained the strongest correlation, significantly surpassing those of the alternative models. In contrast, when the initial concentration in the mixed solution escalated to 25 mg/L/ion, the $R^2$ values for the ID model still was the lowest, though it improved to a range of 0.916 to 0.969. The $R^2$ values for the remaining three models were closely clustered, nearing unity: the Elovich model exhibited values between 0.989 and 0.995, the PFO model ranged from 0.987 to 0.999, and the PSO model achieved the highest values, ranging from 0.997 to 0.999. These findings are consistent with those from single ion adsorption; as the concentration of ions in the solution rose, the spatial distance among ions and between the ions and the adsorbent diminishes, fostering stronger interactions both among the ions and with the adsorbent surface. Consequently, the kinetics of adsorption are altered compared to scenarios characterized with lower ion concentrations, with physical interactions between the sorbate and adsorbent becoming increasingly significant.

The influence of temperature on adsorption kinetics was undertaken, analyzed and fitted to the nonlinear form of the Elovich kinetic model. The results are illustrated in Fig. 10 and detailed in Table 6.

Fig. 10 illustrates that the adsorption kinetics over time during both individual and simultaneous adsorption at 313 K were similar to those at 298 K, aligning most closely with the Elovich kinetic model. However, a slight decreased in adsorption capacities was obtained, as detailed in Table 6.

To further investigate the mechanism underlying the adsorption process, the quantity $R_E$, ($R_E = 1/(q_{ref}k_E)$), which serves as the approaching equilibrium factor, was calculated using the Elovich equation. Here, $q_{ref}$ represents the amount of adsorption at time $t = t_{ref}$

**Table 6**
Kinetic and thermodynamic parameters for the adsorption of Cr(III), Ni(II), Zn(II) and Mn(II) onto KLH10h8g.

| Adsorbate | Kinetic parameters | Individual adsorption | | | Simultaneous adsorption | | | |
|---|---|---|---|---|---|---|---|---|
| | | 20 mg/L/ion 298 K | 20 mg/L/ion 313 K | 100 mg/L/ion 298 K | 5 mg/L/ion 298 K | 5 mg/L/ion 313 K | 10 mg/L/ion 298 K | 25 mg/L/ion 298 K |
| Cr (III) | $q_{e,exp}$ ($10^2$mM/g) | 18.48 | 18.39 | 84.08 | 4.72 | 4.55 | 9.19 | 21.77 |
| | $v_o$(mM.g$^{-1}$.min$^{-1}$) | 247.29 | 84.06 | $3.91.10^{-2}$ | 1.72 | $7.97.10^{-2}$ | 0.31 | $1.41.10^{-2}$ |
| | $R_E$ | 0.087 | 0.124 | 0.247 | 0.066 | 0.071 | 0.013 | 0.279 |
| | $K_C$ | 129.13 | 21.89 | 10.83 | 34.26 | 28.92 | 28.23 | 7.63 |
| | ΔG (kJ/mol) | −12.04 | −8.03 | −5.90 | −8.76 | −8.76 | −8.28 | −5.03 |
| | ΔH (kJ/mol) | −91.7466 | | | −8.7500 | | | |
| Ni (II) | $q_{e,exp}$ ($10^2$mM/g) | 16.19 | 15.98 | 72.85 | 4.12 | 3.94 | 7.86 | 18.25 |
| | $v_o$ (mM.g$^{-1}$.min$^{-1}$) | 6.28 | 3.15 | $3.14.10^{-2}$ | 0.20 | $5.59.10^{-2}$ | $5.79.10^{-2}$ | $8.88.10^{-3}$ |
| | $R_E$ | 0.108 | 0.126 | 0.272 | 0.087 | 0.093 | 0.063 | 0.279 |
| | $K_C$ | 86.90 | 17.39 | 7.02 | 33.12 | 22.73 | 16.93 | 6.90 |
| | ΔG (kJ/mol) | −11.06 | −7.43 | −4.83 | −8.67 | −8.13 | −7.01 | −4.79 |
| | ΔH (kJ/mol) | −83.19 | | | −19.46 | | | |
| Zn (II) | $q_{e,exp}$ ($10^2$mM/g) | 14.00 | 13.83 | 64.68 | 3.59 | 3.43 | 6.83 | 15.51 |
| | $v_o$ (mM.g$^{-1}$.min$^{-1}$) | $1.10.10^{-2}$ | $1.11.10^{-2}$ | $2.50.10^{-2}$ | 0.15 | $3.52.10^{-2}$ | $1.83.10^{-2}$ | $6.32.10^{-3}$ |
| | $R_E$ | 0.112 | 0.132 | 0.283 | 0.237 | 0.231 | 0.187 | 0.282 |
| | $K_C$ | 26.25 | 11.74 | 4.99 | 15.67 | 13.06 | 11.12 | 6.63 |
| | ΔG (kJ/mol) | −8.10 | −6.41 | −3.98 | −6.82 | −6.69 | −5.97 | −4.68 |
| | ΔH (kJ/mol) | −41.61 | | | −9.44 | | | |
| Mn (II) | $q_{e,exp}$ ($10^2$mM/g) | 16.19 | 16.09 | 75.25 | 4.24 | 3.87 | 8.02 | 18.15 |
| | $v_o$ (mM.g$^{-1}$.min$^{-1}$) | $7.35.10^{-3}$ | $7.66.10^{-2}$ | $2.76.10^{-2}$ | $5.54.10^{-2}$ | $3.28.10^{-2}$ | $1.44.10^{-2}$ | $6.42.10^{-3}$ |
| | $R_E$ | 0.130 | 0.137 | 0.295 | 0.278 | 0.266 | 0.288 | 0.285 |
| | $K_C$ | 14.94 | 5.97 | 4.08 | 8.61 | 8.08 | 7.86 | 4.97 |
| | ΔG (kJ/mol) | −6.70 | −4.65 | −3.49 | −5.33 | −5.44 | −5.11 | −3.97 |
| | ΔH (kJ/mol) | −47.46 | | | −3.24 | | | |
| $\Sigma q_{e,\ exp}$ | | 0.138–0.185 | | 0.65÷0.84 | 0.17 0.16 | | 0.32 | 0.74 |

(mg/g), where $t_{ref}$ denotes the longest duration of the adsorption process (min), and $k_e$ is the Elovich constant (g/mg). The calculated results indicate that the $R_E$ values fall within zone III ($R_E = 0.02$ to 0.1) only in the single ion adsorption of Cr(III) and Ni(II) at an initial concentration of 20 mg/L. Similarly, $R_E$ values in the adsorption of Cr(III) from a mixed solution at 5 mg/L/ion also fall in this range, suggesting a rapidly rising adsorption curve was. In contrast, the remaining cases show $R_E$ values within zone II ($R_E = 0.1$ to 0.3), or zone IV, where the adsorption curve rises more gently [60]. This behavior aligns with the characteristics of chemical adsorption as described by the Elovich equation.

Table 6 indicates that the total adsorption capacities for ions from the mixed solution containing four ions falls within the range of the individual adsorption capacities of each ion at the same initial total concentrations (20 mg/L or 100 mg/L). This result demonstrates a high potential for simultaneous ion adsorption.

In terms of the thermodynamics of the adsorption process, the values of ΔG were consistently negative, indicating that the process was spontaneous and thermodynamically favorable. Regarding energy, the ΔH values for the single ion adsorption processes were <20 kJ, suggesting that these processes were predominantly characterized by physical adsorption. However, in the simultaneous adsorption of the four cations, the ΔH values were all negative (exothermic processes) and >40 kJ, indicating that chemical adsorption was the primary mechanism. This result suggests that the interactions among the simultaneously present ions lead to mutual effects, altering their interactions with both the adsorbent surface and the sorbates.

### 3.2.4. Adsorption mechanisms

The findings from the adsorption isotherm model studies indicate that the single adsorption processes adhere to the Freundlich isotherm model and multicomponent adsorption fitted well to the modified extended Sips isotherm model. This suggests that the interactions between the sorbates and the adsorbent surface are primarily physical. Furthermore, kinetic adsorption investigations and thermodynamics studies demonstrated that increasing the initial concentration of sorbates supports the chemical adsorption characteristics of the process. Additionally, the solution pH after both single and multi-ion adsorption increased, indicating that $H^+$ ions were adsorbed concurrently with the studied cations. This observation suggests that the interactions are governed by electrostatic attraction, a form of physical interaction. In fact, at pH 6, Cr(III) ion was partially hydrolyzed to form $CrOH^{2+}$ or completely hydrolyzed to $Cr(OH)_3$, which is difficult to verify. However, if Cr(III) ion is completely hydrolyzed, $Cr(OH)_3$ will not be adsorbed but only deposited on the material surface, without affecting the surface charge or spectrum signal. These conclusions were validated through the measurement of the XPS spectra (Fig. 11), the ζ potential and FTIR spectra (Fig. 12) of the KLH10h8g sample before and after adsorption.

The survey spectra (the black line in Fig. 11a) shows that: the KLH10h8g surface mainly contains carbon (~284.7 eV) and oxygen (~532 eV), small amount of nitrogen (~399 eV) and absence of heavy metal elements. The blue line and red line in Fig. 11a indicate the presence of heavy metal ion on KLH10h8g after adsorption, they are clearly shown in Fig. 11d,e,f,g. In Fig. 11d, the peak at 587.9 eV corresponding to Cr $2p_{1/2}$ confirms the appearance of $Cr^{3+}$, in addition, a peak at 577.5 eV of Cr $2p_{3/2}$ demonstrates that, a partial Cr(III) was oxidation to Cr(VI) adsorbed on the KLH10h8g surface [61]. In Fig. 11e, peak of $Ni^{3+}$ $2p_{3/2}$ at 856 eV and $Ni^{2+}$ $2p_{1/2}$ at 873.5 eV confirms the adsorption of Ni, outside that, two satellite peak of Ni can be observed at 863 eV and 880 eV. Fig. 11f shows two peak at 1044 eV and 1022 eV corresponding to $Zn^{2+}$ $2p_{1/2}$ and $Zn^{2+}$ $2p_{3/2}$. Mn 2p spectrum on KLH10h8g can be deconvoluted into $Mn^{2+}$ $2p_{1/2}$ at 652 eV and a broad peak at 641–642 eV, may be an overlap of $Mn^{2+}$ $2p_{3/2}$ and $Mn^{3+}$ $2p_{3/2}$,

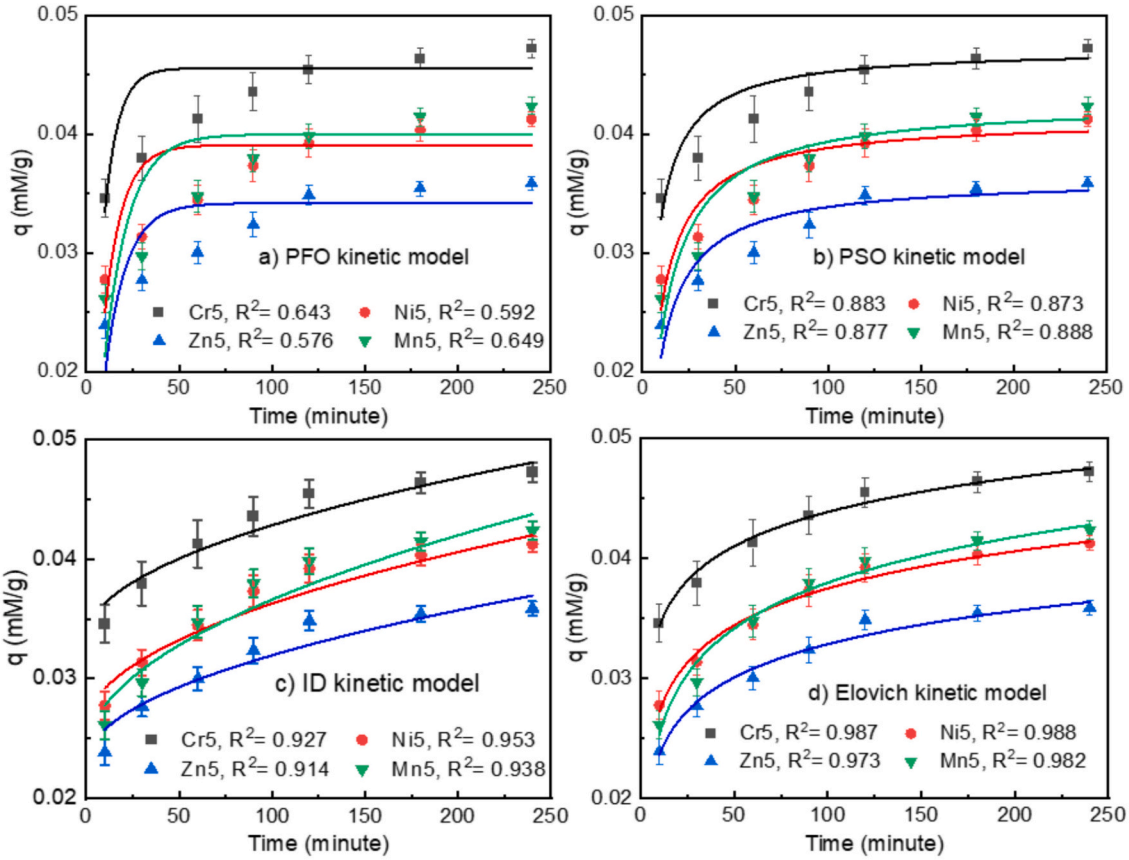


**Fig. 9.** Effect of initial concentration of adsorbates and adsorption kinetic models of simultaneous adsorption of 5 mg/L/ion Cr(III), Zn(II) Ni(II) and Mn(II) on 2 g/L KLH10h8g.

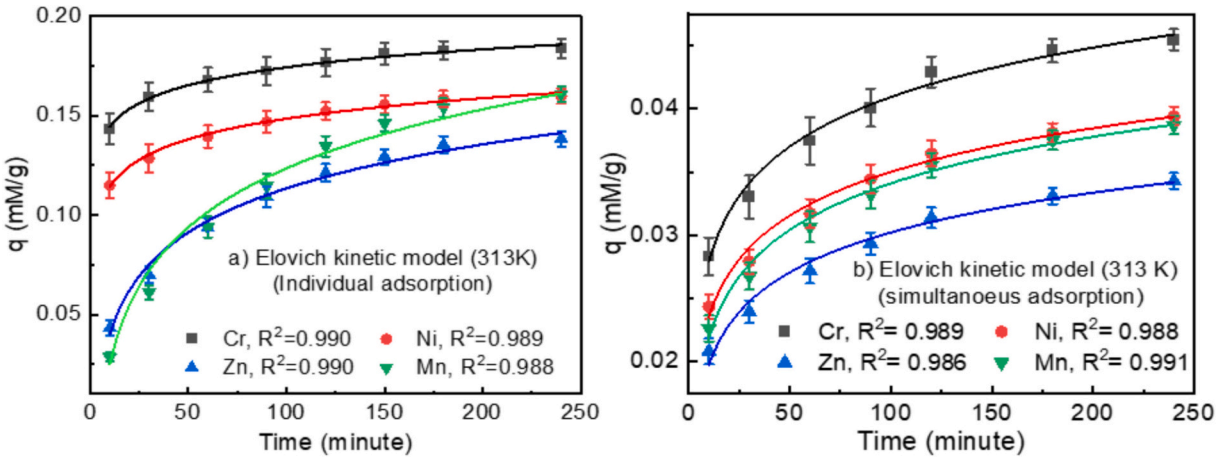


**Fig. 10.** The individual adsorption of 20 mg/L/ion and the simultaneous adsorption of 5 mg/L/ion by 2 g/L KLH10h8g at pH 5, 313 K via time and fitted to Elovich kinetic model.

(Fig. 11g). [62]. Thus, except for a fairly stable ion of Zn(II), during the adsorption process, Cr(III), Ni(II) and Mn(II) ions were partially oxidized to a higher oxygen number and are adsorbed onto the sample surface. XPS Analysis of oxygen (Fig. 11b) and carbon (Fig. 11c), by fitting the peaks by Gaussian function, show that, position and intensity of the characteristic peaks corresponding to their different bond forms in the sample after adsorption all shift slightly compared to before adsorption. For example, O in C═O bond from 530.8 eV shifted to 531.3 eV; O in O═C-O bond at 533.9 eV disappear after adsorption of Cr or mixture; C in C═C, C—O and C═C bond were reduced intensity and shifted position [63,64]. After adsorption, a small peak characteristic of the C-Me bond also appeared at 283 eV after adsorption Cr(III) or mixture of ions [65]. All results show that, interaction between heavy metal ions with hydrochar was a partial chemical interaction.

Fig. 12a reveals that the ζ potential of the adsorbent surface before adsorption was −24.89 mV, indicating a negatively charged surface at pH 6 (consistent with the determined $pH_{pzc}$). This value increased to −18.88 mV after adsorption of Cr(III) ion and to −6.92 mV following

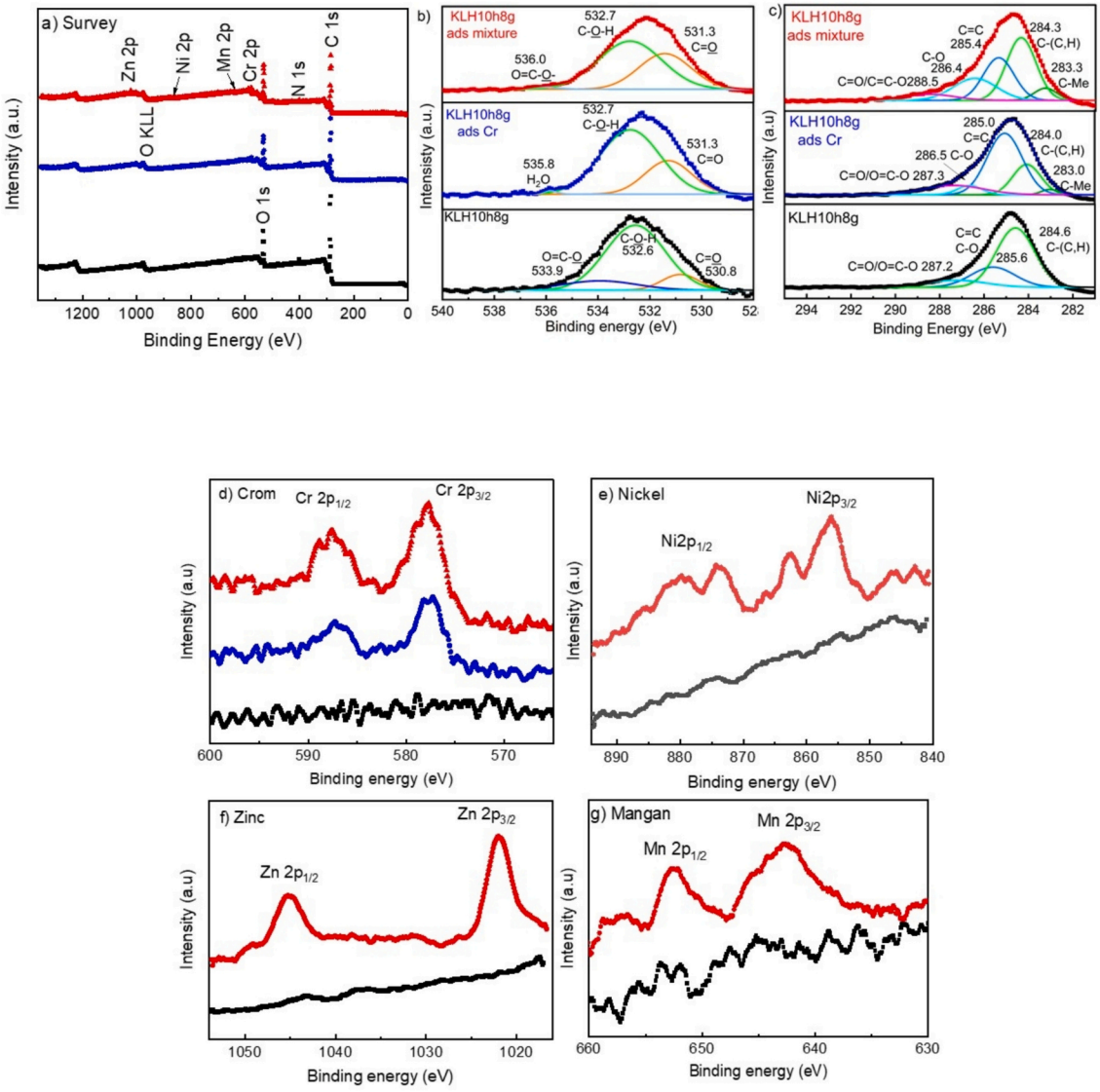


**Fig. 11.** XPS spectra of KLH10h8g sample before and after adsorption: a) XPS Survey; b) oxygen; c) Carbon; d) Crom; e) Nickel; f) Zinc; g) Mangan.
(Note: KLH10h8g sample before: black signal, sample after adsorption of Cr ion: blue line, sample after adsortption of ion mixture (Cr, Ni, Zn, Mn): red signal)

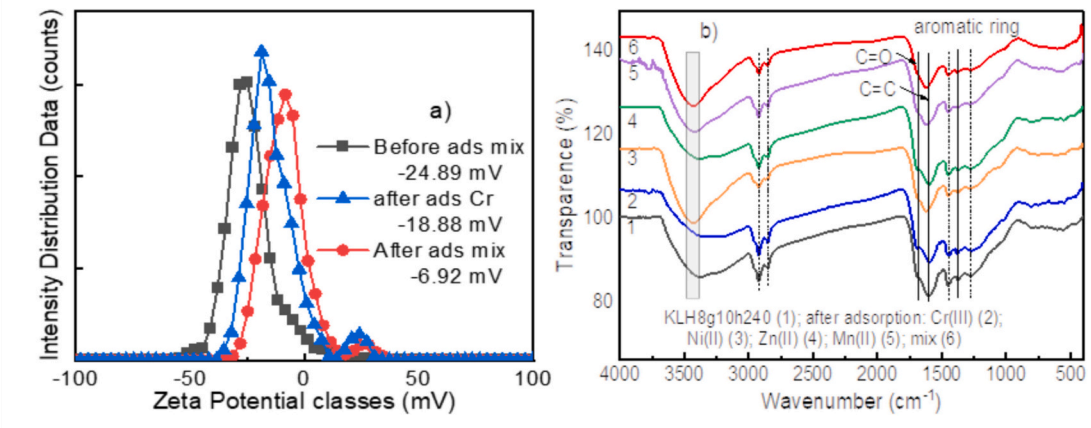


**Fig. 12.** FTIR spectra (a) and zeta potential diagram (b) of the KLH10h8g sample before and after adsorption.

simultaneous adsorption, suggesting that the negative surface charge was neutralized by the presence of metal cations and $H^+$ ions. The shifting of ζ potential of sample after adsoption of Cr(III) is not much (from −24.89 mV to −18.88 mV) but demonstrating that cation of Cr adsorbed on the surface, or Cr(III) ion was partially hydrolyzed to form $CrOH^{2+}$, dit not completely hydrolyze to $Cr(OH)_3$. It also means the adsorption are governed by electrostatic attraction.

The data presented in Fig. 12b indicate that the characteristic peaks of C—H alkane bonds (approximately 2900 $cm^{-1}$) do not exhibit significant changes. The peaks corresponding to aromatic ring bonds shifted slightly after the individual and multi-ion adsorption. The spectral peak associated with O—H bonds in the region around 3400 $cm^{-1}$ exhibited pronounced changes following the adsorption of both single and multi-ions. Specifically, after the adsorption of Cr(III) and Zn(II), this peak broadened. In contrast, after the adsorption of Ni(II) and Mn (II), as well as during multi-ion adsorption, peak has been narrowed and the position shifted. These changes suggest that the bonds were affected by interactions with the metal cations. Similar shifts were noted for the spectral peaks corresponding to C═O and C═C bonds in the range of 1600–1700 $cm^{-1}$. These bonds are characterized by high electron density or involve atoms with unshared electron pairs, which indicating elevated electronegativity. This suggests the potential for interactions with cations through electrostatic forces or donor-acceptor bonding with the vacant orbitals of heavy metal cations [18,28,58]. These results highlight the compelling evidence that the interactions are of a chemical nature.

### 3.2.5. *Adsorption of real samples*

Studies conducted at various concentrations demonstrate that hydrochar derived from DWL has significant potential for the simultaneous adsorption of Cr(III), Zn(II), Ni(II), and Mn(II). It may also adsorb other ions. Several real samples with varying compositions were randomly selected to evaluate the practical applicability of the material. The actual samples were sourced from two different locations. Sample 1 was from the waste stream of the zinc refining process, which had been preliminarily treated by alkalization to precipitate hydroxides and then acidified to neutrality. Sample 2 was from surface water flowing from a village engaged in artisanal production. Qualitative and quantitative analyses of the sample compositions were performed using ICP-OES. The results revealed the presence of various cations and the anion $SO_4^{2-}$. The efficiency and adsorption capacities for different cations in the real samples are illustrated in Fig. 13.

Fig. 13 demonstrates that, due to the varied composition and random nature of the sample, the concentrations of ions within the solution were heterogeneous. Both $Na^+$ and $Ca^{2+}$ cations were present, but their adsorption was relatively weak. The greater adsorption affinity of $Ca^{2+}$compared to $Na^+$ suggests that adsorption tends to increase with ionic charge and radius. However, the KLH10h8g activated carbon not only sustained high adsorption capacities for Cr(III), Zn(II), Ni(II), and Mn(II), but also demonstrated significant adsorption for other heavy metal ions such as Cd(II), Pb(II), and Co(II). These results further indicate that the presence of $Na^+$ and $Ca^{2+}$ had ínignificant impact on the adsorption efficiency of these heavy metal ions. Conversely, the sample showed negligible adsorption for As, which may be due to the As species in an anionic form rather than as a cation. These findings underscore the sample's significant potential for practical applications, demonstrating minimal susceptibility to interference from dissolved ions.

## 4. Conclusions

The residual biomass derived from the essential oil distillation process was extensively studied for hydrochar production, focusing on the effects of hydrothermal duration, temperature, and the solid-to-liquid ratio of the reaction mixture, with and without subsequent alkali activation. The resultant material comprised 84.4 % carbon, exhibited a specific surface area of 32.66 $m^2/g$ and displayed a uniform microporous structure with particle dimensions of approximately 1.5 × 5 μm. The surface of the hydrochar retained advantageous functional groups conducive to heavy metal cation adsorption, including C═O bonds, aromatic rings, O—H groups, and C-O-C linkages. This hydrochar exhibited exceptional adsorption capabilities for the cations Cr(III), Ni (II), Zn(II), and Mn(II), both individually and within a mixed ion solution. The adsorption capacity was observed to follow the order Zn(II) < Mn(II) < Ni(II) < Cr(III), influenced by covalent indices, ionic index and ionic charges. The adsorption mechanisms incorporated both chemical interactions and electrostatic forces. Experimental data pertaining to the adsorption adhered to the Freundlich (individual adsorption) and modified extended Sips isotherm models (simultaneous adsorption), and the Elovich kinetic models. When the initial concentration increased, the correlation with pseudo-first-order and pseudo-second-order kinetic models improved, suggesting stronger physical interactions. Although competitive interactions among ions in solution were noted, their impact was minimal due to the presence of other cations or dissolved cations. Combined with testing on actual samples, our study indicates that lemongrass hydrochar presents substantial potential as an adsorbent for practical applications. It holds promise for effectively removing heavy metal ions in wastewater.

## CRediT authorship contribution statement

**Thi Thao Truong:** Writing – original draft, Visualization, Validation, Supervision, Methodology, Investigation, Data curation, Conceptualization. **Truong Xuan Vuong:** Writing – review & editing, Writing – original draft. **Thi Hong Huyen Chu:** Project administration,

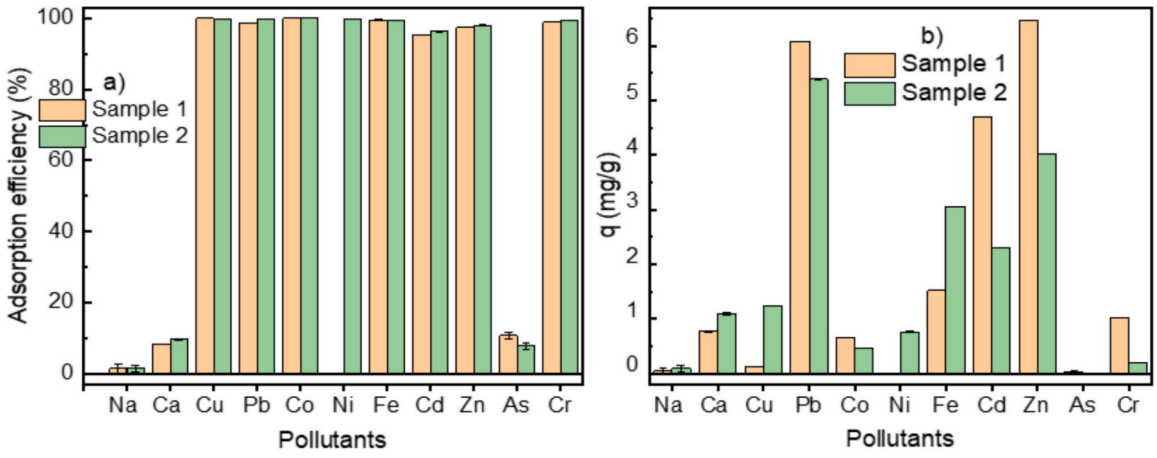


**Fig. 13.** Adsorption efficiencies and capacities of KLH10h8g for the actual samples.

Investigation, Data curation. **Thi Hong Tham Diep:** Investigation, Data curation. **Hoang Chinh Ta:** Software, Resources. **Le Phuong Hoang:** Validation, Methodology, Formal analysis. **Tien Duc Pham:** Writing – review & editing, Validation, Methodology, Conceptualization.

## Funding

This research was partially supported by the TNU-University of Sciences under the project code: CS2023-TN06-17.

## Declaration of competing interest

The authors declare that they have no known competing financial interests or personal relationships that could have appeared to influence the work reported in this paper.

## Appendix A. Supplementary data

Supplementary data to this article can be found online at https://doi.org/10.1016/j.jwpe.2025.107402.

## Data availability

Data will be made available on request.

## References

[1] J. Huang, Y. Feng, H. Xie, P. Wu, M. Wang, B. Wang, Q. Wang, S. Zhang, Z. Liu, A bibliographic study reviewing the last decade of hydrochar in environmental application: history, status quo, and trending research paths, Biochar 5 (2023) 12, https://doi.org/10.1007/s42773-023-00210-4.

[2] G.M. Mohamed, O.I. El-Shafey, N.A. Fathy, Preparation of carbonaceous hydrochar adsorbents from cellulose and lignin derived from rice straw, Egypt. J. Chem. 60 (2017) 793–804, https://doi.org/10.21608/ejchem.2017.1311.1080.

[3] M. Cavali, Nelson L. Junior, J. D. de Sena, A. L. Woiciechowski, C. R. Soccol, P. B. Filho, R. Bayard, H. Benbelkacem, A. B. C. Junior, A review on hydrothermal carbonization of potential biomass wastes, characterization and environmental applications of hydrochar, and biorefinery perspectives of the process, Science of the Total Environment, 857 (2023) 159627, doi:10.10 16/j. scitotenv.2022.159627.

[4] L.P. Padhye, E.R. Bandala, B. Wijesiri, A. Goonetilleke, N. Bolan, Hydrochar: a promising step towards achieving a circular economy and sustainable development goals, Frontiers in Chemical Engineering 4 (2022) 867228, https://doi.org/10.3389/fceng.2022.867228.

[5] A. Kumar, R.K. Lal, A.K. Gupta, C.S. Chanotiya, Historical and contemporary development of novel chemotype varieties with high essential oil of lemongrass in India: a review, J Med Aromat Plant Sci 45 (2023) 17–27, https://doi.org/10.62029/jmaps.v45i1.kumar.

[6] G. Agegnehu, K. Jemal, A. Abebe, B. Lulie, Plant growth and oil yield response of lemon grass (Cymbopogon citratuc L.) to biochar application, Ethiop. J. Agric. Sci. 29 (3) (2019) 1–12.

[7] S. Jain, V. Yadav, D. Mishra, B. Kumar, Y. Deshmukh, N. Nigam, P. Khare, Utilizing three different biochars for attenuation of toxic acidic mine spoils reflected by lixiviate quality Vis-a-Vis Phyto-toxicity on Ocimum sanctum and Cassia angustifolia, Global Journal of Agricultural Innovation, Research & Development 8 (2022) 49–65, https://doi.org/10.15377/2409-9813.2021.08.4.

[8] K.L. Sefatlhi, V.U. Ultra, S. Majoni, Chemical and structural characteristics of biochars from phytoremediation biomass of *Cymbopogon Citratus*, *Cymbopogon Nardus*, and *Chrysopogon Zizanioides*, Waste Biomass Valor 15 (2024) 283–300, https://doi.org/10.1007/s12649-023-02164-x.

[9] A. Saha, B.B. Basak, N.A. Gajbhiye, K.A. Kalariya, P. Manivel, Sustainable fertilization through co-application of biochar and chemical fertilizers improves yield, quality of *Andrographis paniculata* and soil health, Ind. Crop. Prod. 140 (2019) 111607, https://doi.org/10.1016/j.indcrop.2019.111607.

[10] M. Jalilian, R. Bissessur, M. Ahmed, A. Hsiao, Q.S. He, Y. Hu, A review: Hydrochar as potential adsorbents for wastewater treatment and $CO_2$ adsorption, Sci. Total Environ. 914 (2024) 169823, https://doi.org/10.1016/j.scitotenv.2023.169823.

[11] M.N. Mahmood Al-Nuaimy, et al., Nangyallai Azizi, Yahya Nura, Erdal Yabalak, recent advances in environmental and agricultural applications of hydrochars: a review, Environ. Res. 250 (2024) 117923, https://doi.org/10.1016/j.envres.2023.117923.

[12] J.O. Ighalo, S. Rangabhashiyam, K. Dulta, C.T. Umeh, K.O. Iwuozor, C.O. Aniagor, S.O. Eshiemogie, F.U. Iwuchukwu, C.A. Igwegbe, Recent advances in hydrochar application for the adsorptive removal of wastewater pollutants, Chem. Eng. Res. Des. 184 (2022) 419–456, https://doi.org/10.1016/j.cherd.2022.06.028.

[13] Z. Liu, F.S. Zhang, J. Wu, Characterization and application of chars produced from pinewood pyrolysis and hydrothermal treatment, Fuel 89 (2010) 510–514, https://doi.org/10.1016/j. fuel.2009.08.042.

[14] B. Li, J.L. Liu, H. Xu, Synthesis of polyaminophosphonated-functionalized hydrochar for efficient sorption of Pb(II), Environ. Sci. Pollut. Res. 29 (2022) 49808–49815, https://doi.org/10.1007/s11356-022-19350-4.

[15] X. Han, Z. Wang, N. Lu, J. Tang, P. Lu, K. Zhu, J. Guan, T. Feike, Comprehensive study on the hydrochar for adsorption of cd(II): preparation, characterization, and mechanisms, Environ. Sci. Pollut. Res. 30 (2023) 64221–64232, https://doi.org/10.1007/s11356-023-26956-9.

[16] J. Pan, J. Jiang, R. Xu, Adsorption of Cr(III) from acidic solutions by crop straw derived biochars, J. Environ. Sci. 25 (10) (2013) 1957–1965, https://doi.org/10.1016/S1001-0742(12)60305-2.

[17] Y. Zhang, J. Qu, Y. Yuan, H. Song, Y. Liu, S. Wang, Y. Tao, Y. Zhao, Z. Li, Simultaneous scavenging of cd(II) and Pb(II) from water by sulfide-modified magnetic pinecone-derived hydrochar, J. Clean. Prod. 341 (2022) 130758, https://doi.org/10.1016/j.jclepro.2022.130758.

[18] X. Zhang, Z. Gao, X. Fan, L. Tan, Y. Jang, W. Zheng, F.X. Han, Y. Liang, A comparative study on adsorption of cadmium and lead by hydrochars and biochars derived from rice husk and *Zizania latifolia* straw, Environ. Sci. Pollut. Res. 29 (2022) 63768–63781, https://doi.org/10.1007/s11356-022-20263-5.

[19] Y. Zhang, Y. Wan, Y. Zheng, Y. Yang, J. Huang, H. Chen, G. Quan, B. Gao, Potassium permanga- nate modification of hydrochar enhances sorption of Pb(II), cu(II), and cd(II), Bioresour. Technol. 386 (2023) 129482, https://doi.org/10.1016/j.biortech.2023.129482.

[20] Y. Xue, B. Gao, Y. Yao, M. Inyang, M. Zhang, A.R. Zimmerman, K.S. Ro, Hydrogen peroxide modification enhances the ability of biochar (hydrochar) produced from hydrothermal carbonization of peanut hull to remove aqueous heavy metals: batch and column tests, Chem. Eng. J. 200–202 (2012) 673–680, https://doi.org/10.1016/j.cej.2012,.06.116.

[21] X. Luo, H. Du, X. Zhang, B. Tang, M. Zhang, H. kang, Y. Ma, Enhanced adsorption and co-adsorption of heavy metals using highly hydrophilicity amine-functionalized magnetic hydrochar supported MIL-53(Fe)-$NH_2$: performance, kinetics, and mechanism studies. Environ. Sci. Pollut. Res. 30 (2023): 76204–76216, doi:https://doi.org/10.1007/s11356-023-27740-5.

[22] M.A. Bahmanyar, Cadmium, nickel, chromium, and Lead levels in soils and vegetables under long term irrigation with industrial wastewater, Commun. Soil Sci. Plant Anal. 39 (13–14) (2008) 2068–2079, https://doi.org/10.1080/00103620802135013.

[23] A. Sarkar, N. Mushahary, B. Das, S. Basumatary, A novel approach for modification of mont- morillonite using banana peel ash extract for enhanced adsorption efficiency of methylene blue dye, Desalin. Water Treat. 320 (2024) 100585, https://doi.org/10.1016/j.dwt.2024.100585.

[24] C.E. Almeida-Naranjo, M.B. Aldás, G. Cabrera, V.H. Guerrero, Caffeine removal from synthetic wastewater using magnetic fruit peel composites: material characterization, isotherm and kinetic studies, Environmental Challenges 5 (2021) 100343, https://doi.org/10.1016/j.envc.2021.100343.

[25] M. Joudi, H. Nasserlah, H. Hafdi, J. Mouldar, B. Hatimi, M.A. El Mhammedi, M. Bakasse, Synthesis of an efficient hydroxyapatite–chitosan–montmorillonite thin film for the adsorption of anionic and cationic dyes: adsorption isotherm, kinetic and thermodynamic study, SN Appl. Sci. 2 (2020) 1078, https://doi.org/10.1007/s42452-020-2848-3.

[26] T.N.L. Minh, D. Manhaeghe, G. Bernaert, J. Hogie, M. Clarembeau, K.M.V. Geem, S.D. Meester, Activated carbon adsorption of heteroatom components from pyrolysis oil for improved chemical recycling, Chem. Eng. J. 481 (2024) 148394, https://doi.org/10.1016/j.cej.2023.148394.

[27] V.K. Nguyen, T.H.H. Nguyen, T.D. Pham, T.T. Truong, Adsorption characteristics and mechanisms of individual and a quinary mixture of heavy metal ions on novel CoFe2O4-BiFeO3 nanosorbents in water, Inorg. Chem. Commun. 170 (2024) 113177, https://doi.org/10.1016/j. inoche.2024.113177.

[28] M. Haris, M.W. Khan, J. Paz-Ferreiro, N. Mahmood, N. Eshtiaghi, Synthesis of functional hydrochar from olive waste for simultaneous removal of azo and non-azo dyes from water, Chemical Engineer- ing Journal Advances 9 (2022) 100233, https://doi.org/10.1016/j.ceja.2021.100233.

[29] X. Jiao, Y. Qiu, L. Zhang, X. Zhang, Comparison of the characteristic properties of reduced graphene oxides synthesized from natural graphites with different graphitization degrees, RSC Adv. 7 (2017) 52337–52344, https://doi.org/10.1039/C7RA10809E.

[30] F. Li, A.R. Zimmerman, X. Hu, Z. Yu, J. Huang, B. Gao, One-pot synthesis and characterization of engineered hydrochar by hydrothermal carbonization of biomass with $ZnCl_2$, Chemosphere 254 (2020) 126866, https://doi.org/10.1016/j.chemosphere.2020.126866.

[31] C. Costa, B. Medronho, A. Eivazi, I. Svanedal, B. Lindman, H. Edlund, M. Norgren, Lignin enhances cellulose dissolution in cold alkali, Carbohydr. Polym. 274 (2021) 118661, https://doi.org/10.1016/j.carbpol. 2021.118661.

[32] S. Nomura, Y. Kugo, T. Erata, $^{13}C$ NMR and XRD studies on the enhancement of cellulose II crystallinity with low concentration NaOH post-treatments, Cellulose 27 (2020) 3553–3563, https://doi.org/10.1007/s10570-020-03036-6.

[33] Y. Shi, H. Lim Y. Rong, L. Bai, M. Chi, X. Xu, X. Li, H. Bai, Y. Liu, The Improving of $Cd^{2+}$ Adsorption Performance of Hydrochar Obtained from Corn Straw Waste with KOH Activation, Water Air and Soil Pollution 233(12), (2022): 233:502, doi:https://doi.org/10.1007/s11270-022-05981-3.

[34] C. Saunders, J.E.J. Foote, J.P. Wojciechowski, A. Cammack, S.V. Pedersen, J. J. Doutch, H.M.G. Barriga, M.N. Holme, J. Penders, M. Chami, A. Najer, M. M. Stevens, Revealing population heterogeneity in vesicle-based nanomedicines using automated, Single Particle Raman Analysis, ACS Nano. 17 (12) (2023) 11713–11728, https://doi.org/10.1021/acsnano.3c02452.

[35] G. M. Khairy, A. M. Hesham, H. E. Jahin, S. A. El-Korashy, Y. M. Awad, green synthesis of a novel eco-friendly hydrochar from pomegranate peels loaded with

iron nanoparticles for the removal of copper ions and methylene blue from aqueous solutions, journal of molecular liquids, 368, part a, 15 December 2022, 120722, 2022, doi:https://doi.org/10.1016/j.molliq.2022.120722.
[36] H. Zhang, F. Zhang, Q. Huang, Highly effective removal of malachite green from aqueous solution by hydrochar derived from phycocyanin-extracted algal bloom residues through hydrothermal carboni- zation, RSC Advances, Issue 10 (2017) 5790–5799, https://doi.org/10.1039/c6ra27782a.
[37] D. Jaruwat, P. Udomsap, N. Chollacoop, M. Fuji, A. Eiad-ua, Effects of hydrothermal temperature and time of hydrochar from cattail leaves, AIP Conf. Proc. 2010 (2018) 020016, https://doi.org/10.1063/1. 5053192.
[38] A.Y. Lee, K. Yang, N.D. Anh, C. Park, S.M. Lee, T.G. Lee, M.S. Jeong, Raman study of D* band in graphene oxide and its correlation with reduction, Appl. Surf. Sci. 536 (2021) 147990, https://doi.org/10.1016/j.apsusc.2020.147990.
[39] B. Fuertes, M. Camps Arbestain, M. Sevilla, J.A. Maciá-Agulló, S. Fio, R. López, R. J. Smernik, W.P. Aitkenhead, F. Arce, F. Macias, Chemical and structural properties of carbonaceous products obtained by pyrolysis and hydrothermal carbonisation of corn Stover, Aust. J. Soil Res. 48 (2010) 618–626, https://doi.org/10.1071/SR10010.
[40] N. Atykyan, V. Revin, V. Shutova, Raman and FT-IR spectroscopy investigation the cellulose structural differences from bacteria *Gluconacetobacter sucrofermentans* during the different regimes of cultivation on a molasses media, AMB Express 10 (2020) 84, https://doi.org/10.1186/s13568-020-01020-8.
[41] T. Wang, Y. Zhai, Y. Zhu, C. Li, G. Zeng, A review of the hydrothermal carbonization of biomass waste for hydrochar formation: process conditions, fundamentals, and physico- chemical properties, Renew. Sust. Energ. Rev. 90 (2018) 223–247, https://doi.org/10.1016/j.rser.2018.03.071.
[42] Y. Gao, X. Wang, J. Wang, X. Li, J. Cheng, H. Yang, Effect of residence time on chemical and structural properties of hydrochar obtain, Energy 58 (2013) 376–383, https://doi.org/10.1016/j. energy.2013.06.023.
[43] F. Teng, Y. Zhang, D. Wang, M. Shen, D. Hu, Iron-modified rice husk hydrochar and its immobili- zation effect for Pb and Sb in contaminated soil, J. Hazard. Mater. 398 (2020) 122977, https://doi.org/10.1016/j.jhazmat.2020.122977.
[44] H. Kim, S.Y. Lee, J. Choi, K. Jung, Synergistic effect in simultaneous removal of cationic and anionic heavy metals by nitrogen heteroatom doped hydrochar from aqueous solutions, Chemosphere 323 (2023) 138269, https://doi.org/10.1016/j.chemosphere.2023.138269.
[45] B. Chen, H. Guan, Y. Zhang, S. Liu, B. Zhao, C. Zhong, H. Zhang, W. Ding, A. Song, D. Zhu, L. Liu, B. Wulan, H. Li, G. Liu, X. Feng, Performance and mechanism of $Pb^{2+}$ and $Cd^{2+}$ ions' adsorp- tion via modifed antibiotic residue-based hydrochar, Heliyon 9 (2023) e14930, https://doi.org/10.1016/j. heliyon.2023.e14930.
[46] Z. Ding, L. Zhang, H. Mo, Y. Chen, X. Hu, Microwave-assisted catalytic hydrothermal carbonization of *Laminaria japonica* for hydrochars catalyzed and activated by potassium compounds, Bioresour. Technol. 341 (2021) 125835, https://doi.org/10.1016/j.biortech.2021.125835.
[47] F. Dhaouadi, L. Sellaoui, L.E. Hernández-Hernández, A. Bonilla-Petriciolet, D. I. Mendoza-Castillo, H.E. Reynel-Avila, H.A. Gonzalez-Ponce, S. Taamalli, F. Louis, A.B. Lamine, Preparation of an avocado seed hydrochar and its application as heavy metal adsorbent: properties and advanced statistical physics modeling, Chem. Eng. J. 419 (2021) 129472, https://doi.org/10.1016/j.cej.2021.129472.
[48] K. Nadarajah, E.R. Bandala, Z. Zhang, S. Mundree, A. Goonetilleke, Removal of heavy metals from water using engineered hydrochar: kinetics and mechanistic approach, Journal of Water Process Engineering 40 (2021) 101929, https://doi.org/10.1016/j.jwpe.2021.101929.
[49] T. Nizam, K.A. Krishnan, A. Joseph, R.R. Krishnan, Isotherm, kinetic and thermodynamic modelling of liquid phase adsorption of the heavy metal ions Zn (II), Pb(II) and Cr(VI) onto $MgFe_2O_4$ nanoparticles, Groundw. Sustain. Dev. 25 (2024) 101120, https://doi.org/10.1016/j.gsd.2024.101120.
[50] S.S. Zamil, S. Ahmad, M.H. Choi, J.Y. Park, S.C. Yoon, Correlating metal ionic characteristics with biosorption capacity of *staphylococcus saprophyticus* BMSZ711 using QICAR model, Bioresour. Technol. 100 (6) (2009) 1895–1902, https://doi.org/10.1016/j.biortech.2008.10.014.
[51] F. Batool, A. Irfan, S.A. Al-Hussain, E.S. Al-Farraj, S. Iqbal, J. Akbar, S. Noreen, T. Akhtar, T. Iqbal, M.E.A. Zaki, Development of ion character property relationship (IC-PR) for removal of 13-metal ions by employing a novel green adsorbent *Aerva javanica*, Molecules 27 (23) (2022) 8213, https://doi.org/10.3390/molecules27238213.
[52] M.C. Newman, J.T. McCloskey, Predicting relative toxicity and interactions of divalent metal ions, Microtox® bioluminescence assayEnvironmental Toxicology and Chemistry 15 (3) (1996) 275–281, https://doi.org/10.1002/etc.5620150308.
[53] J.S. Al-Jariri, F. Khalili, Adsorption of Zn(II), Pb(II), Cr(III) and Mn(II) from waterby Jordanian bentonite, Desalin. Water Treat. 21 (2010) 308–322, https://doi.org/10.5004/dwt.2010.1623.
[54] M.A. Barakat, M.H. Ramadan, M.A. Alghamdi, S.S. Algarny, H.L. Woodcock, J. N. Kuhn, Remediation of cu(II), Ni(II), and Cr(III) ions from simulated wastewater by dendrimer/titania composites, J. Environ. Manag. 117 (2013) 50–57, https://doi.org/10.1016/j.jenvman. 2012.12.025.
[55] S. Bagdat, F. Tokay, S. Demirci, S. Yilmaz, N. Sahiner, Removal of cd(II), co(II), Cr (III), Ni(II), Pb(II) and Zn(II) ions from wastewater using polyethyleneimine (PEI) cryogels, J. Environ. Manag. 329 (2023) 117002, https://doi.org/10.1016/j.jenvman.2022.117002.
[56] V. Thangaraj, K. Aravamudan, R. Lingam, S. Subramanian, Individual and simultaneous adsorption of Ni (II), cd (II), and Zn (II) ions over polyamide resin: equilibrium, kinetic and thermodynamic studies, Environ. Prog. Sustain. Energy 38 (2018) S340–S351, https://doi.org/10.1002/ep. 13056.
[57] L.S. Chan, W.H. Cheung, S.J. Allen, G. McKay, Equilibrium adsorption isotherm study of binary basic dyes on to bamboo derived activated carbon, HKIE Transactions 24 (4) (2017) 182–192, https://doi.org/10.1080/1023697X.2017.1375434.
[58] J.B. Neris, F.H.M. Luzardo, E.G.P. da Silva, F.G. Velasco, Evaluation of adsorption processes of metal ions in multi-element aqueous systems by lignocellulosic adsorbents applying different isotherms: a critical review, Chem. Eng. J. 357 (2019) 404–420, https://doi.org/10.1016/j.cej. 2018.09.125.
[59] Q. Chen, Y. Wang, G. He, M. Yilmaz, S. Yuan, $KMnO_4$-activated spinach waste biochar: an efficient adsorbent for adsorption of heavy metal ions in aqueous solution, Colloids and Surfaces A: Physico- chemical and Engineering Aspects 684 (2024) 133174, https://doi.org/10.1016/j.colsurfa.2024.133174.
[60] F. Wu, R. Tseng, R. Juang, Characteristics of Elovich equation used for the analysis of adsorption kinetics in dye-chitosan systems, Chem. Eng. J. 150 (2–3) (2009) 366–373, https://doi.org/10.1016/j.cej.2009.01.014.
[61] H. Wang, M. Zhang, Qi Lv, Removal Efficiency and Mechanism of Cr(VI) from Aqueous Solution by Maize Straw Biochars Derived at Different Pyrolysis Temperatures. Water, 11(4) (2019), 781; doi:10. 3390/w11040781.
[62] F. Li, N. Kannari, J. Maruyama, K. Sato, H. Abe, Defective multi-element hydroxides nanosheets for rapid removal of anionic organic dyes from water and oxygen evolution reaction, J. Hazard. Mater. 447 (2023) 130803, https://doi.org/10.1016/j.jhazmat.2023.130803.
[63] Y. Li, F.M. Hagos, R. Chen, et al., Rice husk hydrochars from metal chloride-assisted hydrothermal carbonization as biosorbents of organics from aqueous solution, Bioresour. Bioprocess. 8 (2021) 99, https://doi.org/10.1186/s40643-021-00451-w.
[64] M. Rjeba, A. Labzour, A. Rjeb, S. Sayouri, M. Chafik El Idrissi, S. Massey, A. Adnot, D. Roy, Contribution to the study by x-ray photoelectron spectroscopy of the natural aging of the polypropylene, M. J. Condensed Matter, 5(2) 2004,168–172, https://www.researchgate.net/ publication/2915266].
[65] A. Furlan, J. Lu, L. Hultman, Ulf Jansson and M. Magnuson, Crystallization characteristics and chemical bonding properties of nickel carbide thin film nanocomposites, J. Phys.: Condens. Matter 26 (2014) 415501, doi:https://doi.org/10.1088/0953-8984/26/41/415501.